Final Report

SYNTHESIS AND CHARACTERIZATION OF $BaFeO_3$, $(Ba,Bi)FeO_3$, AND RELATED EPITAXIAL THIN FILMS AND NANOSTRUCTURES

David P. Norton
Dept. of Materials Science and Engr
University of Florida
Gainesville, FL 32611

dnort@mse.ufl.edu

Sponsored by Army Research Office

Grant Number W911NF0510519

Report Documentation Page

Form Approved
OMB No. 0704-0188

1. REPORT DATE	2. REPORT TYPE	3. DATES COVERED
2009		**00-00-2009 to 00-00-2009**

4. TITLE AND SUBTITLE	5a. CONTRACT NUMBER
Synthesis and Characterization of BaFeO3, (Ba,Bi)FeO3, and Related Epitaxial Thin Films and Nanostructures	**W911NF-05-1-0519**
	5b. GRANT NUMBER
	5c. PROGRAM ELEMENT NUMBER
6. AUTHOR(S)	5d. PROJECT NUMBER
	5e. TASK NUMBER
	5f. WORK UNIT NUMBER
7. PERFORMING ORGANIZATION NAME(S) AND ADDRESS(ES)	8. PERFORMING ORGANIZATION REPORT NUMBER
University of Florida,Dept. of Materials Science and Engr,Gainesville,FL,32611	**; 46986-MS.1**
9. SPONSORING/MONITORING AGENCY NAME(S) AND ADDRESS(ES)	10. SPONSOR/MONITOR'S ACRONYM(S)
U.S. Army Research Office, P.O. Box 12211, Research Triangle Park, NC, 27709-2211	11. SPONSOR/MONITOR'S REPORT NUMBER(S)
	46986-MS.1

12. DISTRIBUTION/AVAILABILITY STATEMENT
Approved for public release; distribution unlimited

13. SUPPLEMENTARY NOTES

14. ABSTRACT

15. SUBJECT TERMS

16. SECURITY CLASSIFICATION OF:			17. LIMITATION OF ABSTRACT	18. NUMBER OF PAGES	19a. NAME OF RESPONSIBLE PERSON
a. REPORT	b. ABSTRACT	c. THIS PAGE			
unclassified	**unclassified**	**unclassified**	**Same as Report (SAR)**	**115**	

TABLE OF CONTENTS

page

LIST OF TABLES

LIST OF FIGURES

Summarized Statement of Problem Studied

There is significant interest in identifying and manipulating new materials that have unique magnetic, dielectric, and transport properties. Single phase and artificially structured materials for which more that one electromagnetic functionality coexists are particularly interesting. In this project, the synthesis of epitaxial thin films and multilayered structure with potential to display these attributed were examined. Specifically, epitaxial growth and characterization studies were carried out for the following systems:

- $BaFeO_3$: the growth and properties of $BaFeO_3$, a metastable ferromagnetic perovskite whose structure is realized only in epitaxial films, was examined. The growth of superlattice structures using this compound as a component was also examined.
- $BaFeO_3$-$BiFeO_3$ solid solution alloys: the synthesis and properties of $BaFeO_3$ films alloyed with $BiFeO_3$, a known multiferroic perovskite, was examined.
- $K(Ta,Nb)O_3$: the growth kinetics of $K(Ta,Nb)O_3$, a candidate ferroelectric component for ferroelectric/ferromagnetic multiferroic superlattices, was examined using reflection high energy electron diffraction
- $ZnCo_2O_4$: the growth and properties of $ZnCo_2O_4$, a ferromagnetic semiconducting spinel oxide, was examined

1.0 INTRODUCTION

Multiferroic materials are of interest due to their potential use in communication, computing, and memory storage. These materials have two or more ferroic properties that coexist in the same phase. The properties may or may not be coupled. Multiferroic materials are an example of a broader class of multifunctional or smart materials which combine several properties in the same material.[1] The most interesting multiferroic material opportunties are those that exhibit ferroelectricity and ferromagnetism in the same phase. The applications for these materials are many, one example being an electric field switchable magnetization.

Multiferroics were discovered many decades ago, but the resurgence in interest comes mainly from three interrelated factors, as mentioned by W. Eerenstein, *et al*.[2] A recent review article discusses the requirements for ferroelectricity and ferromagnetism to exist simultaneously in oxides and suggests why there are so few magnetic ferroelectrics (or multiferroics).[2, 3] This declaration posed a challenge to scientists to address this problem with new materials. Secondly, techniques able to investigate on an atomic scale were not available at the time the earliest multiferroics were discovered. In recent years, many nanoscale characterization and analysis techniques have been developed for the study and fabrication of new materials. Finally, there is a relentless drive for new materials for improved transducers, magnetic field sensors, and most importantly and presently, information storage technology.[2, 4, 5]

Before manipulating materials and structures to induce multiferroic behavior, there is a need to address fundamental properties of the parent compounds, and to use that knowledge to create new materials with properties that are complimentary. This work largely examines the fundamental properties of specific perovskite oxides ($BaFeO_3$ and $BiFeO_3$) and the effect on their properties when alloyed together. A brief overview of magnetism, ferroelectrics, and multiferroics is given. This includes an overview of the perovskite materials of primary interest

in this study, namely $BaFeO_3$ and $BiFeO_3$. In addition, a brief discussion is given of the history of multiferroic materials, along with the study of single phase, composite, heterostructure, and solid solution materials.

The chosen technique for sample synthesis, namely pulsed-laser deposition, is described. The various characterization methods for sample analysis are briefly discussed. Investigation of $BaFeO_3$ and its structural and magnetic properties, which differ from that of the bulk, are then examined. The sensitivity of magnetic properties on oxygenation is discussed, along with complexities of its structural properties via x-ray diffraction, and the effects of growth conditions on as-grown and post-annealed magnetic properties. The Report then discusses the synthesis and properties of a single phase solid solutions between $BaFeO_3$ and $BiFeO_3$. The structural and magnetic properties of a specific alloy composition are discussed as a function of synthesis and substrate choice. We then discuss controlling the growth of related perovskites useful for superlattice formation, along with results for a semiconducting magnetic spinel oxide that was also included in this study.

2. REVIEW OF MULTIFERROIC MATERIALS

Magnetism

Ampére postulated more than a century ago that molecular currents are responsible for magnetism in solids.[6, 7] Magnetic properties exhibited by materials include diamagnetism, paramagnetism, ferromagnetism, and antiferromagnetism. In addition, some applications of the discussed magnetic properties are provided. In diamagnetism, there is a change in orbital motion due to an externally applied magnetic field that occurs in materials, including those whose electron shells are completely filled.[6] All materials exhibit a diamagnetic effect, though it is weak and largely over-shadowed by much stronger magnetic interactions. Materials and/or atoms that are diamagnetic have a small and negative magnetic susceptibility, χ_m. Materials with closed electron (sub)shells exhibit diamagnetism.[8] Diamagnetic materials do not have a permanent magnetic moment, and are not particularly useful in magnetic applications. Materials that have net magnetic moments, but are only weakly coupled, are known as paramagnets.[8] Transition metal salts exhibit paramagnetism from a transition metal cation having a partially filled *d* shell. Dilute gases, rare earth salts and elements have an additional source of paramagnetism due to the magnetic moment of the orbiting electrons. Without a field, there is a net magnetization of zero, but when field is applied, the magnetic moments align somewhat in the general field direction. Thermal changes counteract their alignment, making electron-orbit paramagnetism temperature dependent.[7] Some paramagnetic materials obey the Curie law shown in Eq. 2-1:

$$\chi = \frac{C}{T}, \qquad \text{(2-1)}$$

where C is the Curie constant and T is temperature. Other materials observe the Curie-Weiss law shown by Eq. 2-2:

$$\chi = \frac{C}{T - \theta}, \quad \text{(2-2)}$$

where θ is a constant that has the same units at C.[8,9] In Eq. 2-2, when $T = \theta$, there is a divergence in the susceptibility that corresponds to a phase transition to a spontaneously ordered magnetic phase.[6] Like diamagnetic materials, few applications exploit paramagnetism due to the lack of net permanent magnetic moment. Eq. 2-2 shows the Curie-Weiss behavior for paramagnetic materials. In ferromagnetic, a Curie temperature, T_C, is defined as the critical temperature below which a paramagnetic material exhibits spontaneous ordering of spin moments. Origins of ferromagnetism come from the quantum mechanical exchange interaction between component atoms resulting in permanent magnetization.[6-8] Ferromagnetic materials have strong permanent magnetizations even in the absence of an externally applied magnetic field. The magnetic susceptibility χ_m is positive and depends on the history of the applied field.

A largely nonlinear relationship exists between the externally applied magnetic field $\mu_o\mathbf{H}$ and the magnetization **M**, and at very high magnetic fields (depending on the material) the magnetization **M** saturates, called the saturation magnetization M_s.[7] When the magnetic field reduces to zero, the material has a remnant magnetization M_r. Further reducing the applied field below zero causes the magnetization **M** to eventually reach zero, reaching the coercive field H_c at $\mathbf{M} = 0$.[8]

Antiferromagnets consist of two interpenetrating magnetic spin sub-lattices with anti-parallel moments. This gives a net zero magnetic moment, with a susceptibility χ_m that is small, positive and linear with applied field.[6] Antiferromagnets have a phase transition temperature called the Néel Temperature T_N. Above this temperature the material behaves like a paramagnet.

The magnetic structure of antiferromagnets can be determined and quantified using neutron diffraction experimental methods. The origin of antiferromagnetic ordering comes from quantum mechanical exchange forces similar to that in ferromagnets except that antiferromagnets possess a negative molecular field, causing the spins to align anti-parallel.[6] A common mechanism to produce antiferromagnetic ordering is seen in the Fe_3O_4 system, where there are linear chains of Fe^{3+}-O^{2-}—Fe^{3+} linkages. Oxygen valence shells are filled, with the exception of 2 electrons Hybridization occurs by the donation of electrons from O^{2-} ion onto the vacant spin up (or all spin down) orbitals of the Fe^{3+} ions. This occurs throughout the chains leaving a zero net magnetic moment from this oxygen mediated interaction.[10] Ferrimagnetic materials are similar to ferromagnetic materials in that they exhibit spontaneous magnetization below a critical temperature, even in the absence of an externally applied field. Ferrimagnetic materials are similar to antiferromagnetic materials in that they also have exchange coupling between neighboring magnetic ions leading to moments arranging in antiparallel alignment. However, the ferromagnets have a net permanent magnetic moment, and large positive susceptibility. The two magnetic sublattices differ in that one sublattice will have a greater magnetic moment than the other, yielding an overall magnetic moment.[6-8]

Ferroelectrics and Piezoelectrics

Of the 32 crystal classes, there are 11 centrosymmetric (non polar), non-piezoelectric groups. This leaves 21 non-centrosymmetric groups, which are piezoelectric, and in these 10 are polar piezoelectrics. A piezoelectric material is one that undergoes a change in polarization (as well as becoming electrically polarized) when it becomes strained.[11] In applying an electric field, the crystal will also be stretched or compressed depending on the electric field's orientation to the polarization of the crystal. Crystals in the 10 polar groups are considered pyroelectric in that they have a property that is inherent in their structure—spontaneous polarization. In

addition, their polarization changes with temperature. When in a polar state these crystals possess a permanent dipole.[12] Of the pyroelectric materials, some have an additional property where, if an electric field was applied, the direction of polarization can change.[11] This property is termed ferroelectricity. One of the most widely studied ferroelectric classes of materials are those possessing the perovskite structure. The noncentrosymmetric structure in distorted perovskites is reached by A or B cations (or both) being off-center relative to the oxygen anions, shown in Figure 2-1, and the spontaneous polarization comes from the electric dipole moment created by this off-centering. In applications, ferroelectrics are candidate materials for nonvolatile memories. One of the hindrances from widespread application of these materials includes fatigue that arises from multiple cycling of these materials. Oxide electrodes help to alleviate fatigue.[13] There is great interest in ferroelectric field-effect transistors (FFETs) and ferroelectric-ferromagnetic device structure for memory applications. In some of the perovskite materials, the structural distortions that occur are not ferroelectric, but are instead antiferroelectric. Antiferroelectric dipoles order in a way that is analogous to antiferromagnetic materials, resulting in two alternating dipole sublattices that have equal but antiparallel orientations.[12]

$BaFeO_3$

$BaFeO_3$ is an ABO_3 type perovskite material. In bulk, it exists as a hexagonal perovskite structure with lattice parameters a = 0.568 nm and c = 1.386 nm.[14-17] Reports have shown it to have an antiferromagnetic to ferromagnetic transition around 160 K as well as another transition to the paramagnetic state around 250 K.[18-20] The mechanism by which hexagonal $BaFeO_3$ shows ferromagnetism is via superexchange interaction energy of the Fe^{3+}-O^{2}-Fe^{3+} linkage.[16]

When grown as thin films, $BaFeO_3$ can take on a pseudo-cubic perovskite structure (a = 0.412 nm) as reported by Matsui, *et al* [21, 22] with iron in the center of oxygen octahedra linking to

neighboring octahedra via sharing corners. Depending on partial pressure of oxygen and temperature conditions used during growth, it can be oxygen deficient. The impact of oxygen deficiencies have been reported to influence its magnetic properties, where with increase in oxygen deficiency there is decrease in ferromagnetism.[18] The mechanism by which this occurs is speculated to be a change in the valence state of Fe ions; increase in oxygen deficiency leads to a decrease in Fe^{4+} and increase in Fe^{3+} ions. Evidence suggests this explanation is sound, due to the associated increase in the lattice spacing due to a decrease in oxygen vacancies (more metal ions with higher valence state have larger radius).[17-20] $BaFeO_3$ thin films lack a comrehensive understanding regarding the nature of its structural and magnetic properties. $BaFeO_3$ could be alloyed with other magnetic preovskites, such as $BiFeO_3$, to yield interesting multiferroic properties.

$BiFeO_3$

$BiFeO_3$ is a multiferroic material that exhibits ferroelectricity and antiferromagnetism in the same phase. It is currently one of the most studied multiferroic materials. Bulk $BiFeO_3$ exists as a distorted perovskite structure, with the rhombohedral polar space group R3c.[23, 24] The space group R3c allows for $BiFeO_3$ to exhibit ferroelectricity.[25-27] The rhombohedral unit cell contains two connected $BiFeO_3$ perovskite formula units, with the two oxygen octahedra tilted by + and – 13.8°.[28] In bulk, single crystal $BiFeO_3$ can exhibit a spontaneous polarization in excess of 100 $\mu C\ cm^{-2}$.[29] The ferroelectricity in $BiFeO_3$ can be explained by lone pair mechanism of the Bi ions.[30] Its polarization occurs along the [111] direction, and it is ferroelectric below $T_C = 1143$ K.[31, 32] $ABiFeO_3$ is also magnetic, exhibiting G-type antiferromagnetism below a Neel temperature of 643 K. It is also reported to be weakly ferromagnetic.[31, 33, 34] It was found that this weak ferromagnetism can be attributed to a complex magnetic spiral[35], or helimagnetic structure discovered by Sosnowska *et al*[33] using high

resolution time-of-flight neutron diffraction. The spiral structure is stable at most temperatures below the T_C.[33] Research on the variation of strain and thickness effects of epitaxial films of $BiFeO_3$ grown via pulsed laser deposition show that the polarization does not exhibit large change in size, despite distinct crystallographic changes in structure.[36, 37] $BiFeO_3$ has been grown on (100) or (111) oriented single crystal perovskite substrates, and has a large polarization of 100-115 $\mu C/cm^2$ in the [111] direction, similar to the bulk.[36-38] $BiFeO_3$ is interesting to study because it can be used as a lead-free ferroelectric and multiferroic material for nanoscale devices.[4, 38-41]

Multiferroics Compounds and Composites

There is growing interest in materials that have both magnetic and electronic functionality. In principle, these materials could enable single device components to perform multiple functions. Multiferroics with coupled ferroelectric and ferromagnetic properties, so-called are magnetoelectrics, are particularly attractive, enable new concepts such as electric-field controlled magnetic data storage devices.[40] A magnetoelectric material could exhibit a spontaneous magnetization that can be reoriented with an applied electric field, or a spontaneous polarization that can be reoriented with an applied magnetic field. Coupling these phenomena adds significant versatility to current device applications in data storage.[40, 42]

Multiferroic materials are uncommon in bulk materials. Some possible restricting factors have been theoretically discussed. N. A. Hill [3] suggested that d-orbital occupancy of the B-site cation in perovskite materials is a critical variable in reducing the propensity for perovskite materials to exhibit ferroelectricity. This consequence reduces the chance for magnetoelectric multiferroics, unless there are additional influences that allow for this phenomenon. Single-phase multiferroics were first identified in 1958. Currently there are more than 80 known single-

phase multiferroics. There are four major categories of single-phase multiferroics as reported by Fiebig:[42]

1. Perovskite structure materials (ABO_3 or $A_2B'B''O_6$) that have slightly deformed cubic symmetry can be multiferroic. One example of this kind of material is $BiFeO_3$, a ferroelectric, ferroelastic, and weakly ferromagnetic compound. Various solid solutions based on this compound have been made due to interest in its high electric and magnetic ordering at high temperatures.

2. Hexagonal structure materials that have the same stoichiometric formula as perovskite but crystallize in hexagonal structure can also be multiferroic. These mainly consist of manganites with formula $RMnO_3$ where R = Sc, Y, In, Ho, Er, Tm, Yb, or Lu. The point group they possess is 6mm. These compounds are ferroelectric with an antiferromagnetic Mn^{3+} sublattice.

3. Boracites ($M_3B_7O_{13}X$) are ferroelectric, ferroelastic antiferromagnets, that sometimes also have a weak ferromagnetic moment. The range of bivalent ions can be M = Cr, Mn, Fe, Co, Cu, Ni and the anions, X = Cl, Br, or I. These solid solutions have ferroelectric $T_C >$ 300 K. However the magnetic transitions occur below 100 K.

4. $BaMF_4$ compounds where M = Mg, Mn, Fe, Co, Ni, Zn, are ferroelectric ferroelastic with solely antiferromagnetic or weak ferromagnetic ordering. These solid solutions have 2mm point symmetry at high temperatures and their melting temperature is less than their Curie temperature.[3, 42]

Although multiferroic phenomena are observed in these materials, they are of little utility for applications due to the temperature range of the coupled phenomena or the nature of the magnetic ordering (i.e. antiferromagnetic).[40]

Several groups have examined nanostructured materials as potential multiferroics. For example, self-assembled $BaTiO_3$-$CoFe_2O_4$ nanocomposites have been studied by Zheng *et al*[43] and are shown in Figure 2-2. The structures consist of $CoFe_2O_4$ nanopillars that are grown perpendicular to a $SrTiO_3$ substrate, with the pillars embedded in a $BaTiO_3$ matrix. This self-assembled matrix is a spinel/perovskite structure grown from a single $0.65BaTiO_3$-$0.35CoFeO_4$ target by pulsed laser deposition. The authors proposed magnetoelectric coupling through magnetorestriction, a mechanism where there is strong elastic interactions between the two phases. One of the interactions comprised of the $BaTiO_3$ matrix's ferroelectric structural

distortion from cubic to tetragonal phase which caused a compressive strain in $CoFe_2O_4$ nanopillar along its axis. A drop in the magnetization at the ferroelectric T_C was quoted as evidence for magnetoelectric coupling.[43]

Motivation for thin film artificial superlattices for multiferroics has increased over the past decade, benefiting from the ability to achieve well-defined interfaces at the atomic level. The interfaces comprised of a magnetic and ferroelectric material layered on one another has great advantage over bulk materials because of manipulation of electron-mediated magnetic dipole ordering. As shown in Figure 2-3, lattice strain effects, dimensionality, and stacking periodicity are some of the key parameters that can be controlled. Tabata *et al*[44] suggested that superlattice structures can realize the following:

1. Strain Effect; lattice stress can be introduced at the interface
2. [Reduced] Dimensionality; first layer is isolated by the second layer with changing thickness of the second layer
3. Stacking periodicity (cycles); it is like a sharp superlattice in semiconducting devices. [44]

There are two kinds of strain that can occur in a multilayer structure: the interface between the film and the substrate, and the interface between the two distinct materials used to create the multilayers. Thus, one can expect a variation of strains in a multilayer system. In multiferroic systems, compressive (or tensile) strain at the interface can suppress (or enhance) multiferroic coupling. With reduced dimensionality, the thickness of the layers can pose variation in the measured property of interest. An enhancement or suppression of coupling can also occur with changing thickness of one or both layers. Variation of stacking periodicity can tune the transition temperature of the material property of interest.

In recent years, superlattices have offered novel approaches to creating new materials that can be tailored depending on the kind of layer materials, thickness, morphology, and layer

interfacial structure. One or more of these factors varied do in fact govern the electronic and magnetic properties.[45] There are some groups that have succeeded in fabricating ferromagnetic/ferroelectric hetero-epitaxial layers. Mentioned here are a few studies in recent years of ferromagnetic/ferroelectric thin films assembled via pulsed-laser deposition.[46-49]

Murugavel *et al* [48] chose ferromagnetic $Pr_{0.85}Ca_{0.15}MnO_3$ (PCMO) and ferroelectric $Ba_{0.6}Sr_{0.4}TiO_3$ (BST) to fabricate artificial thin film superlattices. They chose PCMO because it appears to be ferromagnetic and insulating which is uncommon and BST for a minimum lattice mismatch with PCMO. They observed an increase in magnetoresistance in the samples with increasing ferroelectric layers as well as magnetization and dielectric constant as a function of temperature, indicating that superlattices could have coexistence of ferromagnetic and ferroelectric properties.[48] Another group[50] created multilayers of ferroelectric $BaTiO_3$ (BTO) and ferromagnetic $La_{0.7}Ca_{0.3}MnO_3$ (LCMO). They varied the thickness of the BTO layers while keeping LCMO layers constant at a thickness where it behaves as an insulating ferromagnet. They revealed that the total magnetization increased as the BTO layer thickness is increased. However the Curie temperature of the films were almost independent of BTO thickness. In addition, they obtained successful measurements of high magnetocapacitance and large magnetoresistance, which they claim will be useful in designing optimal multiferroic thin films.[50]

Multiferroic Solid-Solution Epitaxial Films

There has been much work on "enhancing" the magnetic properties of single phase multiferroic materials that exist, for example by substitution and doping of A-site and/or B-site cations.[51-71] $BiFeO_3$–based solid solutions have recently become of increasing interest, as research groups look to make this antiferromagnetic ferroelectric exhibit "maximum strength" magnetism without compromising the integrity of its robust ferroelectric properties.[54, 56-61] Only a few groups have investigated the properties of A- and/or B-site cation substitution on bulk

$BiFeO_3$,[54-59, 62-64] and few articles have been published on A- and/or B-site cation substitution in $BiFeO_3$ epitaxial thin films.[60, 61, 70, 71]

A-site cation substitution is of importance in $BiFeO_3$ because the doping or substitution of certain elements may cause a change in the magnetic structure.[72, 73] However, this is not an easy task, taking note that even the synthesis of single phase $BiFeO_3$ in bulk or thin film is rather difficult achieve, due to many factors, including the volatility of Bi ions, narrow window of epitaxial deposition constraints, and numerous impurity phases.[31, 35, 74] In addition, by adding another solid solution in the system, one may can prevent the formation of second phases and improve the resistivity of $BiFeO_3$.[32, 51, 55, 75]

Some groups have utilized isovalent cations, many of which are rare earth elements such as Gd, Nd, Sc, La, and Ce, as an A-site substitution.[54-61] Some have put in as little as 5%, and at most 40% substitution for Bi. Khomchenko *et al* showed that by adding up to 30% Gd to bulk $BiFeO_3$, the room temperature magnetization changed to weakly ferromagnetic. They claim it was not due to Gd^{3+} ions themselves being magnetic, but that an antisymmetric exchange mechanism was the reason for increase, in addition to a substitution-induced suppression of the spiral spin modulation.[54] Two groups studied the effects of substitution of Lanthanum (La^{3+}) into bulk $BiFeO_3$. Zhang *et al* claim that adding La^{3+} induced the destruction of the spin cycloid, and hence resulted in a magnetization two times that of "pure" $BiFeO_3$. The second group, Das *et al*, demonstrated that the presence of a small secondary phase in $BiFeO_3$ was removed upon La substitution at the Bi site, which meant that stabilization of the bulk crystal structure was enabled. In addition, they concluded that nonuniformity caused by La substitution enhanced the multiferroic properties of $BiFeO_3$.[56]

As mentioned before, there are only a few articles published for heterovalent A-site substitution in $BiFeO_3$ in the form of thin films,[60, 61, 70, 71] which is not a surprise due to the relatively new general interest in improving multiferroic materials by cation substitution rather than just by growth conditions and substrate choice. Epitaxial films that are grown via pulsed laser deposition have proven to be relatively advantageous. This is due to the "ease" at which many materials can be grown with stoichiometric transfer of atoms onto a single crystal substrate. Two groups in particular have grown the same A-site substituted material, $(Bi_{0.6}Tb_{0.3}La_{0.1})FeO_3$ via pulsed laser deposition, and a third research group synthesized this material as a bulk ceramic.[63, 70, 71] The findings of Palkar, *et al* of bulk $(Bi_{0.825}Tb_{0.075}La_{0.1})FeO_3$ were a decrease in the ferroelectric transition temperature (they ascribe this to the addition of Tb^{3+} which causes a decrease in the unit cell volume), and a room temperature magnetization increase to $4\mu_B$ per Tb ion.[63] This is the largest magnetization reported for a multiferroic material.

A second group, Wang *et al*, grew epitaxial films of $(Bi_{0.6}Tb_{0.3}La_{0.1})FeO_3$ and reported that growing at very low pressures removes the presence of impurity phases (an $BiFeO_3$ orthorhombic phase and a ferric oxide) and increases the crystallinity, in addition to decreasing the leakage current at electric fields higher than 50 kV/cm.[72] The authors believe the cause of leakage current is a small amount of Fe^{2+} ions or oxygen vacancies. They concluded the cause was the presence of oxygen vacancies and observed that doping $BiFeO_3$ with Ti^{4+} ions decreased the leakage in those films, indicating that oxygen vacancies was the main cause.[76] The authors also *ex situ* annealed the films in oxygen ambient atmosphere and measured the lowest leakage current ever reported in literature on pure or doped $BiFeO_3$ thin films.[72]

An additional report on $(Bi_{0.6}Tb_{0.3}La_{0.1})FeO_3$ by Eerenstein *et al*[70] attempted to reproduce data produced by the previously mentioned articles and explain their own observations. First, they addressed the problem of large variation of measured $BiFeO_3$ polarization (between 2 and 150 $\mu C/cm^2$), especially groups measuring polarizations in excess of 100 $\mu C/cm^2$. They state that to determine if a measured polarization is valid, frequency-dependent measurements and leakage density (acceptable values are below 10^{-5} A/cm^2) should be reported with polarization measurements. In addition, Eerenstein *et al* challenged the claim of a ferromagnetic moment of $4\mu_B$ per ion.[63, 70] They reported results where the magnetization increases from $0.05\mu_B$ per unit cell in undoped $BiFeO_3$ films to ~$0.08\mu_B$ per unit cell for $(Bi_{0.6}Tb_{0.3}La_{0.1})FeO_3$. They concluded that it is possible that the large value reported was due to iron oxide impurities due to Bi loss. They also added that the large room temperature moment cannot be explained by A-site magnetic order, because this is only expected as low temperatures (< 5 K). Also, other rare earth substitutions[54-61] show only weak magnetism.[70]

To conclude, there is much interest in A-site substitution of $BiFeO_3$ in manipulating the complex properties of this multiferroic material.

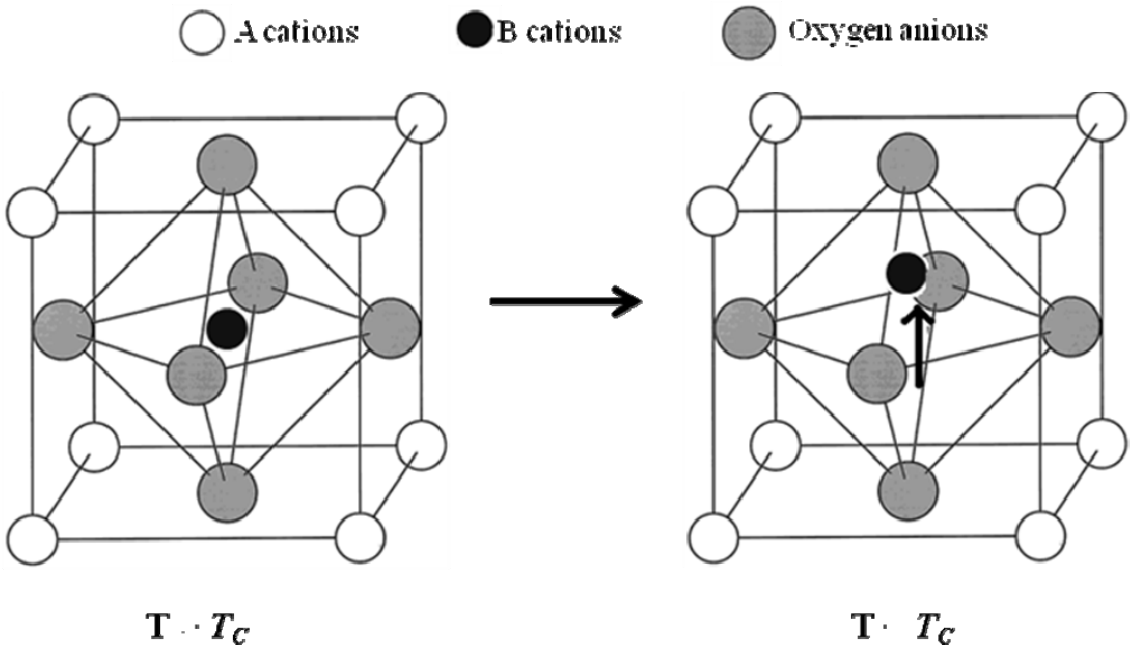

Figure 2-1. Schematic of perovskite structure. In some ferroelectrics, the B cations shift off position.

Table 2-1. Single phase multiferroics with various properties.

Compound	Structure	Point Group(s)	Properties	Example
Perovskite	ABO_3 or $A_2B'B''O_6$	3m	FE, FEL, (A)FM	$BiFeO_3$, $PbFe_{0.5}Nb_{0.5}O_3$
Hexagonal Manganites	$RMnO_3$	6mm	FE, AFM	*R* = Sc, Y, Ho, Tm, In
Boracite	$MB_7O_{13}X$	High T: bar43m Low T: 3m or m	FE, FEL, (A)FM	*M* =Ni, Co, Cr *X* =Cl, Br, I
$BaMF_4$	$BaMF_4$	2mm	FE, FEL, (A)FM	*M* = Mg, Mn, Fe

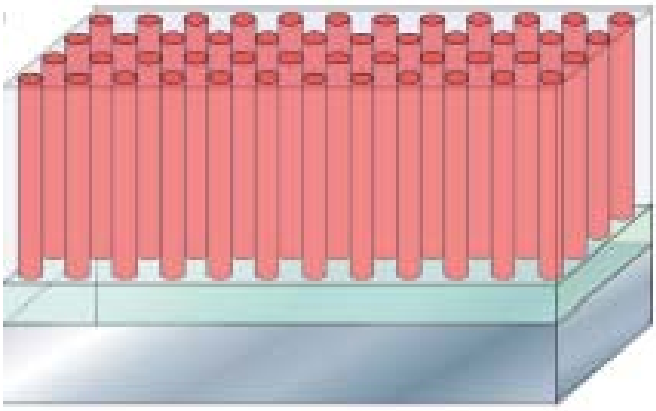

Figure 2-2. Schematic of self-assembled nanostructure thin film aligned perpendicular to substrate.[43]

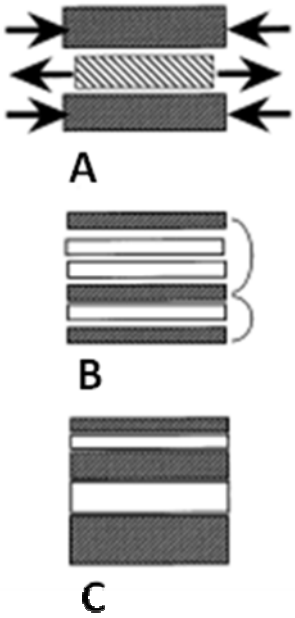

Figure 2-3. Variation of layering in an artificial superlattice. A) Strain: Lattice stress can be introduced at the interface; B) Dimensionality: black layer is isolated by the white layer with changing thickness of the white layer; C)Stacking: change in the number of cycles.[44]

3. METHODOLOGY

Synthesis of Thin Films

Pulsed Laser Deposition (PLD) is a thin film growth technique that is conceptually simple. The apparatus consists of a target holder and substrate holder located inside a vacuum chamber. A laser is used to ablate materials from the target and deposit on substrate(s) mounted to the substrate holder. Film growth can be carried out in almost gas environment with or without plasma excitation.[77] A brief history, specific equipment used, and technique of PLD will be briefly explained here.

After the first high-power ruby laser became available, many experimental and theoretical studies of interactions of intense laser beams on solid surfaces, liquids and gaseous materials came about.[77, 78] It wasn't until the demonstration of epitaxial growth of high T_C superconducting films in 1987 that PLD emerged as a significant growth technique in research.[77-79] One of the advantages of PLD is its capability to explore almost any materials systems. Unlike other systems, the energy source of PLD, the laser, is independent from the deposition chamber system, making PLD a simple technique to create complex epitaxial films.[77] In addition, the ability to realize stoichiometric transfer of ablated material from multi-cation targets shows that almost any material that exists in the bulk form can be grown by PLD.[78, 80] There are several growth conditions of importance that include target-substrate distance, ambient gases, laser energy, and substrate temperature. Laser wavelength is important in the use of PLD. To efficiently ablate target material, temperatures of the ablated volume must be well above what is required for evaporation of species. Thus the laser pulse should have short duration, be high in energy density, and highly absorbed by target materials. Specifically for ceramic targets, ultraviolet wavelength lasers are optimal for achieving deposition.[78] Generally, laser wavelengths for PLD exist between 200 and 400nm. Table 3-1 shows different excimer laser

operating wavelengths. Most PLD research has been executed with excimer or frequency-converted Nd^{3+}:YAG (Yittrium Aluminum Garnet) lasers as the energy source. For a high-quality deposition, the laser output must have uniformity; hot spots and non-uniformity must be avoided, especially in the use of multi-component deposition targets. Non-uniformity in laser output can lead to particle formation on the substrate, or non-stoichiometry in the film. The KrF and XeCl excimer lasers are the most extensively used lasers for PLD.[77]

In PLD, the laser pulse is absorbed by the target creating an ablation plasma. The effusion layer (plume) expands out from the target, mostly perpendicular to the surface. The atoms acquire a large flow velocity in the surface normal direction towards the heated substrate.[81]

The $BaFeO_3$ ablation targets were synthesized from $BaCO_3$ (99.997%) and Fe_2O_3 (99.998%) powders that are crushed and dry-mixed in a high density alumina mortar and pestle set for 45 minutes. The powder mixture was placed in a covered high density alumina boat and calcined in a box furnace in air in the following sequence:

$$RoomTemp(RT) \xrightarrow{4hrs} 800°C \xrightarrow{2hrs} 950°C \xrightarrow{6hrs} 950°C \xrightarrow{5hrs} 25°C(RT)$$

After removal, the powder mixture was put in a ball mill and mixed dry for 30 minutes, or dry-mixed a second time with alumina mortar and pestle set. Then the mixed powders were cold pressed into a 1" diameter pellet with a stainless steel die and held under 2000 lbs psi for 2 minutes and then placed again in a box furnace in air and set to sinter in the following sequence:

$$RoomTemp(RT) \xrightarrow{4hrs} 1000°C \xrightarrow{12hrs} 1000°C \xrightarrow{5hrs} 25°C(RT)$$

The target is then checked for hardness and polished with sand paper to ensure a flat surface for even laser ablation. (Bi, Ba)FeO_3 solid solution targets were synthesized using the same conditions as $BaFeO_3$ targets, but with an extra step in the process where Bi_2O_3 was added right after the $BaFeO_3$ mixture was calcined. Due to the volatility of bismuth, the calcining and

sintering temperatures were 100 degrees less than that of $BaFeO_3$. In addition, 10% excess Bi_2O_3 was added to account for Bi loss during sintering and deposition.[78] Three targets: $SmScO_3$, $SrTiO_3$, and $KTaO_3$ targets were obtained from other sources.

Growth Procedure

The ceramic target is loaded into the deposition chamber on a target carousel. The pulsed laser is focused through a series of mirrors and lenses, eventually through the deposition chamber window onto the rotating target.[82] Film deposition occurs on the heated substrate.

The substrates utilized in this work are $SrTiO_3$ (100), $LaAlO_3$ $(100)_{pc}$, $KTaO_3$ (100), $NdGaO_3$ $(100)_{pc}$, $DyScO_3$ $(100)_{pc}$, and $(La_{0.29},Sr_{0.71})(Al_{0.65},Ta_{0.35})O_3$ (LSAT) $(100)_{pc}$ single crystal substrates. Although $LaAlO_3$ is rhombohedral at room temperature, it is a cubic perovskite at the growth temperatures and can be indexed as a perovskite pseudo-cubic with a_0 = 3.789 Å at room temperature. Prior to growth, the substrates were cleaned with trichloroethylene, acetone, and methanol in an ultrasonic bath, followed by drying with dry nitrogen. In order to remove any trace metals that might introduce spurious magnetic properties, the unpolished backside of the substrate was etched with a 50/50 solution of HNO_3 and distilled water.

The base pressure of the deposition is maintained at 10^{-7}-10^{-9} Torr, with various growth pressures maintained between 0.1-300 mTorr Po_2. Oxygen and Nitrous Oxide flow rates are 1-2 sccm. The temperatures of the substrates mounted on substrate holders during growth are 600-900°C respectively. Laser ablation energies are between 2-3 J/cm^2 with a pulse rate of 5 or 10 Hz for $BaFeO_3$ epitaxial films, and 1.68 J/cm^2 at 50 Hz for continuous-target-rotation mechanism for solid solution thin films.

Some of the epitaxial films were grown using a two-target continuous rotation method. This method is used to create solid solution or alloy epitaxial films via the use of two targets,

instead of making a new target of the desired composition. Before deposition, the desired solid solution composition is calculated, to know how many shots per end-member target is needed, and how many repetitions are required for the desired thickness. In the deposition chamber, two targets are placed opposite from each other on the target carousel, and routine preparations are completed prior to deposition. The program will command the entire target carousel to rotate at a certain speed, and laser pulses will strategically hit each target with a certain number of pulses at determined frequencies to create alloy mixing. This method, when modified, can also be used to create artificial superlattices.

Characterization

The magnetic properties of the samples are investigated by using Superconducting Quantum Interference Device (SQUID) Magnetometry.[7, 8, 83, 84] Magnetic properties can be determined by examining how the magnetization changes versus temperature and applied field. To accurately measure the magnetization of the film, substrates were measured with SQUID, and their diamagnetic (or in some cases paramagnetic) response was subtracted as the background from the actual sample's measurement. This was accomplished by taking the magnetization versus field data, and dividing this by the mass of the reference substrate. Then these values were subtracted from the sample data, and the data was multiplied by the sample's actual mass.

X-ray Diffraction (XRD) is a technique used to measure the structural properties of a material such as strain, epitaxy, phase composition, preferred orientation, and defect structure. Crystals are made of planes of atoms that are spaced a distance, d, apart, each family of planes has a different d-spacing from one another. To differentiate these planes, a coordinate system such as an orthogonal system for a simple cubic crystal can be uniquely distinguished by its Miller Indices. The Miller Indices with the a, b, and c crystallographic axes, are the reciprocal

intercepts of the plane reduced to the smallest integers having the same ratio.[85] An (hkl) plane intercepts the axes at a/h, b/k, and c/l. Thus the d-spacing between (hkl) planes is d_{hkl} for simple cubic crystals, where

$$d_{hkl} = \frac{a_0}{\sqrt{h^2 + k^2 + l^2}}, \quad \text{(3-1)}$$

Here in Eq. 3-1, a_0 is the lattice constant of the crystal.[85]

In X-ray diffraction, Bragg's law gives the condition for which a diffraction peak can be observed from the constructive interference from x-rays scattered by atomic planes in a crystal:

$$\lambda = 2d_{hkl} \sin\theta_{hkl}, \quad \text{(3-2)}$$

In Eq. 3-2, θ_{hkl} represents the angle that is between the planes and the incident and diffracted x-ray beam. To observe a diffracted plane, the detector must be positioned so the diffraction is $2\theta_{hkl}$. In addition, the crystal should be oriented so that the normal to the diffracting plane is coplanar with the incident and diffracted beams, so that the angle between them is equal to the Bragg angle θ_{hkl}. Only one specimen orientation is possible for each (hkl) plane in single crystals and epitaxial films.[83, 85]

Reciprocal Space Maps (RSMs) are two-axes measurements that produce a two- or three-dimensional "map" of the epitaxial film and substrate, mostly with off-axis planes. These scans are incredibly useful because calculation of the out in-plane as well as out-of-plane lattice parameters can be obtained. Using the substrate as the reference point, the peak distance differences (or mismatch) from the substrate to the film is measured. The parallel mismatch the difference taken from the x-axis and perpendicular mismatch is taken from the difference of the y-axis. For more accuracy, one can take into consideration the average of the $K\alpha_1$ and $K\alpha_2$ peaks. These differences can be converted to lattice constants when the lattice constant of the

substrate is known. On reciprocal space maps one can identify whether a film exhibits strain or relaxation and to what degree, with respect to the substrate.

Two-theta (2θ) scans can determine the unique d-spacings of crystalline materials and specifically show out of plane peak intensities, which is proof of epitaxy. In this project specifically, the perovskite materials studied will show (00*l*) peak intensities. Omega (ω) Rocking Curve scans will "oscillate" about a chosen d-spacing on the 2-theta/2 axis (or omega) and the information determined is the crystallinity of the sample. The breadth of the rocking curve or Full-width-at-half-maximum (FWHM) will determine the distribution of the crystalline grains. A narrow rocking curve (FWHM $\leq 0.5°$) means the film is highly crystalline, whereas a FWHM greater than 0.5° is poorer crystalline quality. Single crystal substrates always yield a FWHM of less than 0.08°. Phi scans verify or identify the symmetry of the material measured. In addition, specific families of planes of single crystal substrates can be determined.

Components used in the study

In this work, a couple of diffractometers were used: a Phillips APD 3720 two-circle x-ray diffractometer for films grown in Chapter 4, and a Pan Alytical four-circle x-ray diffractometer for films grown in Chapters 5 and 6. In the four-circle diffractometer, a mirror was used (which limits peaks to the presence of $K\alpha_1$ and $K\alpha_2$ peaks. Also slits of ¼" and ⅛" were used in measurements.

A scanning electron microscope (SEM) was used to obtain topographic images and elemental analysis of materials. It has a magnification range of 10-10,000×, and most elements can be identified using the electron dispersive spectrometer portion of the SEM. The SEM's instrumental resolution is generally on the order of 10-50 Angstroms; as well it has a large depth of field, which is responsible for the three-dimensional appearances of sample imaging. Overall the SEM's most important use is for structure analysis and elemental analysis.[86] Due to

bombardment of electrons onto the sample during SEM, if the sample is nonconducting, (or insulating) the sample may exhibit a phenomena called “charging.” To overcome this problem, samples can be prepared by coating them. In this work, samples were coated with Carbon, using an SPI Sputter Coater. In this work, ceramic target powder samples were examined using a Hitachi S4800 FEG SEM, located in the High Temperature Materials Laboratory (HTML) at Oak Ridge National Laboratory. As stated earlier, most target powder samples were coated with carbon, and their chemical composition and surface were analyzed.

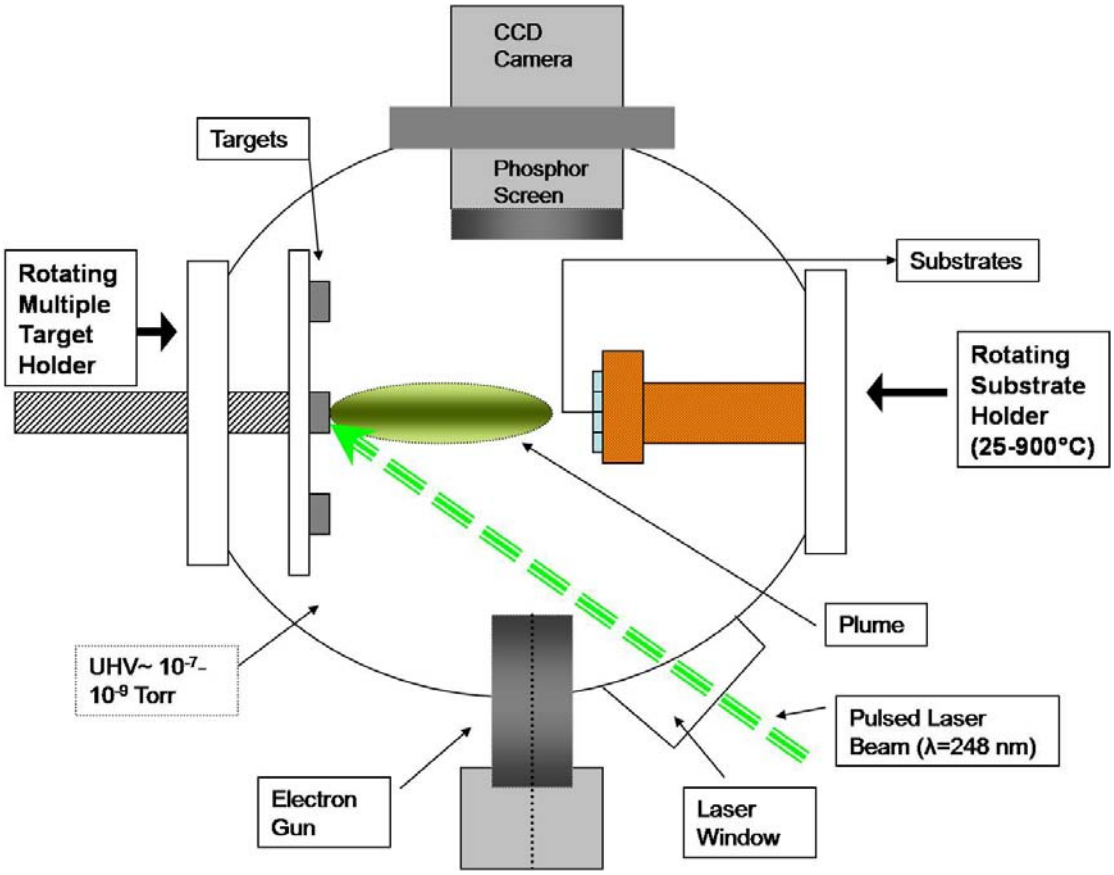

Figure 3-1. Schematic of Laser MBE Growth Chamber Setup

Table 3-1. Excimer Laser Operating Wavelengths

Excimer	Wavelength (nm)
F_2	157
ArF	193
KrCl	222
KrF	248
XeCl	308
XeF	351

FERROMAGNETISM IN PSEUDO-CUBIC $BaFeO_3$ EPITAXIAL FILMS

Magnetic oxide materials[87] have attracted considerable attention due to interest in the fundamental science of magnetic moment interactions, magnetic device applications, and the possibility of creating novel coupling via the formation of nanostructured interfaces.[43, 88, 89] One member of the perovskite oxide family that exhibits unique magnetic properties is $BaFeO_3$. It is one of the few oxides where iron assumes an oxidation state of +4.[16] In bulk, $BaFeO_3$ normally assumes a hexagonal crystal structure (a=0.568 nm and c=1.386 nm), although various polymorphs are observed with oxygen deficiency.[16, 17, 19, 90, 91] The magnetic properties of $BaFeO_3$ are strongly dependent on the oxygen content, presumably affecting the formal valence of the iron cation. Several studies indicate that bulk hexagonal $BaFeO_3$ exhibits an antiferromagnetic to ferromagnetic transition at 160 K, with a ferromagnetic Curie temperature of 250 K.[18] More recent Mössbauer and high magnetic field studies seem to contradict this conclusion, showing that no magnetic ordering occurs for 160 K > T > 220 K.[19] This discrepancy could be related to the different oxygen stoichiometries that $BaFeO_{3-x}$ can assume.[18]

Recent results for epitaxial $BaFeO_3$ thin films indicate that the structural, magnetic and electrical properties of films can be significantly different from that of bulk material.[20, 22, 92] For epitaxy on (001) $SrTiO_3$, $BaFeO_3$ films assume a metastable pseudo-cubic crystal structure similar to that observed for $SrFeO_3$, a material that exhibits antiferromagnetic characteristics with screw spin type magnetic structure and is metallic. This stabilization of a metastable phase via epitaxial growth has been observed for other perovskite-like oxides.[93, 94] Previous reports on pseudo-cubic $BaFeO_3$ films suggest that this phase is ferromagnetic at room temperature,[22, 92] in contrast to the hexagonal bulk phase which is not. This modification of magnetic properties is presumably the result of strain and/or defects in the films. Modification through strain has been observed in a variety of perovskite material properties.[78, 95-97] However, it is unclear how strain

might yield an enhancement in the T_c for magnetic ordering in the Fe^{+4}-O-Fe^{+4} system. The reported lattice constant of the $BaFeO_3$ epitaxial film on $SrTiO_3$ was a=4.120 Å, which is larger than that expected based on anion-cation spacing in bulk materials.[20, 22] Note also that the films were also reported to be highly insulating. At 300 K, magnetization measurements showed hysteresis as well as remnant magnetization.[22, 92]

In this work, the properties of epitaxial pseudo-cubic $BaFeO_{3-x}$ films grown by pulsed laser deposition are examined. The focus of this work is on the variation of magnetic and structural properties as a function of processing conditions that yield variations in oxygen content. As will be seen, the onset of robust ferromagnetism is a strong function of oxygen content, similar to what is seen in the bulk phases.

Experimentation

$BaFeO_3$ thin films were grown on (012) oriented $LaAlO_3$ and (001) $SrTiO_3$ single crystal substrates via pulsed laser deposition.[79, 98] The $LaAlO_3$ substrates were pre-screened in a Superconducting Quantum Interference Device (SQUID) magnetometer to insure that the substrates were "non-magnetic" (no ferromagnetic impurities) and thus suitable for magnetic characterization of the thin films after growth. Deposition preparation was discussed earlier. Laser energy densities on the order of 2-3 J/cm^2 were utilized. Target to substrate distance was on the order of 4 cm. The ablation targets were 1 inch diameter $BaFeO_{3-x}$ ceramics. The thin films were grown at substrate temperatures between 650-850°C and an oxygen pressure ranging from 0.1-100mTorr. Growth time was 60 or 100 minutes. After growth, the samples were cooled at 10°/min in the oxygen partial pressure used during growth.

The crystal structure and orientation of the deposited films were examined by X-ray diffraction (XRD). Magnetic characterization was performed on a SQUID magnetometer, with substrate and sample preparation discussed earlier, as well as details of what sample crystal

orientations the magnetic fields were applied. In some cases, $BaFeO_3$ films were annealed in oxygen in a high temperature tube furnace.

Results and Discussion

As-Deposited $BaFeO_{3-x}$ epitaxial films

Initial studies focused on understanding epitaxy and phase evolution for the in situ grown $BaFeO_{3-x}$ films. Figure 4-1 shows the X-ray diffraction data for films grown on $LaAlO_3$ at temperatures ranging from 650-850°C in an oxygen pressure of 10 mTorr. In all cases, the growth of $BaFeO_{3-x}$ in a pseudo-cubic perovskite structure is observed, although not as a single cubic phase. In particular, the diffraction data show the emergence of two distinct phases. At low temperatures, the $BaFeO_{3-x}$ (200) peak at a 2-theta angle of 44.27° corresponds to a pseudo-cubic lattice parameter of 4.09Å. As the substrate growth temperature is increased, a second peak emerges at 45.13°, corresponding to a lattice spacing of 4.02Å. This could represent the emergence of a second cubic phase with a slightly smaller d-spacing, or a splitting of the peak due to a single, low symmetry phase with different oxygen stoichiometry. Low symmetry phases are seen for $SrFeO_x$ ($2.5 \leq x \leq 3.0$), where there is a cubic ($SrFeO_{2.97}$), tetragonal ($SrFeO_{2.86}$), and orthorhombic ($SrFeO_{2.73}$) progression with changes in oxygen stoichiometry.[99] However, additional in-plane characterization of the crystal structure suggests that the $BaFeO_{3-x}$ films consist of two pseudo-cubic phases with slightly different lattice spacing. This result is consistent with that shown in other work on $BaFeO_{3-x}$ films where shifts in the pseudo-cubic (00l) peaks have been reported.[18, 92] The as-grown $BaFeO_{3-x}$ thin films grown at 10 mTorr were translucent with an orange-tan color at a film thickness of approximately 300 nm. Transport measurements show that the as-grown films were non-conducting. The magnetic properties of the as-deposited $BaFeO_{3-x}$ film were measured at temperatures down to 10K. The magnetization versus applied magnetic field film behavior is shown in Figure 4-2. A small but discernable

hysteresis is seen in the M vs. H plot at 10 K, indicating that these films are weakly ferromagnetic.

Ex situ anneal treatment of $BaFeO_{3-x}$ epitaxial films

In order to investigate the progression of magnetic order with oxygen content, several films were subjected to post-growth annealing in oxygen ambient (1 atm). Films were annealed at varied temperatures of 600°C, 750°C, and 900°C for an annealing time of 1 hour. This annealing treatment induced a decrease in lattice spacing and a decrease in resistance. Figure 4-3 shows the X-ray diffraction scans for a $BaFeO_3$ film grown at 700°C, 100 mTorr O_2 before and after a 900°C anneal in oxygen. Before annealing, the peak at 44.21°, corresponding to a cubic d-spacing of 4.10 Å, could be deconvolved into two closely spaced peaks. After annealing at 900°C, films were measured to be less resistive. The resistivity was on the order of 100-200 ohm-cm. In addition, the color of the films changed from the translucent orange-tan to a reflective brown-black. After annealing, the thin film samples were characterized using x-ray diffraction to quantify changes in structure. After 1-hour annealing of the sample, the peak shifts to 45.13°, which corresponds to a smaller lattice spacing of 4.009Å. Four-circle XRD was used to characterize the in-plane lattice spacing, determined to be 4.0134 Å. The in-plane XRD rocking curve full-width half-maximum was on the order of 4°.

Magnetic properties of Annealed $BaFeO_{3-x}$ Epitaxial Films

Significant changes in magnetic properties were observed with annealing. SQUID magnetometry measurements for the as-deposited and annealed films were performed at 10 K, 100K, and 300K. The magnetization behavior for the as-deposited films considered in Figure 4-2 shows that they display weak ferromagnetic behavior. In contrast, annealing the films in oxygen induces a robust ferromagnetic phase with a stable coercive field. The magnetization as a function of applied magnetic field was measured for $BaFeO_{3-x}$ films grown on $LaAlO_3$ and

$SrTiO_3$ at 600ºC, then annealed in oxygen at 900ºC. These films showed clear hysteresis with a coercive field on the order of 800 Oe. Field-cooled and zero-field cooled magnetization was measured as a function of temperature.

Figure 4-4 shows the magnetization at 5K as a function of magnetic field for films grown on $SrTiO_3$ subjected to various anneals; clearly, the magnetization increases with annealing in oxygen. Figure 4-5 shows the magnetization as a function of temperature for the same films. In this case, a Curie temperature of ~ 235 K is observed. Similar experiments were performed for $BaFeO_{3-x}$ films grown on $LaAlO_3$, although the field cooled/zero field cooled splitting was on the order of 100 K for the film on $LaAlO_3$. The realization of ferromagnetism in fully oxidized $BaFeO_3$ and not in the oxygen-deficient material is consistent with the Kanamori-Goodenough rule for superexchange coupling involving transition metal ions, in which the d^5-d^5 Fe^{+3}—O—Fe^{+3} superexchange interaction should be antiferromagnetic, and the d^4-d^4 Fe^{+4}—O—Fe^{+4} superexchange interaction ferromagnetic.[10,24,25] The difference in magnetic behavior for $BaFeO_{3-x}$ thin films grown on $LaAlO_3$ and $SrTiO_3$ may reflect a strain effect due to the differing substrate/film lattice spacing. Figure 4-6 shows plots of saturation (M_s), remnance (M_r), T_c, and the peak in the zero field cooled data for the $BaFeO_{3-x}$ films grown on $SrTiO_3$. Clearly, the annealing of $BaFeO_{3-x}$ films results in a ferromagnetic phase with a relatively high value of T_c. While these results are inconsistent with earlier reports of ferromagnetic behavior at 300 K for insulating $BaFeO_{3-x}$ films, they do show that robust ferromagnetism is observed for highly oxidized pseudo-cubic $BaFeO_3$ at relatively high temperatures.

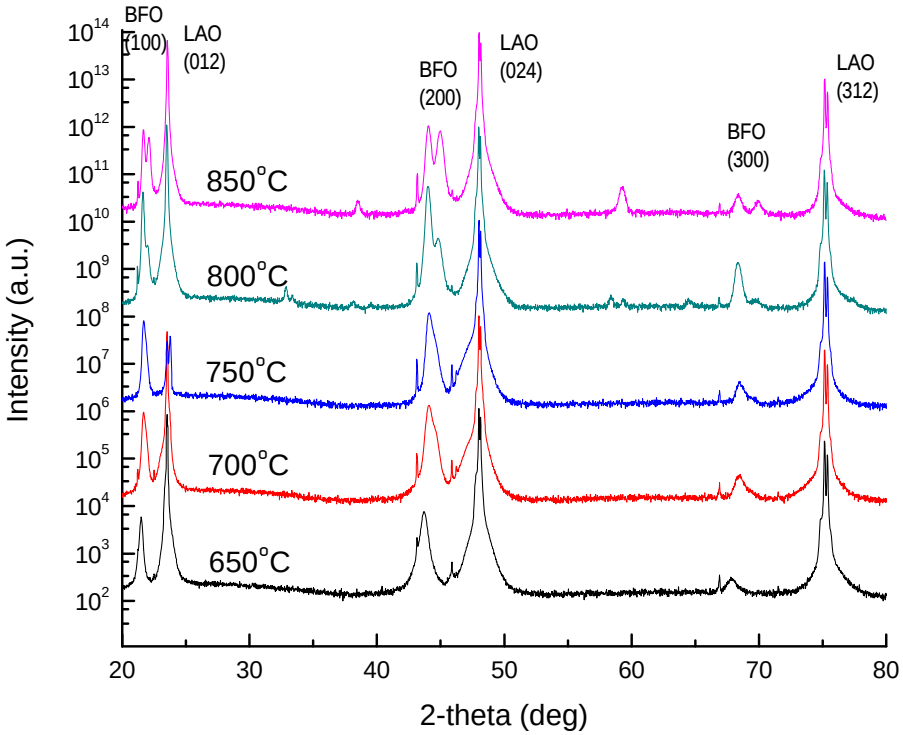

Figure 4-1. X-ray Diffraction data of as-deposited $BaFeO_{3-x}$ epitaxial films with increasing temperature

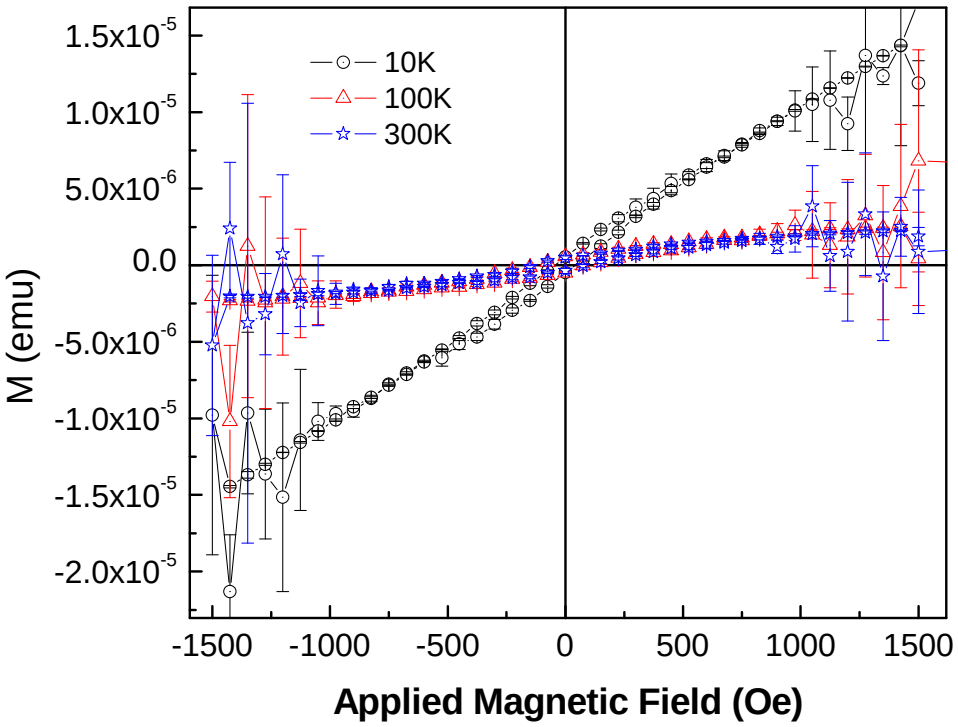

Figure 4-2. Magnetization versus applied magnetic field for as-deposited BaFeO3-x grown at 750°C and 10 mTorr

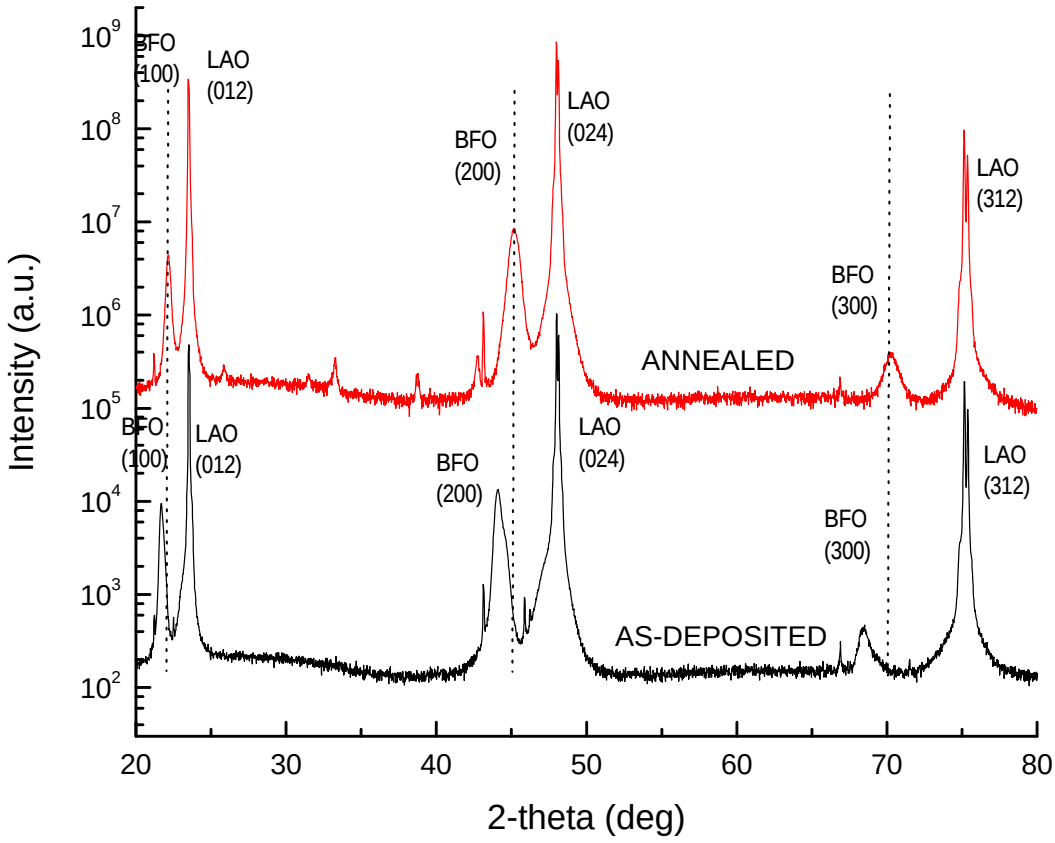

Figure 4-3. X-ray diffraction scans for $BaFeO_{3-x}$ films on $LaAlO_3$, both as deposited and after annealing in 1 atm oxygen for 1 hr at 900°C

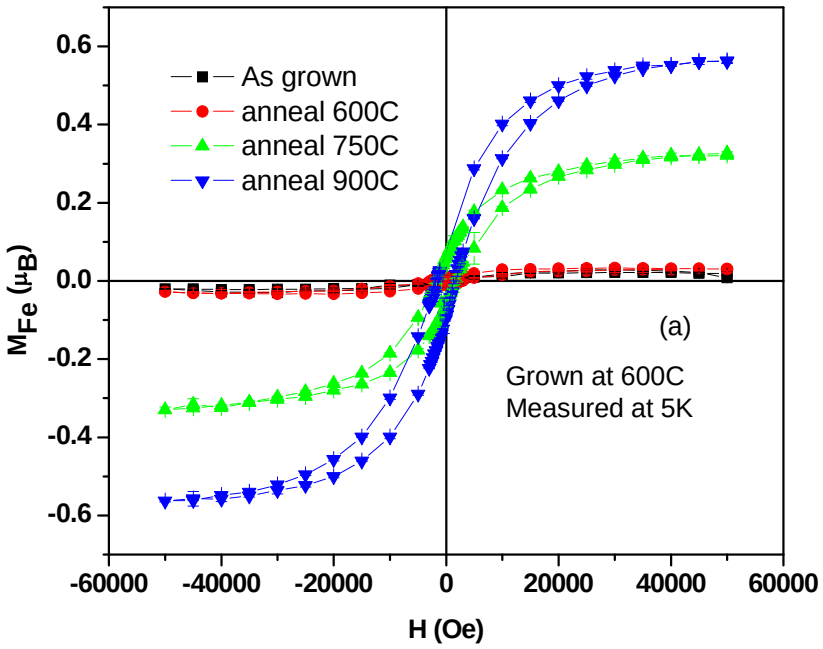

Figure 4-4. Magnetization versus applied magnetic field for $BaFeO_3$ film grown on $SrTiO_3$ (a) at 600°C and 100 mTorr plus annealing in 1 atm oxygen for 1 hr at various temperatures

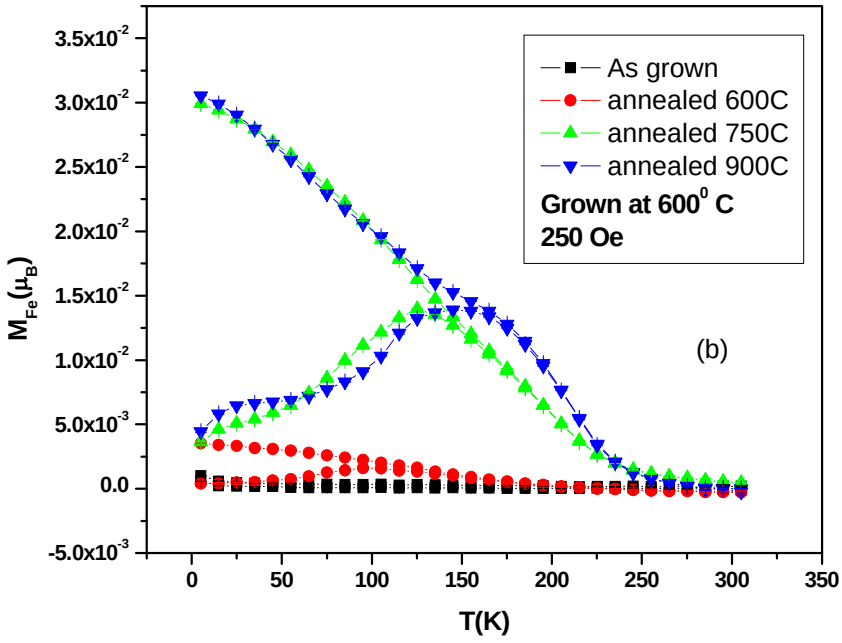

Figure 4-5. Field-cooled and zero field-cooled magnetization as function of temperature for the $BaFeO_{3-x}$ film after annealing in 1 atm oxygen for 1 hr at 900°C. The data are taken in a perpendicular field of 30 kOe

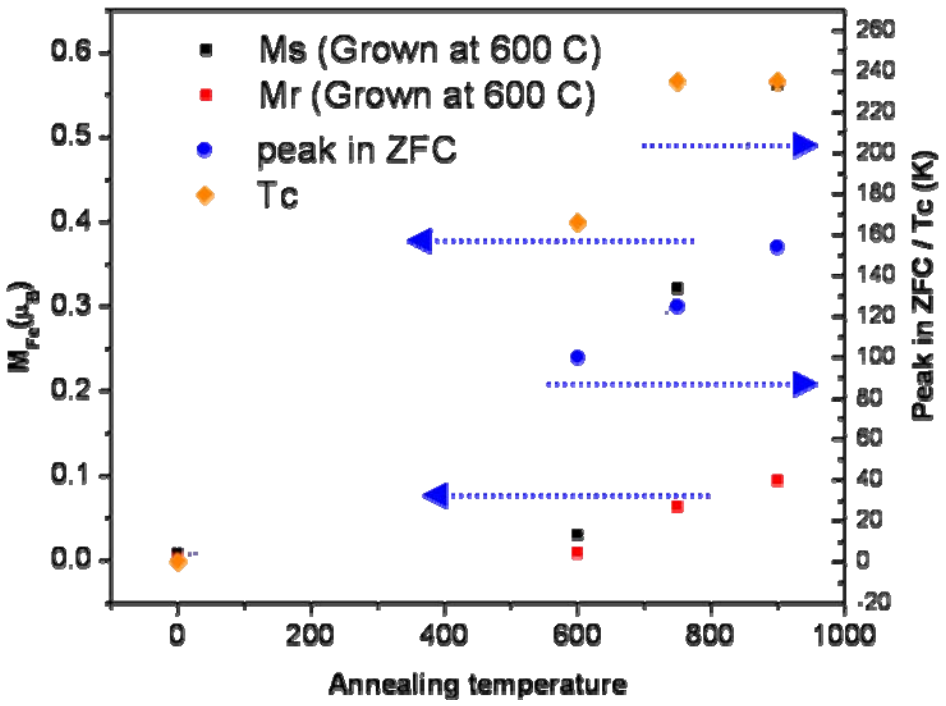

Figure 4-6. Magnetization results for $BaFeO_3$ films on $SrTiO_3$ showing remanence magnetization, saturation magnetization, zero-field behavior and T_C as a function of annealing temperature.

5. STRUCTURAL CHALLENGES WITH $BaFeO_{3-X}$ EPITAXY

In the previous chapter, the structural and magnetic properties of $BaFeO_{3-x}$ were investigated and discussed.[100] There are many reports on the investigation of oxygen content and various annealing processes in the synthesis of perovskite oxides via pulsed laser deposition.[101-104] These anneal treatments of perovskite compounds include *in situ* anneal after growth, *ex situ* anneal in oxygen ambient environments, and growth in various background gases and mixtures to achieve fully stoichiometric compounds.[78] However, little research has been done on the effect of oxygen content in ferrite perovskite films.[90, 105, 106]

The growth and characterization of epitaxial $BaFeO_{3-x}$ thin films grown via pulsed laser deposition was investigated in detail in an attempt to investigate possible stabilization of its oxygen rich phase as grown, as opposed to growth and annealing of these films. In addition, efforts to examine the material challenges that arise after post-annealing, for example: thickness issues, films cracking, and forced stabilization via artificial heterostructures, are illustrated. Also, other research group claims concerning the directional dependence of magnetic moments will be addressed.[20]

Experimentation

$BaFeO_{3-x}$ thin films were grown on $DyScO_{3pc}$ (3.94Å), $SrTiO_3$ (3.905 Å), $LaAlO_{3pc}$ (3.789 Å), and $KTaO_3$ (3.989 Å) single crystal substrates via pulsed laser deposition. Laser energy densities on the order of 1.4-1.6 J/cm^2 and 1.67 J/cm^2 were utilized. Though these fluences are similar, the laser energies (in mV) were 580-650mV (high laser energy) and 300mV (low laser energy). The ablation targets were 1 inch diameter $BaFeO_{3-x}$ ceramics. The thin films were grown at substrate temperatures between 700-750°C and an oxygen pressure ranging from 10-500mTorr. After growth, the samples were cooled at 10°/min (and in some cases 20°/min) in the oxygen or nitrous oxide partial pressure used during growth and in some cases *in situ* annealed in

at a higher oxygen pressure for 1 hour and then cooled in the *in situ* annealing pressure. Most films were *ex situ* annealed in a tube furnace with oxygen flowing, at an anneal temperature of 900°C. Also $BaFeO_{3-x}/SrTiO_3$ artificial superlattice films of varying periodicities were grown, and in some cases *ex situ* annealed in oxygen ambient atmosphere.

The crystal structure and orientation of the deposited films were examined by X-ray diffraction (XRD). To examine effects of annealing on thickness, images of the sample surface were taken using an OptiPhot Light Optical Microscope. Magnetic characterization was performed on a SQUID magnetometer. Details of substrate and sample preparation were discussed earlier.

$BaFeO_3$ epitaxial films grown at low laser energy

$BaFeO_{3-x}$ epitaxial films grown on $DyScO_3$, $SrTiO_3$, $LaAlO_3$ single crystal substrates were grown at 700°C with varied growth pressures (Po_2) and cooled at 20°/min in the various growth pressures. It is apparent that when grown at lower laser density, the films are of high crystalline quality. Shown in Figure 5-1 are x-ray diffraction data, particularly two-theta scans of $BaFeO_{3-x}$ epitaxial films grown on $SrTiO_3$ at the same low laser energy at various pressures. Rocking curves with FHWM values are demonstrated in Figure 5-2. The crystalline quality of the films increases with decrease in pressure, as evidenced by the rocking curve widths. To have the films exhibit ferromagnetic behavior, they are annealed, as stated in the previous chapter. When these films grown at low laser fluency are annealed, they decompose (or degrade) into Fe_2O_3 and BaO. Because of this decomposition, further investigations such as magnetization measurements are unwarranted. A brief explanation for this phenomenon will be elaborated on later.

$BaFeO_3$ epitaxial films grown at high laser energy

$BaFeO_{3-x}$ epitaxial films were grown at high laser energy on $SrTiO_3$, $LaAlO_3$ and $KTaO_3$ single crystal substrates. The growth temperature and pressure was 700°C at 100mTorr and

cooled at 10°/min in the growth pressure. Most films were *ex situ* annealed at 900°C in oxygen ambient environment, and in some cases, films were post *in situ* annealed.

These films, when annealed, do not decompose. They still have rather larger rocking curve widths of one degree on average. Also, after the films were annealed, when examined under a microscope, the films showed directional "hatches" or "cracks." Shown in Figure 5-3 are optical light microscope images of the surfaces of as-grown and post-annealed films at various thicknesses. The estimated thicknesses (in nm) were 300, 502, 1004, 1580, and 2610. At the second lowest thickness shown on Figure 5-3B, there are cross marks that occur in a cross diagonal fashion, making the film surface look textured. There is "cracking" in small areas which start to occur at 502nm in film thickness; with increasing thickness, there are increasing areas of "cracking." At the second greatest thickness, shown in Figure 5-3D, the film has significant cracking. This is mainly attributed to a large change in lattice parameter upon annealing. The film "cracks" are due to large compressive strain.

Effects of Film Thickness on Magnetic Properties of $BaFeO_3$

Figure 5-4 shows varying thickness (in number of pulses) of as-deposited films synthesized at various laser energies. Shown are three films with large differences in the number of laser pulses which demonstrate the definite effect that thickness has on the crystalline quality of $BaFeO_{3-x}$ epitaxial films. With this effect noted, the magnetic properties of films at varying thickness were explored. Figure 5-5 indicates the magnetization of five films varying from 1250 to 20,000 laser pulses which correlates to roughly 300 nm to 3,000 nm in thickness. Note that these films were all annealed at 900°C in oxygen ambient. With decrease in film thickness there is decrease in magnetization. As mentioned in the previous section, the higher crystalline films (grown at lower laser fluency) were not "convertible." In this case, "convertible" refers to films that have optimal conditions to easily become magnetic after ex situ annealing. Consistently, the

less thick films, which are also the films with higher crystalline quality, also are more difficult to make magnetic, based on the weaker magnetic moment (and aside from being thinner films). Figure 5-6 shows the trend of magnetization versus thickness of the films. Note that there is a "threshold" or minimum thickness for films to become convertible, in this case, greater than 502nm but less than or equal to 1004nm. In addition, referring back to Figure 5-4, the film grown at 205 nm has a rocking curve width of 0.351°, signaling high crystalline quality, and the film grown at 1004nm has a rocking curve width of 0.725°, evidence of low crystalline quality.

Effects of Oxygen and Nitrous Oxide partial pressure on structure of $BaFeO_3$

Attempts to fully oxidize $BaFeO_{3-x}$ in the as grown state, as opposed to undergoing *ex situ* anneal treatment, were also investigated by using N_2O as the oxidant. Films grown in 100mTorr Po_2 were compared to films grown in 100mTorr P_{N2O}. The following is a discussion on the effects of different partial pressure and substrate choice on structure. In the two-theta scans, there are usually two peaks known as peak A (oxygen deficient) and peak B (oxygen rich) (see for example Figure 4-1). The ratio of the intensities of the two peaks depends on the substrate used and the lattice mismatch. With increasing lattice mismatch, the ratio of the peaks intensities of the oxygen-deficient to oxygen-rich decreases. In Figure 5-6, $BaFeO_{3-x}$ films were grown at the same conditions, but on three different substrates. On $KTaO_3$, there is only one peak visible, the oxygen deficient peak. On $SrTiO_3$ both peaks are visible, with the oxygen-rich peak having a much higher intensity than the oxygen deficient peak. Many films were grown on $SrTiO_3$, but only a few showed opposite ratio intensities. On $LaAlO_3$, the ratios for the most part would be equal or the oxygen-deficient peak would be slightly lower intensity than that of the oxygen-rich peak.

Reciprocal space maps in Figures 5-7 and 5-8 show interesting phenomena as well. Figure 5-7 shows two reciprocal space maps of as-grown $BaFeO_{3-x}$ on STO, grown in 100 mTorr Po_2

and in 100mTorr P_{N2O}. Nitrous oxide (N_2O) promotes high oxidizing conditions. Shown in Figure 5-8 is $BaFeO_{3-x}$ grown on three different substrates in 100mTorr P_{N2O}. These structures all lie on the same c-axis d-spacing, while having different a (=b) axis d-spacing. On STO, the unusual structuring is not strongly present. On KTO, only a single peak remains (signifying the oxygen deficient phase domination). One possible explanation for this could be a chemical separation of some kind and possible phase-specific orientations arising. Table 5-1 shows the lattice mismatch between the two phases of $BaFeO_{3-x}$ and the substrates used and other substrates for further comparison. Note the huge lattice mismatch of $BaFeO_{3-x}$ with that of LAO, and STO, while with KTO, the lattice mismatch is almost 7% less than that of LAO. This can support the notion that with greater substrate mismatch, $BaFeO_{3-x}$ is less crystalline in quality, yet more convertible to a magnetic material. Lastly, it is widely known that to obtain higher quality crystalline films, lattice mismatch should be kept to below 5%, of which the mismatch between $BaFeO_{3-x}$ with LAO and STO are both $\geq$5%.

Magnetization in different directions

In a paper by Taketani *et al,*[20] the authors measured the magnetization in different planar directions for films grown via pulsed laser deposition. They measured the magnetization perpendicular to the plane (100), parallel to the plane (001) and in-plane (110). They concluded that the magnetization in each direction was different and therefore the sample exhibits conventional antiferromagnetic behavior with magnetic spins along the (100) crystal axis.[20]

Here, the magnetic properties of annealed samples of $BaFeO_{3-x}$ on $SrTiO_3$ and $KTaO_3$ single crystal substrates were investigated in the (100) and (001) directions. Shown in Figure 5-9 is the magnetization versus field of samples measured with crystal orientation perpendicular to the field and parallel to the field. Concluded here is that, in these films, there is no observed change in the strength or the coercivity of the magnetization, hence it does not depend on

direction, as the previously mentioned authors suggested.[20] In addition to this, the papers the authors cited[107, 108] were for samples having 3-5 μ_B per Fe, a few orders of magnitude higher than that of the author's samples. Moreover, both of those cited papers showed evidence of helical ordering from neutron diffraction studies, and these sample measurements were limited to room-temperature SQUID magnetometry.

Lastly, recent neutrons diffraction experiments were executed to further confirm that antiferromagnetic ordering is not present in $BaFeO_{3-x}$. Neutron data showed small peaks, with no temperature dependence, possibly structural peaks. However, no strong antiferromagnetic structure peaks were observed, which shows that $BaFeO_{3-x}$ is not antiferromagnetic, but is rather, a large and disordered material, structurally and magnetically.

Artificial Superlattices of $SrTiO_3/BaFeO_3$

To further elucidate on this cracking phenomena, $SrTiO_3/BaFeO_3$ layered structures with periodicities of 500nm (bi-layer), 10nm, and 4nm were synthesized. This experiment was conducted to determine if minimizing the thickness of $BaFeO_3$ would ease the phenomenon of cracking after ex-situ anneal. The artificial superlattices were grown via alternation of a continuous two-target rotation system, using $BaFeO_3$ and $SrTiO_3$ ceramic targets. Shown in Figure 5-10 is a 2θ-ω scan of an attempted [STO_{5nm}/BFO_{5nm}] artificial superlattice that is 500nm thick on $LaAlO_3$ and $SrTiO_3$ substrates. From the defined satellite peaks, the periodicity of these heterostructures is Λ = 10 nm. In the inset is a reciprocal space map of the corresponding superlattice film on $LaAlO_3$. The satellite peaks are well-defined, and interestingly, they cluster around the relative d-spacings where $BaFeO_3$ and $SrTiO_3$ would each be located had they been each synthesized separately onto the substrate.

Figure 5-11 shows x-ray diffraction scans of attempted 4nm periodic artificial superlattices: as-grown, and then post-annealed. The measured periodicity of the as-grown heterostructure was $\Lambda \approx 2.4$nm. After annealing, the periodicities were again calculated from 2θ-ω scans to be $\Lambda \approx 2.7$nm. The periodicities had increased, meaning the overall thickness of the heterostructure increased. In a normal single layer epitaxial $BaFeO_{3-x}$ film, annealing decreases the out-of-plane lattice parameter, while in most cases the in-plane lattice parameter remains the same. So, in a superlattice with periodicity *n*, the individual material thickness layers are *b* and *s* (*b* = $BaFeO_{3-x}$ and *s* = $SrTiO_3$), making $b + s = n$.

Illustrated in Figure 5-12 is a post-deposition schematic of the substrate holder with substrates still adhered, and the "footprint" of the deposition. Note that depending on where the substrates are positioned, that there is a deviance in the accuracy of the attempted periodicity of 4nm artificial superlattices. Note also that substrate size also plays a part in the accuracy of periodicity, because there are most likely gradient differences in the thickness of the layers as one goes from the center of the deposition area out toward the edges.

Moreover, annealed artificial superlattices of all the mentioned periodicities, down to $\Lambda = 4$ nm, exhibit cracking phenomena as shown in Figure 5-13. This presents further evidence that the cracking phenomena of $BaFeO_{3-x}$ does not depend on thickness of $BaFeO_{3-x}$. Even with thin alternating layers of $BaFeO_{3-x}$ and $SrTiO_3$, it is mainly the large change in lattice constant upon annealing that causes cracking of $BaFeO_{3-x}$.

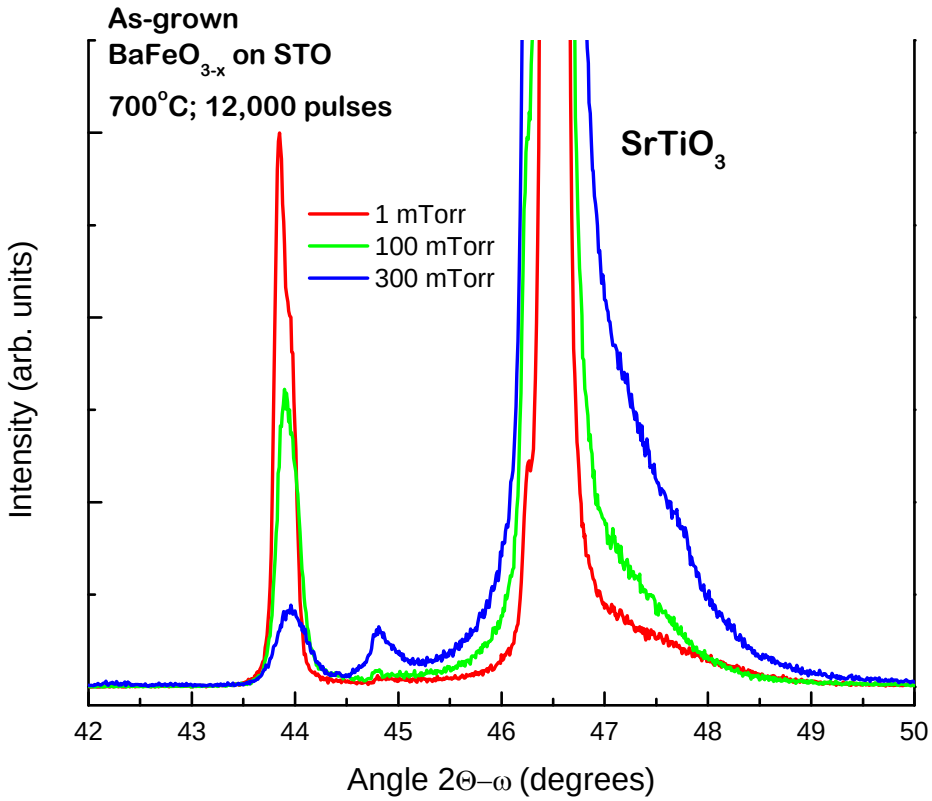

Figure 5-1. Two-Theta-Omega scans of as-grown $BaFeO_{3-x}$ thin films at various pressures.

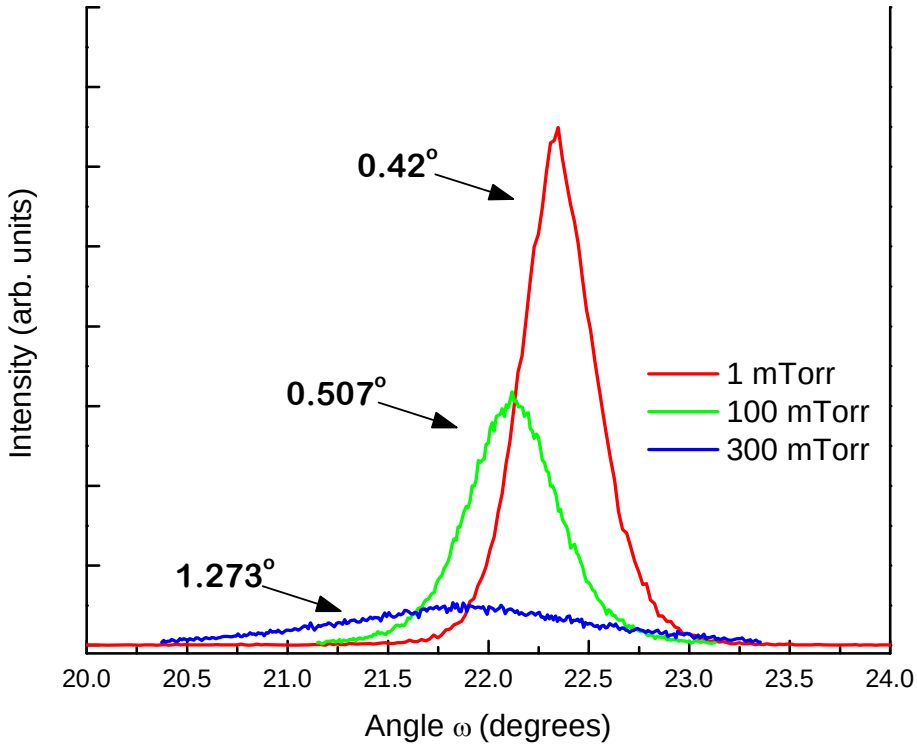

Figure 5-2. Omega Rocking Curves show FWHM of (002) peaks of the films at various pressures.

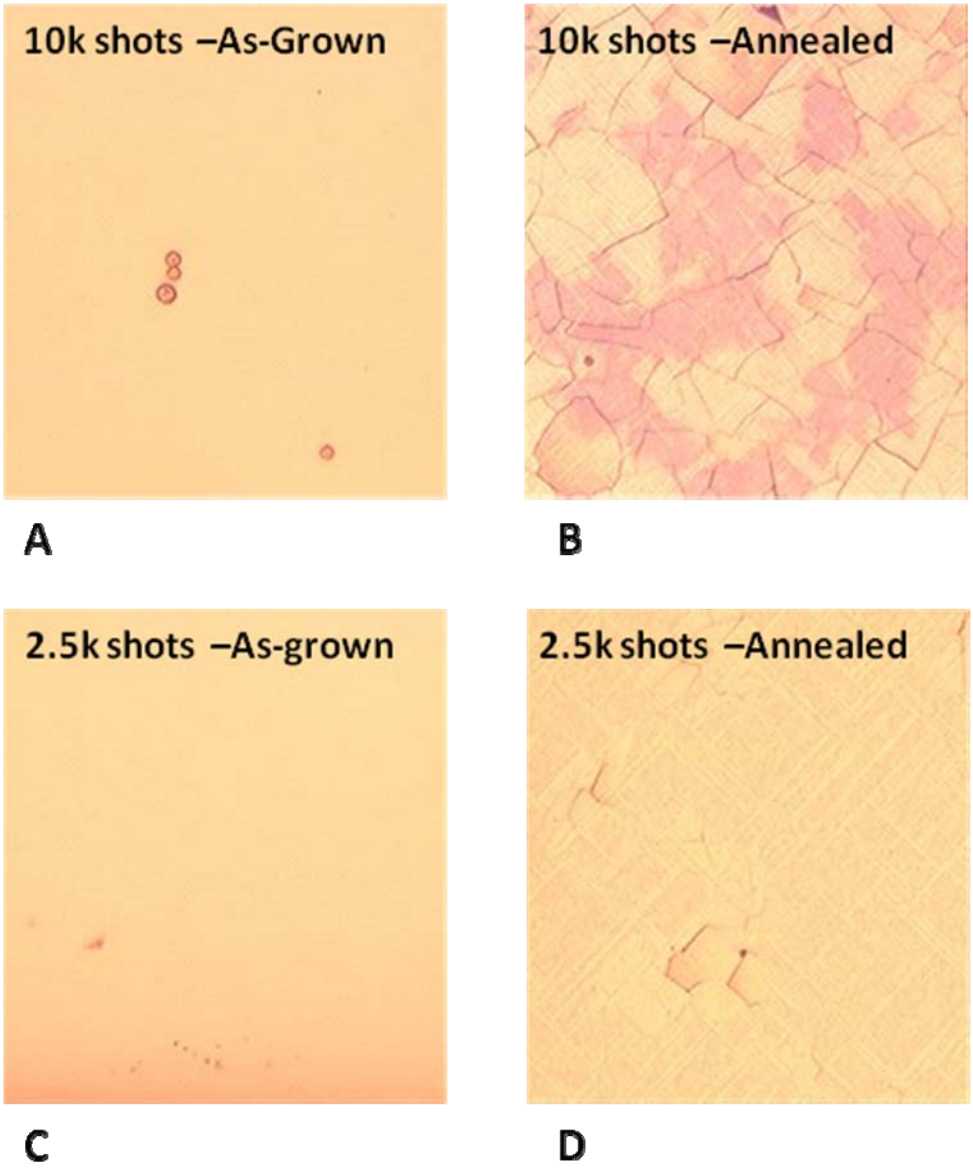

Figure 5-3. Optical Light Microscope images of surfaces of as-deposited and annealed $BaFeO_3$ films. Shown are: A) as-grown film at 1580 nm, B) annealed film at 1580 nm, C) as-grown film at 502 nm, D) annealed film at 502 nm

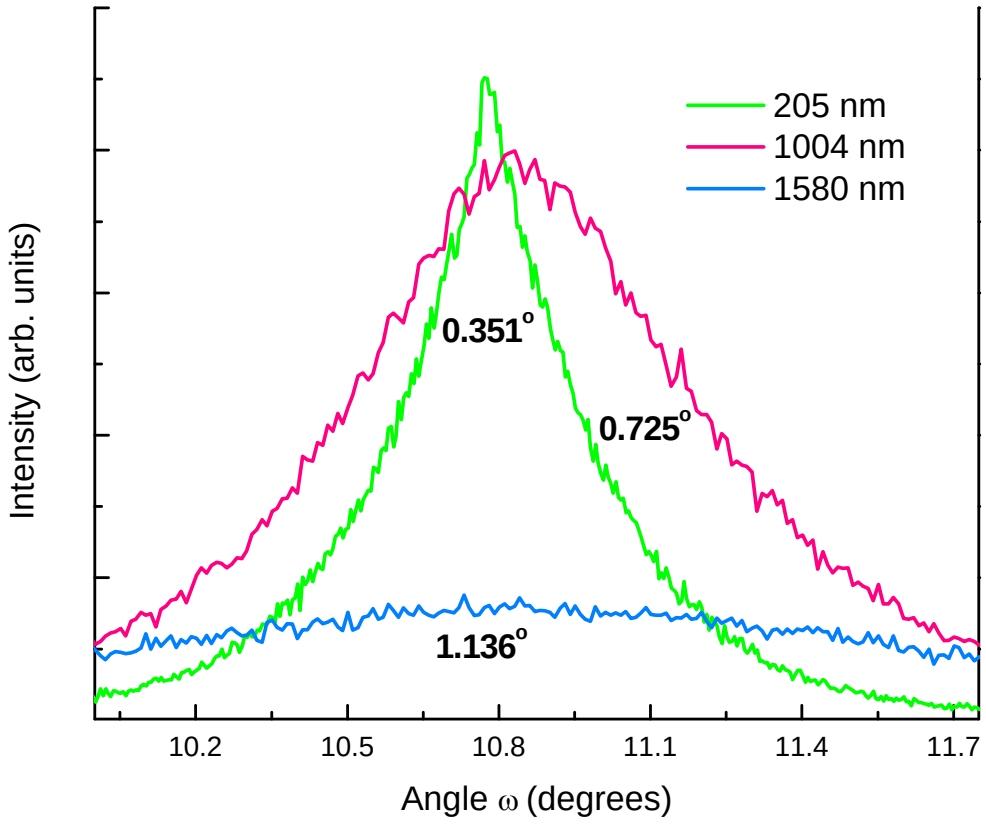

Figure 5-4. Omega Rocking Curves of as-deposited $BaFeO_3$ epitaxial films at different thicknesses.

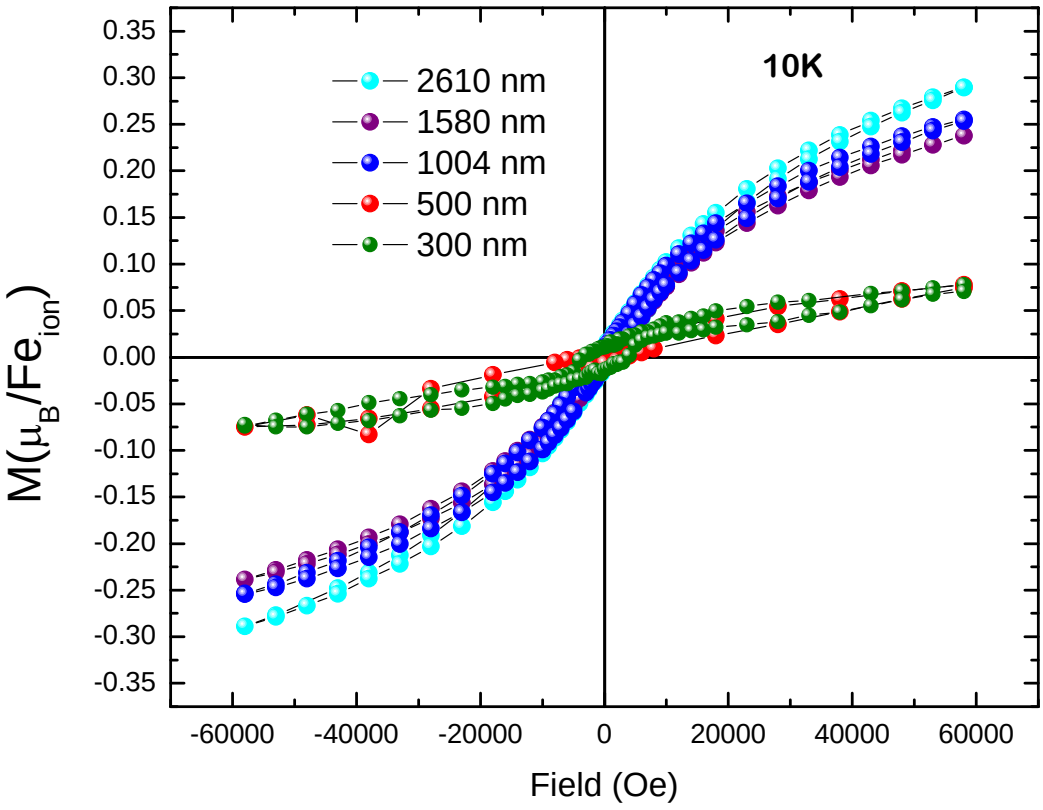

Figure 5-5. Magnetization versus field data of annealed $BaFeO_{3-x}$ epitaxial films at varying thicknesses.

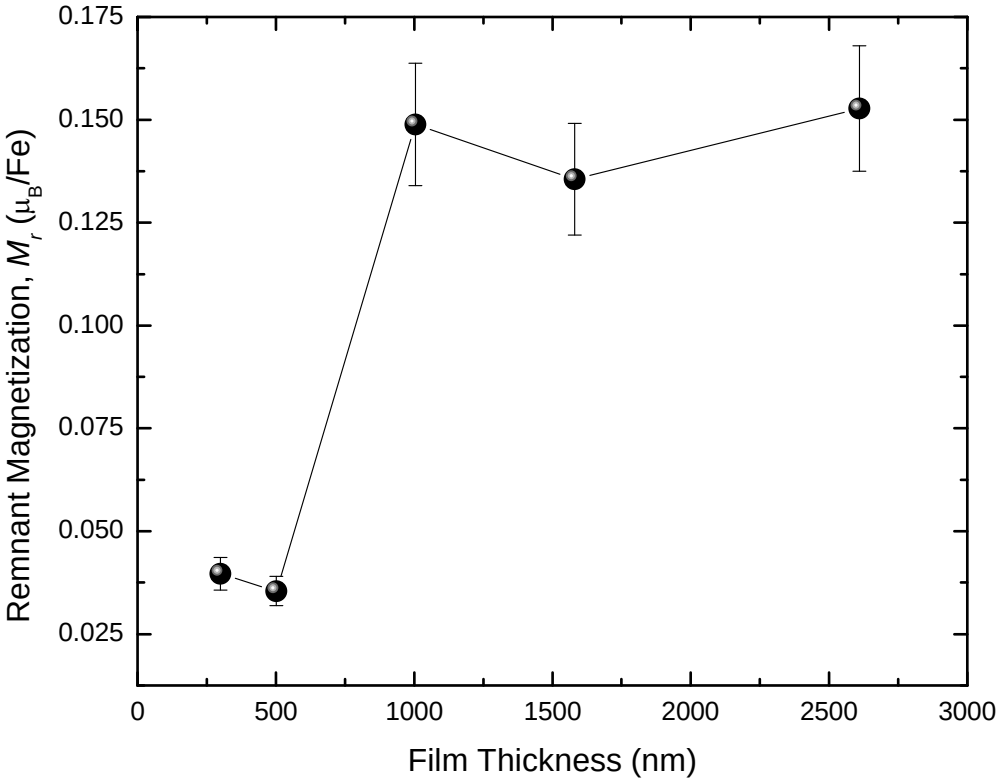

Figure 5-6. Plot of remnant magnetization, M_r versus film thickness (in nm).

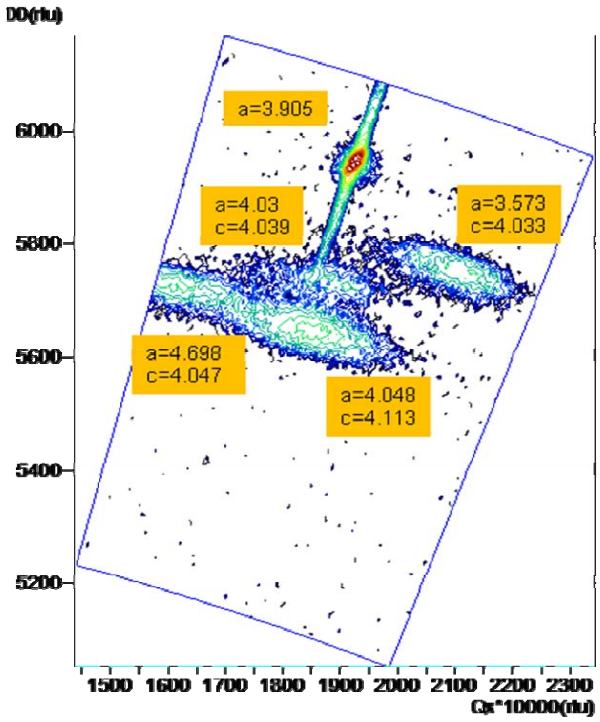

A

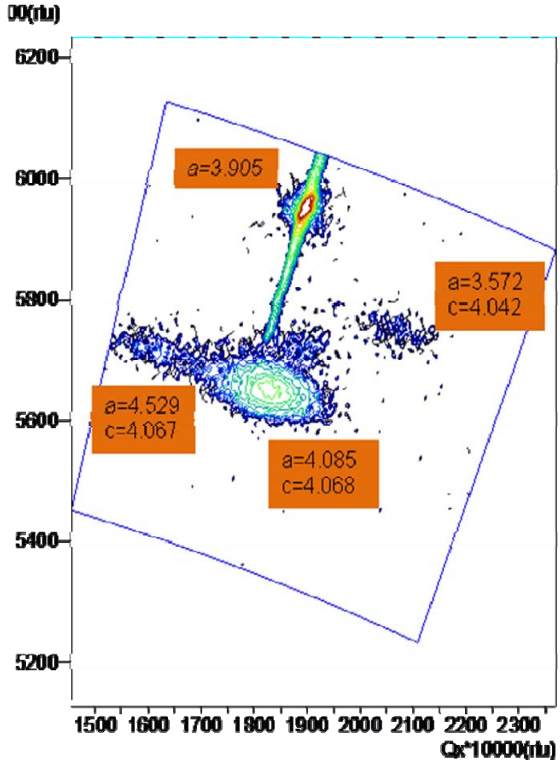

B

Figure 5-7. Reciprocal Space Maps of a) $BaFeO_{3-x}$ on STO at 100mTorr Po_2, and b) $BaFeO_{3-x}$ on STO at 100mTorr P_{N2O}

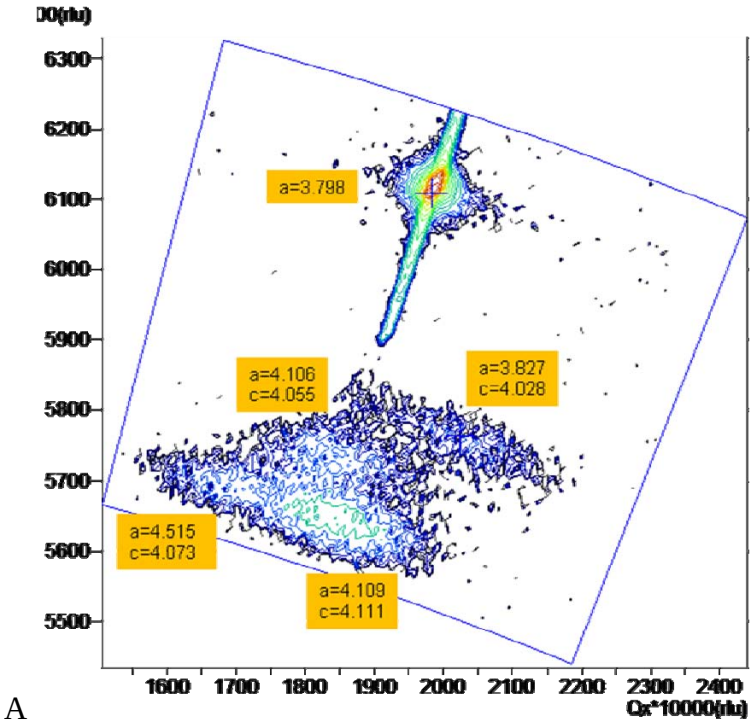

A

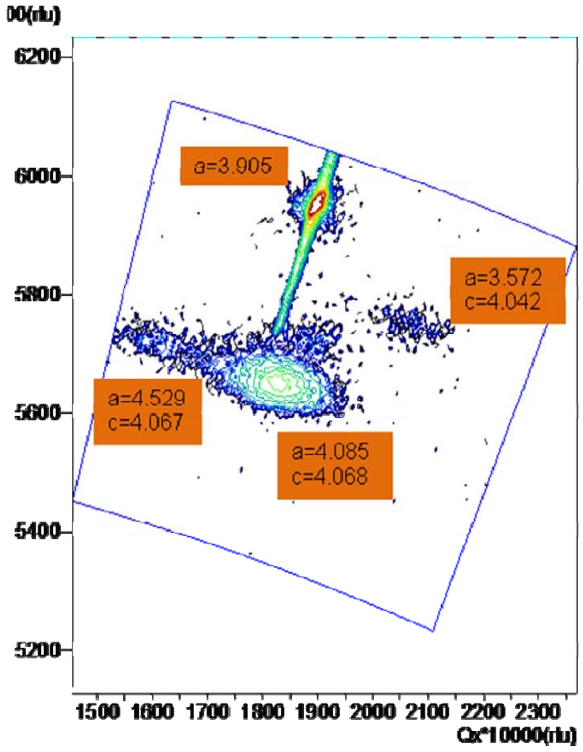

B

Figure 5-8. As-deposited $BaFeO_{3-x}$ at 100mTorr P_{N2O} namely on a) LAO, b) STO, and c) KTO

C

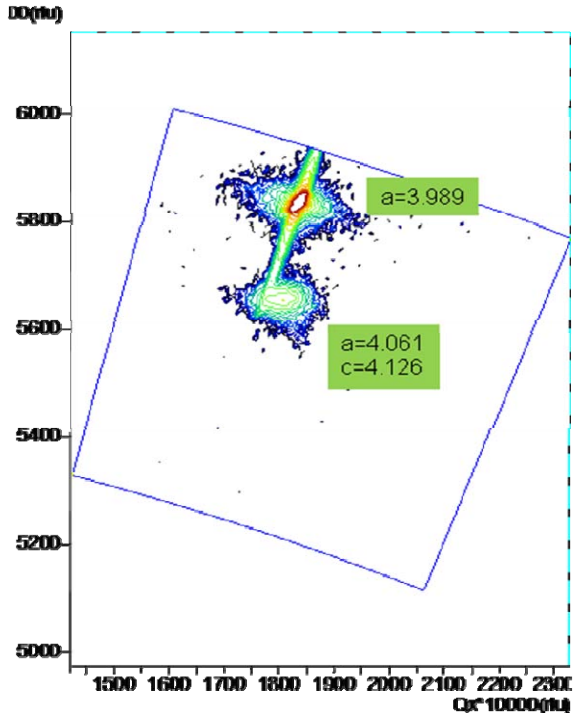

Figure 5-8. Continued

Table 5-1. Comparison of lattice constant mismatch with the two phases of $BaFeO_{3-x}$

Substrate/Buffer Film	$BaFeO_{3-x}$ % Mismatch (O_2 Def: a= 4.1 Å)	$BaFeO_{3-x}$ % Mismatch (O_2 Rich: a = 4.012 Å)
$LaAlO_3$ (3.789 Å)	8.2%	5.89%
$SrTiO_3$ (3.905 Å)	4.99%	2.74%
$DyScO_3$ (3.94 Å)	4.06%	1.83%
$KTaO_3$ (3.989 Å)	2.78%	0.57%
$SmScO_3$ (3.990 Å)	2.76%	0.55%
$BaZrO_3$ (4.186 Å)	2.05%	4.15%

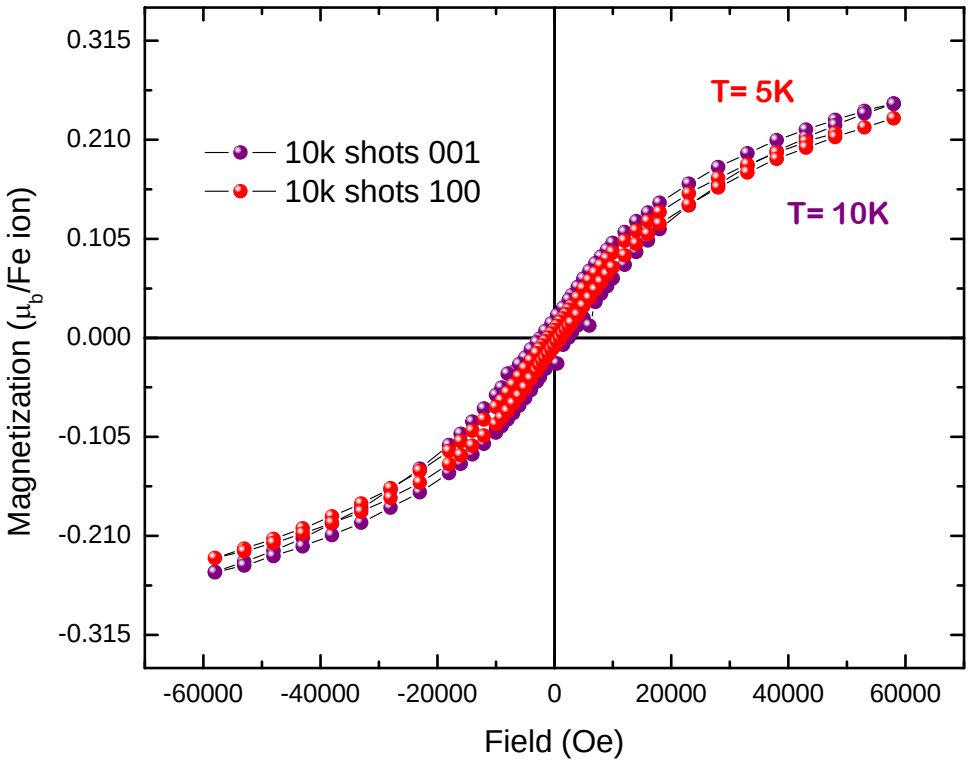

Figure 5-9. Magnetization versus Magnetic field data of $BaFeO_{3-x}$ measured parallel and perpendicular to the crystal axis

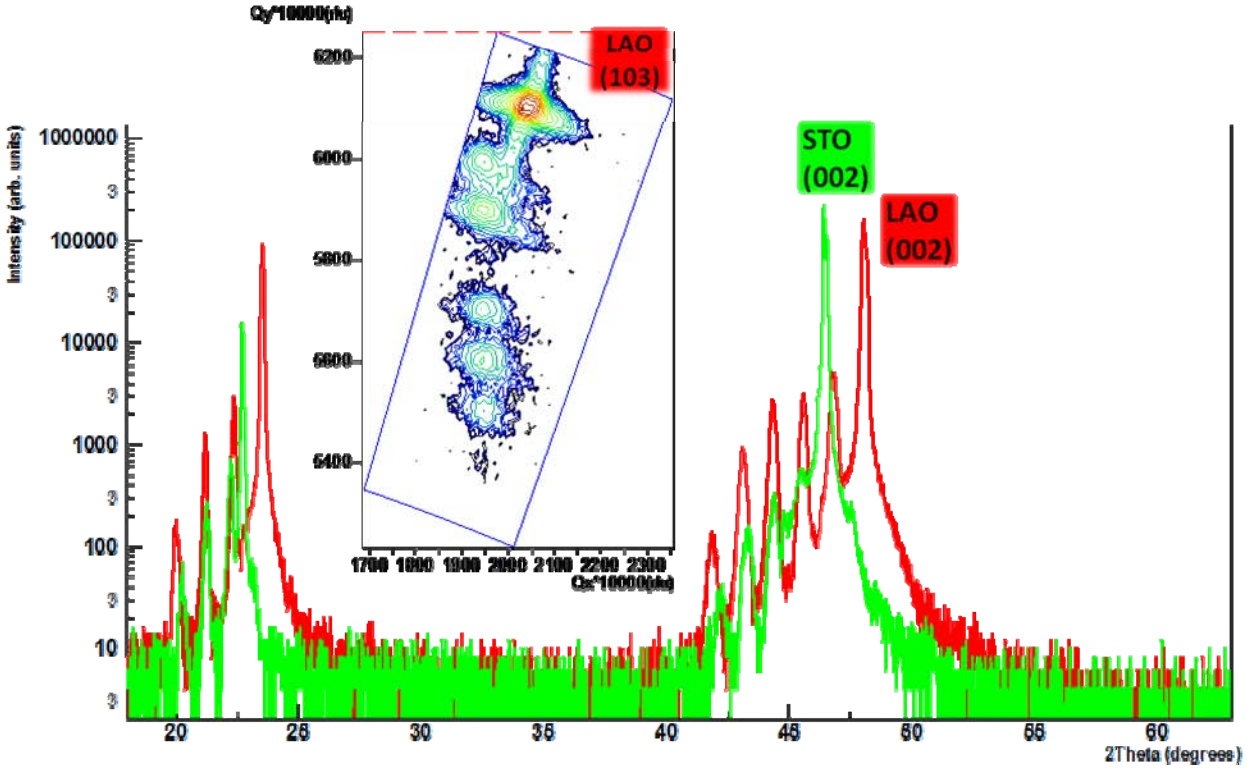

Figure 5-10. X-ray diffraction of [$SrTiO_3$/$BaFeO_3$] artificial superlattices on LAO and STO substrates. Inset is reciprocal space map of superlattice on LAO.

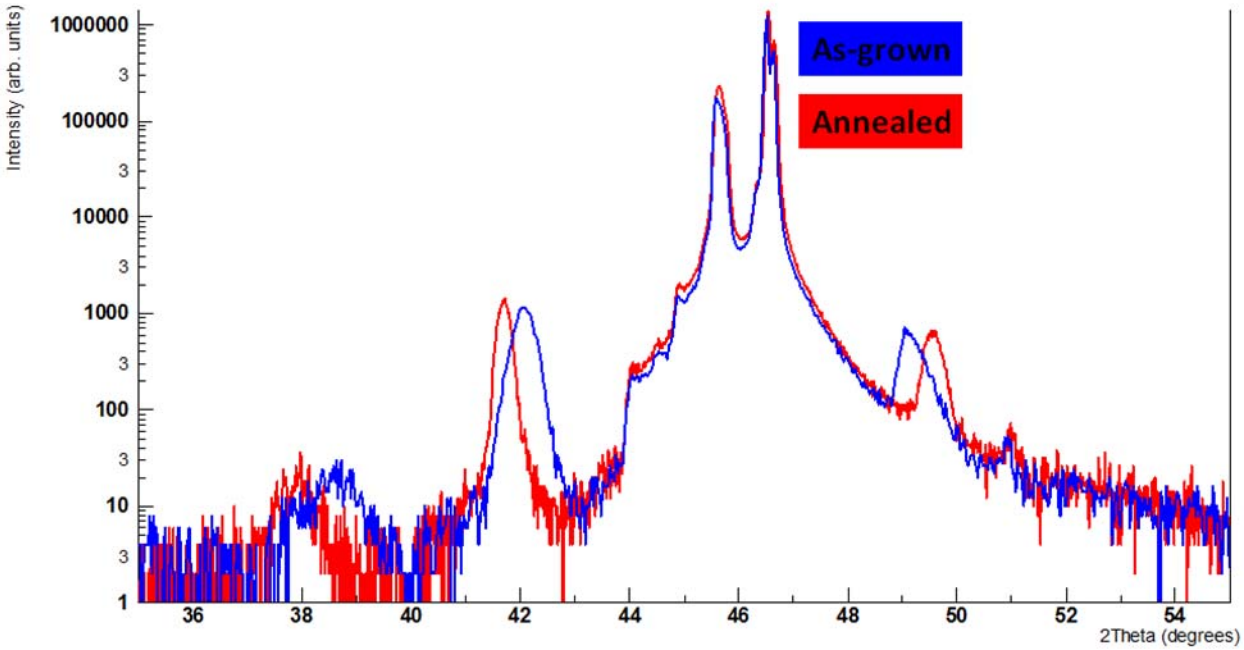

Figure 5-11. X-ray diffraction data of as-grown and annealed [STO/BFO] artificial superlattices. Attempted periodicity is $\Lambda \approx 4$nm.

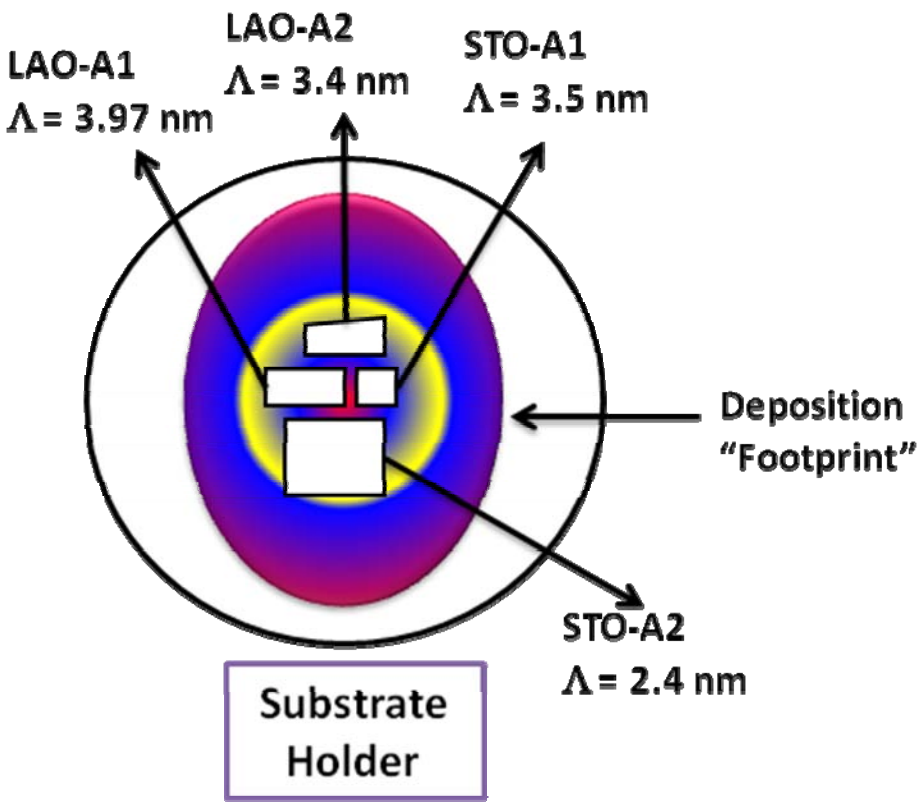

Figure 5-12. Schematic of substrate holder after film deposition with substrates attached. Substrates are labeled with corresponding periodicities (Λ) of the [STO/BFO] superlattice growth.

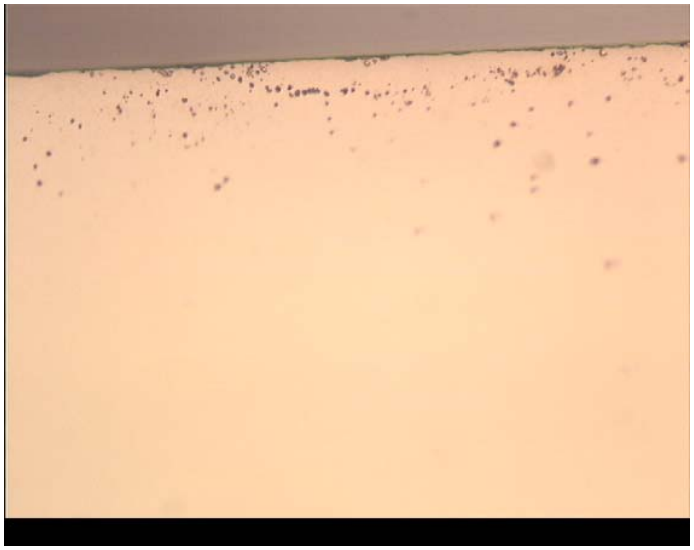

A

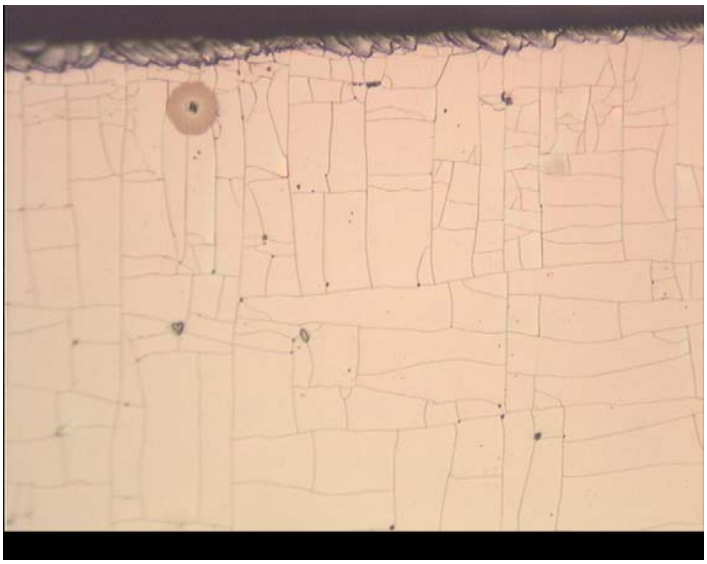

B

Figure 5-13. Optical microscope images of artificial superlattices, namely a) as-grown [STO/BFO] and b) annealed [STO/BFO].

6.0 SYNTHESIS AND PROPERTIES OF (Bi,Ba)FeO_3 SOLID SOLUTION THIN FILMS

As an interesting and widely researched multiferroic, $BiFeO_3$ exhibits a large spontaneous polarization below 1100 K and is antiferromagnetic below 640 K. Its compatibility toward the existence of these two ferroic properties is due to its unique Bi lone pair mechanism, which doesn't interfere with the antiferromagnetically aligned Fe ions. The unique properties of $BiFeO_3$ consistently occur in bulk, and as epitaxial films grown at all thicknesses at optimal conditions.[36, 72] $BiFeO_3$, like most other single phase multiferroics, has a limitation in that it does not have a net magnetic moment—due to its helical magnetic ordering. Research groups have in recent years begun studying the effect of A- and B-site substitution and solid solutions in the $BiFeO_3$ system in an attempt to resolve the issue of zero net magnetization.[32, 53, 75, 109] In particular, their findings show that A-site substitution of diamagnetic large ionic radius ions show promise in providing an increase in magnetization values.[62-64, 67, 70, 71]

Discussed previously in sections 4 and 5 is the study of the magnetic properties of epitaxial films of $BaFeO_{3-x}$,[100] an oxide that exists as a hexagonal structure in bulk, but can be stabilized as a perovskite oxide when grown as an epitaxial film. $BaFeO_{3-x}$ can display ferromagnetic properties depending on growth and annealing conditions.[20, 22, 92, 100] $BaFeO_{3-x}$ shows weakly ferromagnetic behavior and, in addition, the material is highly insulating. Thus $BaFeO_3$, mixed with $BiFeO_3$, may show interesting properties, possibly without compromising its ferroelectric properties. As discussed in Section 2, there are a few groups that have studied the properties of A-site cation substituted $BiFeO_3$, specifically a few alloy compositions of substitution of Ba in $BiFeO_3$. However, all of these studies have been carried out only in bulk sample experiments.[65, 66, 68, 69] Given the magnetic ordering in both $BaFeO_3$ and $BiFeO_3$, this work examines structural properties of the creation of $(Bi_xBa_{1-x})FeO_3$ solid solutions epitaxial films via pulsed laser deposition on single crystal substrates.

There were two ways in which the alloys of (Bi,Ba)FeO_{3-x},were synthesized. In the first method, the growth modes and conditions were found for each of the end members. Because $BiFeO_3$ is a well established multiferroic material which has a strong ferroelectric polarization above room temperature, we elected to start at its optimal growth conditions and tune the growth of $BaFeO_{3-x}$ around the conditions for $BiFeO_3$ growth. The conditions for $BiFeO_3$ are discussed elsewhere.[36] After reaching compatible conditions, the solid solution films were grown by pulsed laser deposition via two-target continuous rotation, previously described in Section 3, on $DyScO_3$ (3.94 Å) , $SrTiO_3$ (3.905 Å), and $LaAlO_3$ (3.789 Å) single crystal substrates.

The second experimental method to synthesize alloys of (Bi,Ba)FeO_{3-x} was via solid-solution targets. Instead of mixing powders of $BaFeO_{3-x}$ and $BiFeO_3$ together, Ba-Fe-O_{3-x} powders were first fabricated by calcination of $BaCO_3$ mixed with Fe_2O_3. Then Bi was added to the powder depending on the alloy desired, and the powder mixture was pressed into a pellet and sintered. Three alloy targets were made: $Bi_{0.1}Ba_{0.9}FeO_{3-x}$, $Bi_{0.5}Ba_{0.5}FeO_{3-x}$, and $Bi_{0.9}Ba_{0.1}FeO_{3-x}$. After completion, the three ceramic targets, each with different compositions, were examined with X-ray diffraction. Figure 6-1 illustrates structural information of the targets, noting that they are acceptable with respect to the reference positions of the end members and $BaFeO_{2.5}$. In addition, the targets' Bi to Ba composition ratios was examined using EDS analysis. Lastly, no buffer layer was used in growing the films of this second method. The only change in growth conditions between the two-target method and the solid-solution target method was a decrease in laser fluence to 1.27 J/cm^2 in the solid-solution target method. The solid solution films were grown by pulsed laser deposition at low laser energy on $LaAlO_3$ (3.789 Å), $NdGaO_3$ (3.85 Å), $(La_{0.29},Sr_{0.71})(Al_{0.65},Ta_{0.35})O_3$ (LSAT) (3.86 Å), and $SrTiO_3$ (3.905 Å) single crystal substrates.

The crystal structure and orientation of the deposited films were examined by X-ray diffraction (XRD). Magnetic characterization was performed on a superconducting quantum interference device (SQUID) magnetometer. Transmission Electron Microscopy (TEM) was performed on some of the samples by collaborating authors.

Results for $(Bi_xBa_{1-x})FeO_{3-x}$ films via continuous alternating target rotation

The midpoint of the solid solution, $Bi_{0.5}Ba_{0.5}FeO_{3-x}$, was created as a starting point. Epitaxial $Bi_{0.5}Ba_{0.5}FeO_{3-x}$ films on $(001)_{pc}$ $DyScO_3$ and $(001)_{pc}$ $LaAlO_3$ were fabricated using the continuous two-target rotation method. The films grown on the pseudo cubic substrates have no extra diffraction peaks other than the (00L) indicating single phase epitaxy. Figure 6-2 shows varied thicknesses of the 50/50 alloy grown on $DyScO_3$ single crystal substrate at a temperature of 700°C and pressure of 50mTorr. There is a shift in d-spacing with increasing thickness. This may indicate that there could be strain occurring in the films at a thickness of 80nm or less.

To mimic the surface and lattice constant of $DyScO_3$, a relatively thick layer (100nm) of $SmScO_3$ on $LaAlO_3$ was grown to serve as the "surface" of the smaller lattice constant substrates. This "buffer" reduces the lattice mismatch between the solid solution alloys and the $LaAlO_3$ substrate. Figure 6-3 shows structural data for the 50/50 alloy composition with varied thicknesses, this time using the $SmScO_3$ buffer on $LaAlO_3$ substrates. At all three thicknesses there are no extra diffraction peaks other than (00L) that show up that would indicate secondary phases. Again, these epitaxial films may be strained at 80 nm due to the similarly comparable lattice parameter of the $SmScO_3$ buffer, but this is can only be quantitatively determined by reciprocal space maps.

Figure 6-4 contains rocking curve measurements on the three films. At all three thicknesses, the rocking curve widths are below 0.3 degrees, indicating high crystalline quality. Although it is not completely evident in the two-theta scan and omega rocking curves, according

to reciprocal space map (RSM) measurements not shown, $Bi_{0.5}Ba_{0.5}FeO_3$ films are strained to the $SmScO_3$ buffer with a- and c-axis parameters of 3.993 Å and 4.063 Å at a thickness of 80nm. At thicknesses of 160nm, the films are relaxed with a- and c-axis lattice parameters of 4.00 Å and 4.07 Å. At 240nm, a- and c-axis parameters are 4.00 Å and 4.06 Å, with virtually no change in lattice constant (between the film grown at 160nm and 240nm). This is evidence of complete relaxation of the film.

Alloys of compositions were successfully fabricated via the two-target rotation method on $LaAlO_3$ substrates with relaxed $SmScO_3$ buffer film. Figure 6-5 shows the x-ray diffraction results for the solid solution films at 0%, 10%, 20%, 30%, 40%, 50%, 60%, 70%, and 80% Bi content. The diffraction results in Figure 6-5 show a continuous shift in d-spacing, with the alloy film peaks moving closer to the $SmScO_3$ buffer (film) peak. All of the alloys showed no extra peaks other than (00L) indicating single phase epitaxy.

Using four-circle X-ray diffraction, reciprocal space maps of the epitaxial films, buffer, and substrate at 20%, 50%, and 70% Bi content are shown in Figure 6-6. The $SmScO_3$ buffer was grown thick enough to be "relaxed" in most cases (more than 80nm in thickness). With increase in Bi content, the film peak begins to line up with that of the $SmScO_3$ buffer, signaling a decrease in a- and c- lattice parameter. A clear difference in Figure 6-6A and Figure 6-6C is seen where the increase in Bi, the smaller cation, has reduced both the a-axis an c-axis lattice constant.

Figure 6-7 shows the in-plane and out-of-plane lattice parameters extracted from the reciprocal space maps. There is a consistent trend in lattice constant until at $x \geq 0.5$, when the solid solution epitaxial films start to become coherent with that of the buffer. After $x > 0.4$, the in-plane lattice parameters hover around that of the $SmScO_3$ lattice parameter while the out-of-

plane (or c-axis) lattice parameters continue to shrink, indicating a shrinking in tetragonality to a more cubic structure. From $x \geq 0$ to $x \leq 0.4$, the a-axis lattice parameter is actually shrinking almost the same amount that the c-axis parameter is shrinking, indicating strong tetragonal behavior in these alloys. This is also shown in Figure 6-8, where the c/a ratios show that the structure varies from highly tetragonal to a basic cubic structure, and a "transition" is observed at $x \geq 0.5$. Note that $BaFeO_3$ is found to be having usually tetragonal structure, while $BiFeO_3$ varies from rhombohedral to slightly tetragonal depending on the film thickness.

$(Bi_xBa_{1-x})FeO_3$ films via solid solution targets

Referring back to Figure 6-1, the ceramic targets were characterized via x-ray diffraction. In the 2-theta scan, structural data of three targets, $Bi_{0.9}Ba_{0.1}FeO_{3-x}$, $Bi_{0.5}Ba_{0.5}FeO_{3-x}$, and $Bi_{0.1}Ba_{0.9}FeO_{3-x}$, are shown. All peaks (except one at 2-theta = 28 degrees), were able to be identified. This was carefully executed by using the JCPDS International tables of structural data for $BaFeO_3$ and $BiFeO_3$ and matching the (*hkl*) with the peak intensities shown on the targets' structural patterns in the two-theta scan. The trend in increasing Bi content and decreasing Ba content is evident via the shift of the peaks in each diffraction pattern. In the insert, this trend is fully illustrated with the labeling of where $BaFeO_{2+x}$, $BaFeO_{3-x}$, and $BiFeO_3$ (111) peak would be, respectively.

Thin films of $Bi_{0.9}Ba_{0.1}FeO_{3-x}$ were successfully synthesized via pulsed laser ablation from a $Bi_{0.9}Ba_{0.1}FeO_3$ solid solution ceramic target. Taking a closer look at the alloy, $Bi_{0.9}Ba_{0.1}FeO_{3-x,}$ was grown on five different substrates in order of increasing lattice parameter: $LaAlO_3$ (3.789 Å), $NdGaO_3$ (3.85 Å), $(La_{0.29},Sr_{0.71})(Al_{0.65},Ta_{0.35})O_3$ (LSAT) (3.86 Å), $SrTiO_3$ (3.905 Å), and $KTaO_3$ (3.99Å). The films are epitaxial, as illustrated in Figure 6-9. There is a large change in d-spacing depending on the substrate the film was grown on. In Table 6-1 is the measured c-axis d-spacings of the film and substrate peaks, taken from the two-theta scan. It clearly shows the

extreme change c-axis d-spacing with choice of substrate. The measured film c-axis parameters of the four films range from 4.6007Å and decrease to 4.161Å, a drastic difference.

Upon closer examination of the two-theta scans, the films on LSAT and on NGO show two peaks, similarly crossing over each other. It appears as a possible transition; it could be structural and/or chemical. Figure 6-10 displays the Omega rocking curves of the thin films. The full-width-half-maximum values are labeled beside each peak. The rocking curves show evidence of the distribution of crystalline domains. Equally important, the rocking curve widths for all four of the epitaxial films fall below 0.22° degrees, indicating highly crystalline films.

The largest rocking curve, which is on LAO at a FWHM of 0.215°, is surprising since there should be a rather large lattice mismatch between $Bi_{0.9}Ba_{0.1}FeO_3$ and the LAO substrate. However, because $Bi_{0.9}Ba_{0.1}FeO_3$ was first synthesized in this work, no prior structural data exists on it, so it is impossible to know beforehand its actual c-axis lattice parameter. A speculation of the potential mismatch between LAO and $Bi_{0.9}Ba_{0.1}FeO_3$ can be estimated from one of its parent compounds, $BiFeO_3$. $BiFeO_3$'s c-axis parameter (relaxed) is approximately 3.962Å. So taking this value, and doing calculations, the lattice mismatch with LAO substrate is about 4.4%, which is high. Assuming $Bi_{0.9}Ba_{0.1}FeO_3$ will have a larger lattice parameter than $BiFeO_3$ due to the presence of large Ba cations, the lattice mismatch will definitely be higher. Also note that the FWHM of $Bi_{0.9}Ba_{0.1}FeO_3$ on STO is not much smaller than that on LAO; its rocking curve width is around 0.1°. This is a tiny difference in FWHM for such a big difference in film-substrate lattice mismatch ($BiFeO_3$'s lattice mismatch with STO is around 1.4%).

With further investigation, the in-plane and out-of-plane lattice parameters of these films along with the corresponding substrates were extracted from reciprocal space maps. From studying the reciprocal space maps in Figure 6-11, all four epitaxial films are entirely strained to

the substrates. This is evidenced by the position of the film (103) peak being directly under the (103) peak of the substrate. This is interesting as these films are approximately 175nm, which is rather thick for complete strain to be present. Also note the increasingly large change in c-axis lattice parameter of the strained films with decreasing substrate lattice parameter.

Table 6-2 demonstrates the complete picture of these excessively strained thick epitaxial films. It is interesting that the unit cell volume of these samples is increasingly larger with decreasing lattice parameter of the substrate (also equal to the in-plane lattice parameter). More importantly, the in-plane lattice parameter only matches that of the substrate's exact lattice value, and this occurs with all of the substrates. Note that there are two values for the films grown on LSAT and NGO due to the presence of dual peaks in both the two-theta scans and reciprocal space maps. Also listed in Table 6-2 is a second *(hkl)* reflection for $Bi_{0.9}Ba_{0.1}FeO_3$ on LAO. The LAO (113) peak shows comparable values to the LAO (103). Furthermore, information for two different samples of $Bi_{0.9}Ba_{0.1}FeO_3$ grown on STO is shown in the table in case of any doubts of reproducibility, because admittedly, these samples prove to be highly unusual in the scope of epitaxial film research.

It should be mentioned that while KTO is labeled on this table, there is no structural data for $Bi_{0.9}Ba_{0.1}FeO_3$ on KTO. When this film was grown on this substrate, the two-theta scans only showed that the KTO substrate peaks were visible, however no film peaks were visible. Two-theta scans measured from 0.2° out to 110° also showed no presence of $Bi_{0.9}Ba_{0.1}FeO_3$ peaks (or any others). This can mean two things. The first is that the film did not grow (or have epitaxy) on KTO. The second is that the film grew, but is completely commensurate with the substrate. This is possible, knowing that the estimated lattice parameter of $Bi_{0.9}Ba_{0.1}FeO_3$ is incredibly close to that of KTO (3.99Å). Reciprocal space maps were done for this sample which did not

show any conclusive evidence that a film peak was there and/or whether it was strained to the substrate. This is the reason for question marks for the KTO sample in Table 6-2.

To have a quantitative perspective of the extreme lattice parameters of these completely strained epitaxial films, Figure 6-12 graphs the backed-out lattice parameters (both a- and c-axis) of the films. For the $Bi_{0.9}Ba_{0.1}FeO_3$ film on KTO, for illustration purposes, this value for the c-axis is estimated and under assumption that the film peak overlaps that of the substrate. In Figure 6-12, there are two trends. Where the trends meet is at the "transition" at $Bi_{0.9}Ba_{0.1}FeO_3$ films on LSAT and NGO. This trend is also shown in Figure 6-13, where the c/a ratios versus substrate values illustrate extreme tetragonality and then reduce down to an almost cubic ratio. Again, for the $Bi_{0.9}Ba_{0.1}FeO_3$ film on KTO, this is estimation. These numbers unusual for a material with the perovskite structure. Transmission Electron Microscopy (TEM) images of two samples (Figures 6-14 and 6-15) illustrate that these are indeed correct values. Figure 6-14 is a TEM image of $Bi_{0.9}Ba_{0.1}FeO_3$ on LSAT where the film is the light colored area and the darker area is the substrate. At the interface, the film is coherent with the substrate, relatively clean, showing that there is no major defect occurring there. In Figure 6-15, the interface of $Bi_{0.9}Ba_{0.1}FeO_3$ with the LAO substrate is also sharp. Looking at the film (lighter area) the film is single phase, and no major defects are shown which supports that the $Bi_{0.9}Ba_{0.1}FeO_3$ epitaxial film on LAO is perovskite.

The magnetic properties of as-grown films are demonstrated in Figure 6-16. The magnetization versus magnetic field data show weak ferromagnetic hysteresis in Bohr Magnetons per Fe for consistency. The remnant magnetization M_r of all of the samples is $0.2\mu_B$ per Fe. This magnetic data is comparable to that of other groups whom measured magnetizations of Ba-doped bulk $BiFeO_3$ samples[65, 68] The coercivity, or resistance of the sample to

demagnetization, is about 6000 Oe on LAO, 8000 Oe on STO, and about 1 Tesla on LSAT, with a magnetic moment for all three, comparable to annealed $BaFeO_{3-x}$ and obviously greater than that of $BiFeO_3$ epitaxial films.[36]

It is important to note is that having comparable magnetic moment after adding only 10% Ba to pure $BiFeO_3$ is surprising and interesting. Theoretically, highly oxidized $BaFeO_{3-x}$ is calculated to have magnetic moments of a lot more than at $0.2\mu_B$. Those films are of low crystalline quality, and it makes sense that they also have low magnetic moment. Moreover, the $Bi_{0.9}Ba_{0.1}FeO_3$ epitaxial films are highly crystalline, and so it is less likely they are magnetically disordered as well.

The apparent "pinching" at 1 Tesla and -1 Tesla is interesting. The "pinch" of the hysteresis loops is at the same magnetic fields in all of the samples. $BiFeO_3$ is known to possess G-type antiferromagnetic helical structuring which is complex.[33] In previous works other groups claim that with substitution of certain A-site cations into $BiFeO_3$ and upon measuring small magnetic moments and obtaining very weak magnetic hysteresis, they are, in effect, breaking down the spiral structure that is responsible for the antiferromagnetism present in pure $BiFeO_3$.[32, 36, 53, 63-71, 75, 109] One can speculate that this "pinching" of the magnetic hysteresis loops is directly related to the disruption of helical magnetic ordering via introduction of 10% Ba^{2+} cations into $BiFeO_3$, and could be cited as evidence for such phenomena.[23, 33]

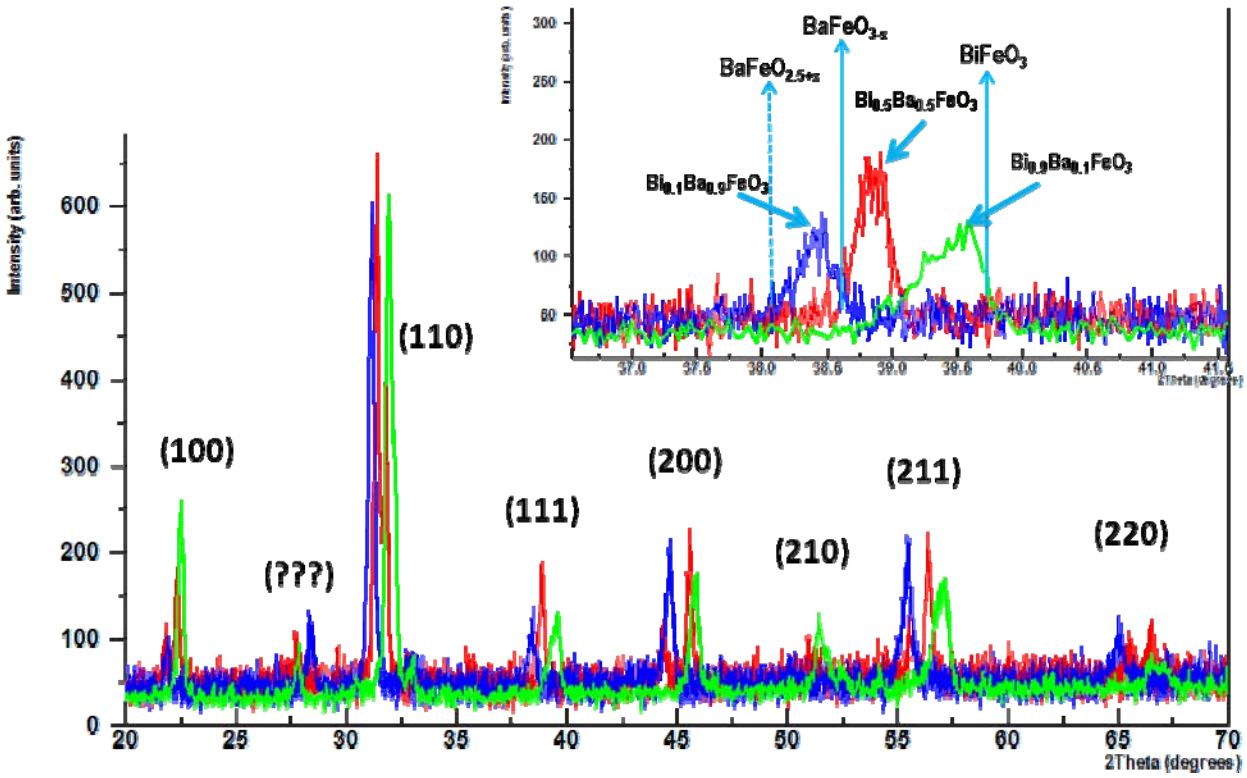

Figure 6-1. Structural data of three $Bi_xBa_{1-x}FeO_3$ ceramic targets. Points of $BiFeO_3$, $BaFeO_{3-x}$, and $BaFeO_{2.5+x}$ are labeled for reference.

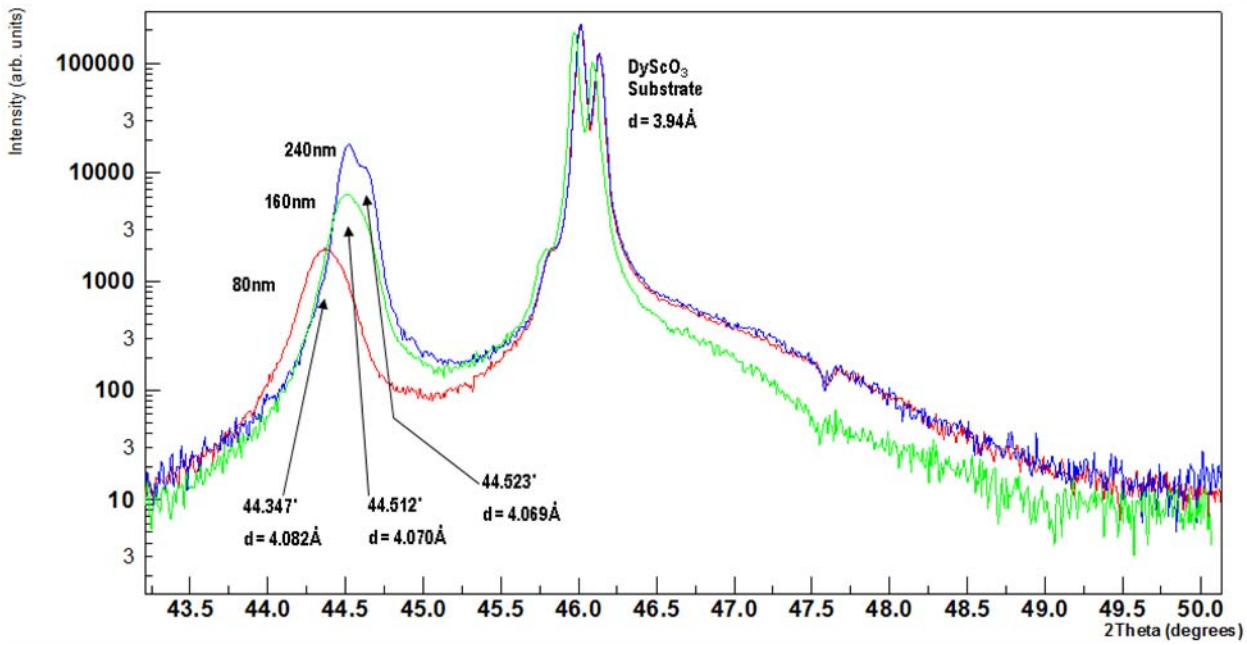

Figure 6-2. X-ray diffraction data for varied thicknesses of $Bi_{0.5}Ba_{0.5}FeO_{3-x}$ on $DyScO_3$ substrates.

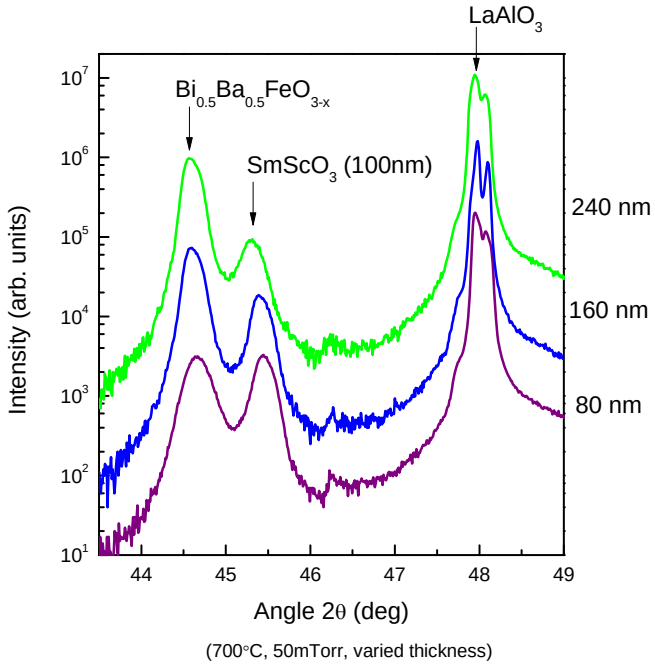

Figure 6-3. X-ray diffraction (2-theta scan) for $Bi_{0.5}Ba_{0.5}FeO_{3-x}$ alloy films at various thicknesses with $SmScO_3$ buffer.

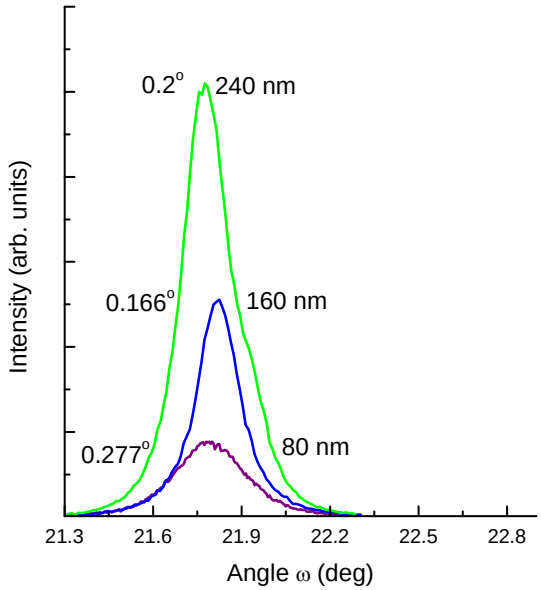

Figure 6-4. X-ray diffraction data for $Bi_{0.5}Ba_{0.5}FeO_{3-x}$ alloy films at various thicknesses. Omega rocking curves of thin films showing strain/relaxation behavior.

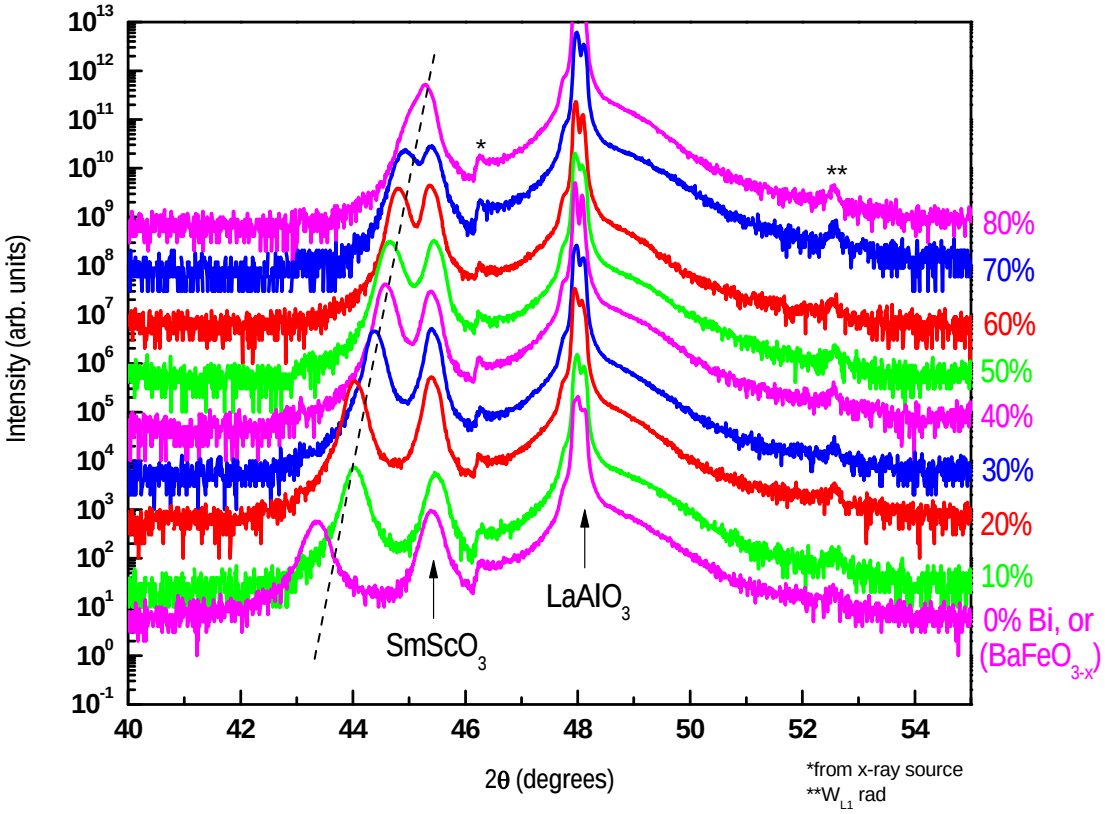

Figure 6-5. X-ray diffraction data for solid solution $(Bi_xBa_{1-x})FeO_3$ grown by pulsed-laser deposition.

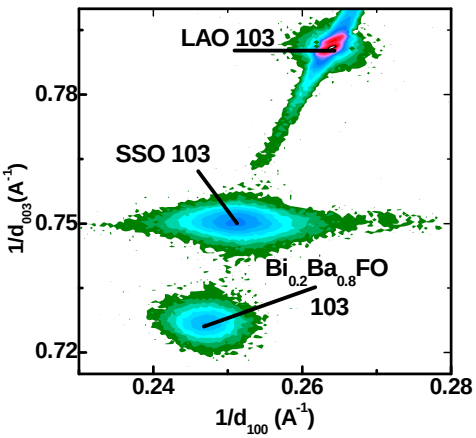

A

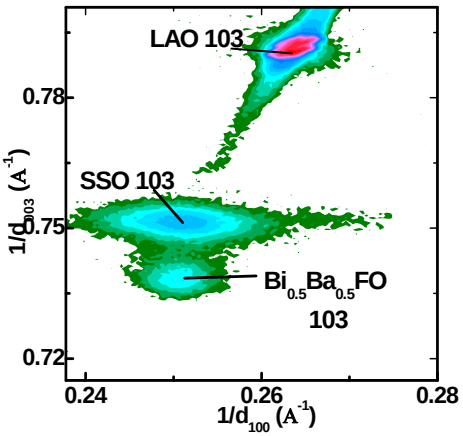

B

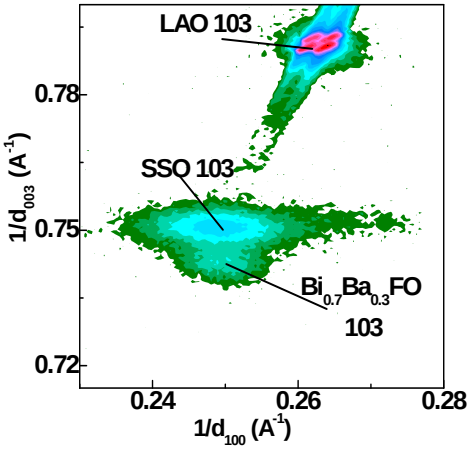

C

Figure 6-6. Reciprocal space maps for selected $(Bi_x Ba_{1-x})FeO_3$ films on $LaAlO_3$ with $SmScO_3$ buffer. A) $(Bi_{0.2} Ba_{0.8})FeO_3$ B) $(Bi_{0.5} Ba_{0.5})FeO_3$ C) $(Bi_{0.7} Ba_{0.3})FeO_3$

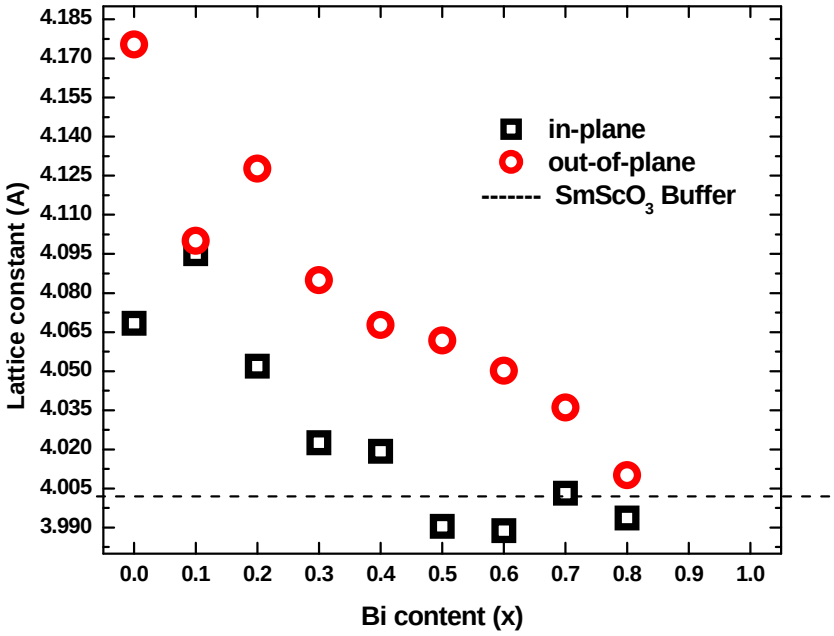

Figure 6-7. In-plane and out-of-plane lattice parameters extracted from the reciprocal space maps.

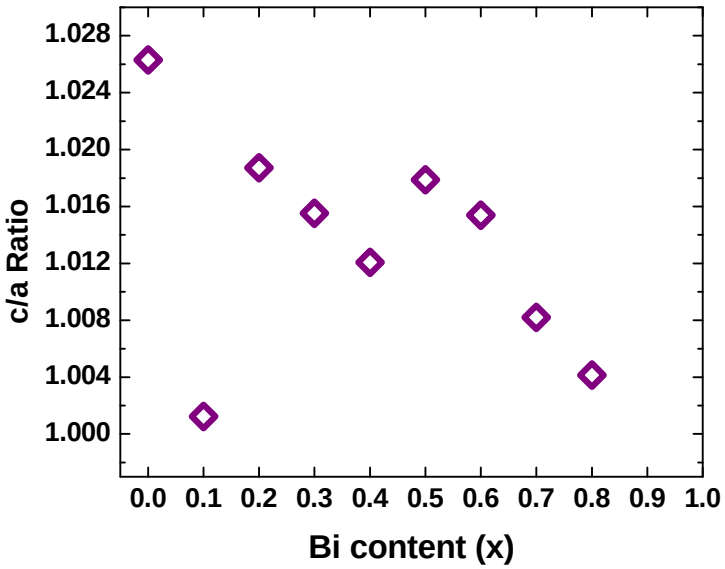

Figure 6-8. C/A ratios calculated from lattice constants extracted from the reciprocal space maps.

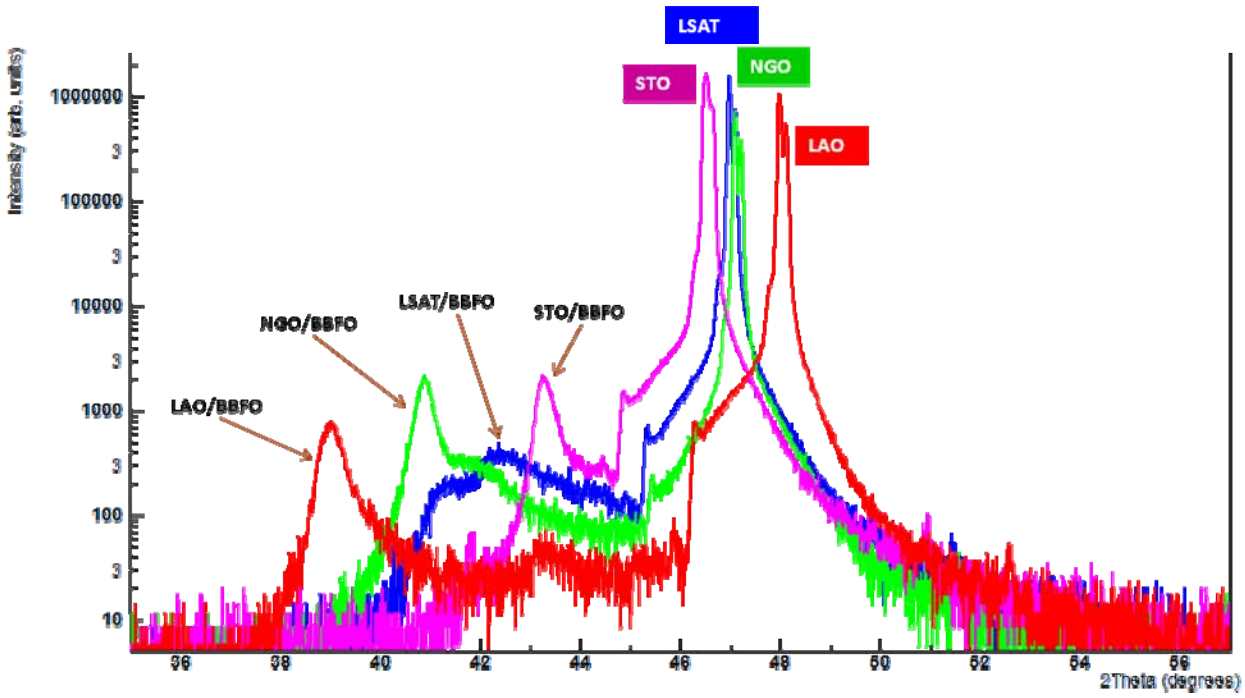

Figure 6-9. $Bi_{0.9}Ba_{0.1}FeO_{3-x}$ epitaxial films grown on four different substrates.

Table 6-1. Measured c-axis d-spacings of substrate and corresponding films, taken from two-theta scan.

Substrate	Substrate (c-axis) measured (Å)	Film (c-axis) measured (Å)
LAO	3.788	4.6007
NGO	~3.86	4.412
LSAT	~3.86	4.245
STO	3.904	4.161
KTO	3.989	3.969(?)

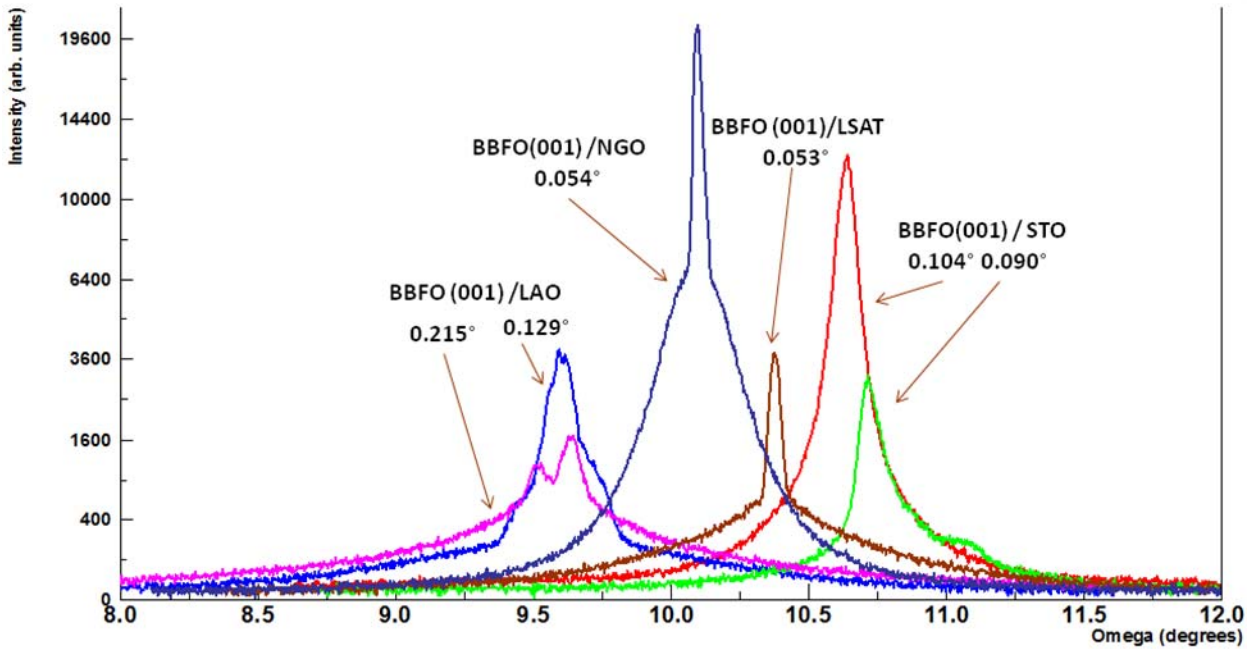

Figure 6-10. Omega rocking curves with measured widths illustrate highly crystalline phases.

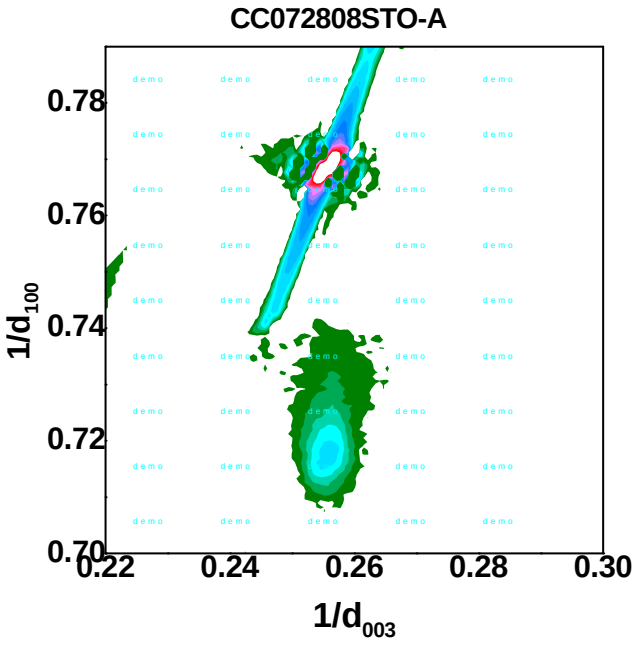

A

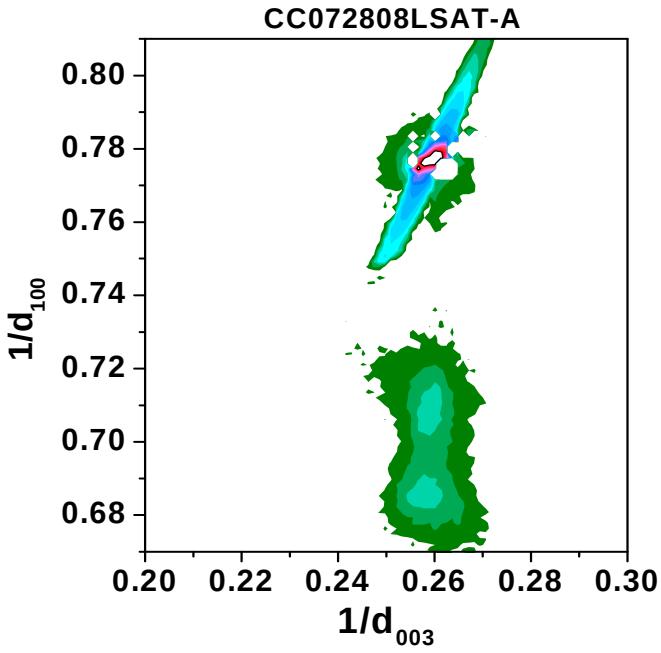

B

Figure 6-11. Reciprocal space maps of $Bi_{0.9}Ba_{0.1}FeO_{3-x}$ epitaxial films grown on four different substrates, namely A) STO, B) LSAT, C) LAO, and D) NGO

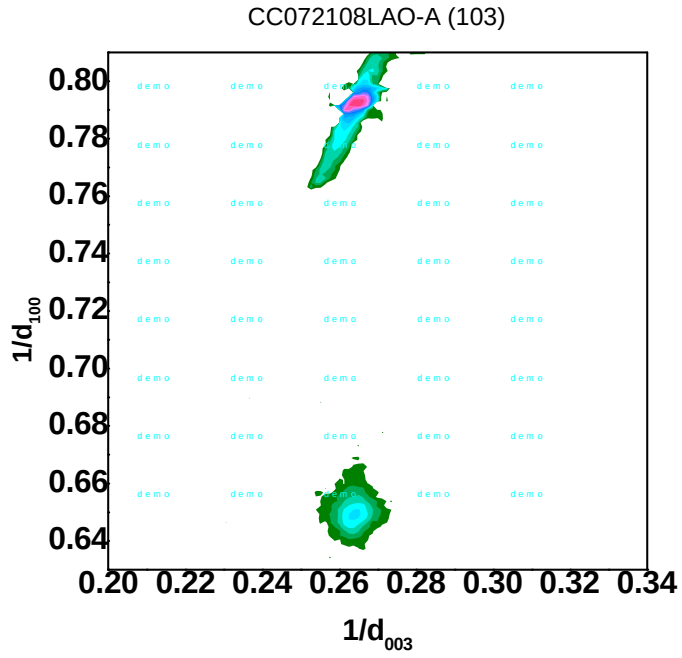

C

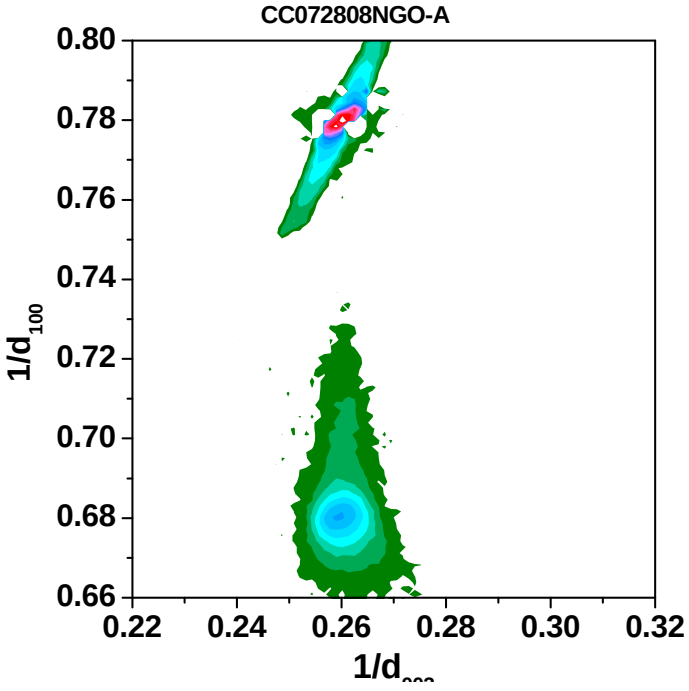

D

Figure 6-11. Continued

Table 6-2. Measured and calculated in-plane and out of plane lattice parameters, and unit cell volumes for selected epitaxial films (calculated from reciprocal space maps or RSMs).

Sample Number & *hkl* Reflection	sub_a	$Film_{a=b}$	$Film_c$	$Cell\ Vol_{film}$	
0721-LAO-103	3.782	3.798	4.620	66.652	
0721-LAO-113	3.792	3.792	4.622	66.45	Not shown
NGO-103-top	~3.85	3.844	4.226	62.4	
NGO-103-bott.		3.844	4.411	65.16	
LSAT-103-top	~3.86	3.861	4.240	63.202	
LSAT-103-bott.		3.861	4.377	65.260	
0721-STO-103	~3.903	3.903	4.137	63.023	Not shown
0728-STO-103	~3.909	3.909	4.180	63.883	
KTO-103	3.989	4.010(?)	3.969(?)	63.821(?)	Not shown

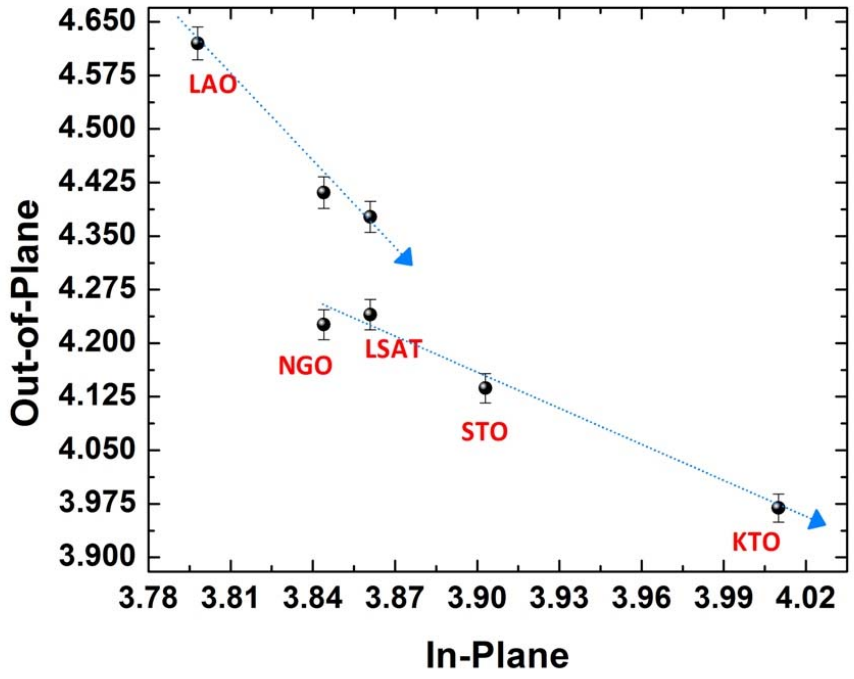

Figure 6-12. C-axis versus a-axis lattice parameters of $Bi_{0.9}Ba_{0.1}FeO_3$ strained films.

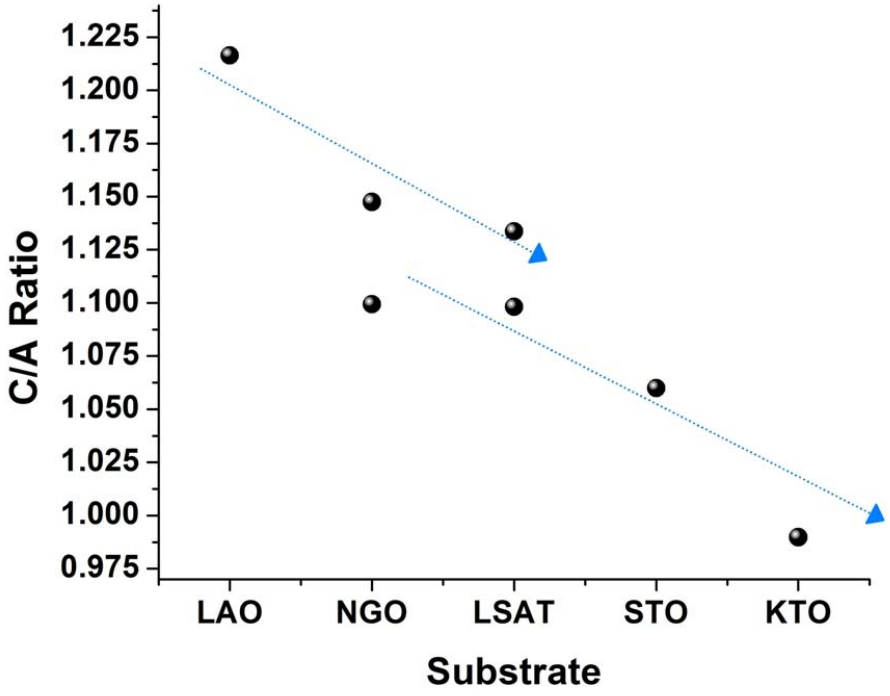

Figure 6-13. C/A ratio of $Bi_{0.9}Ba_{0.1}FeO_3$ strained films.

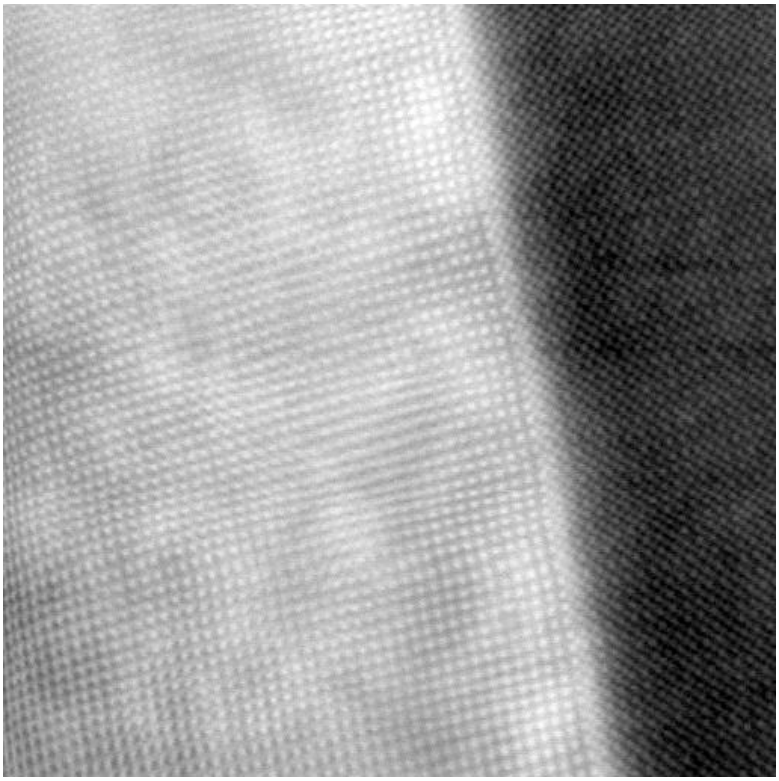

Figure 6-14. TEM image of $Bi_{0.9}Ba_{0.1}FeO_3$ (light area) on LSAT (dark area).

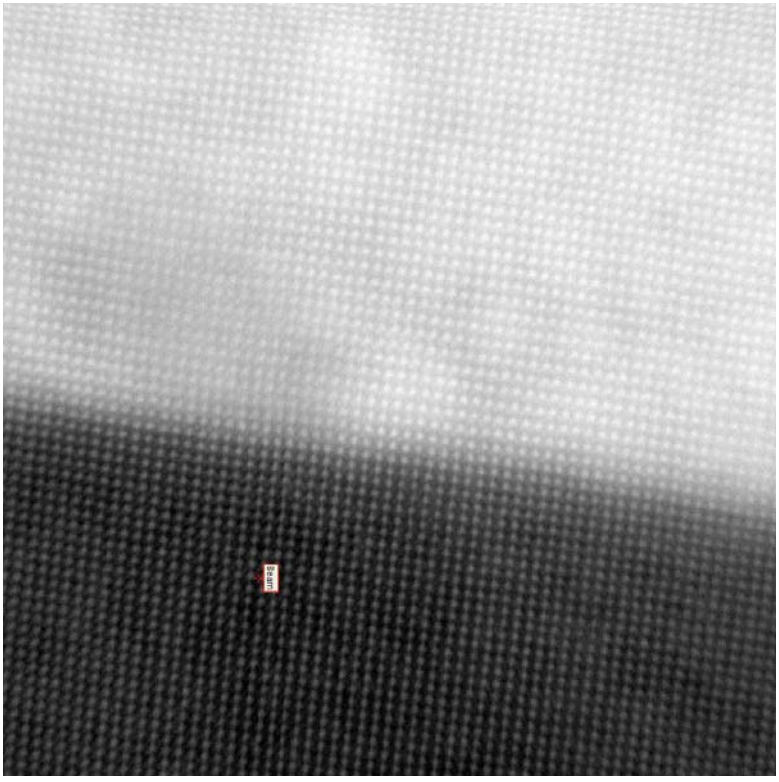

Figure 6-15. TEM image of $Bi_{0.9}Ba_{0.1}FeO_3$ (light area) on LAO (dark area).

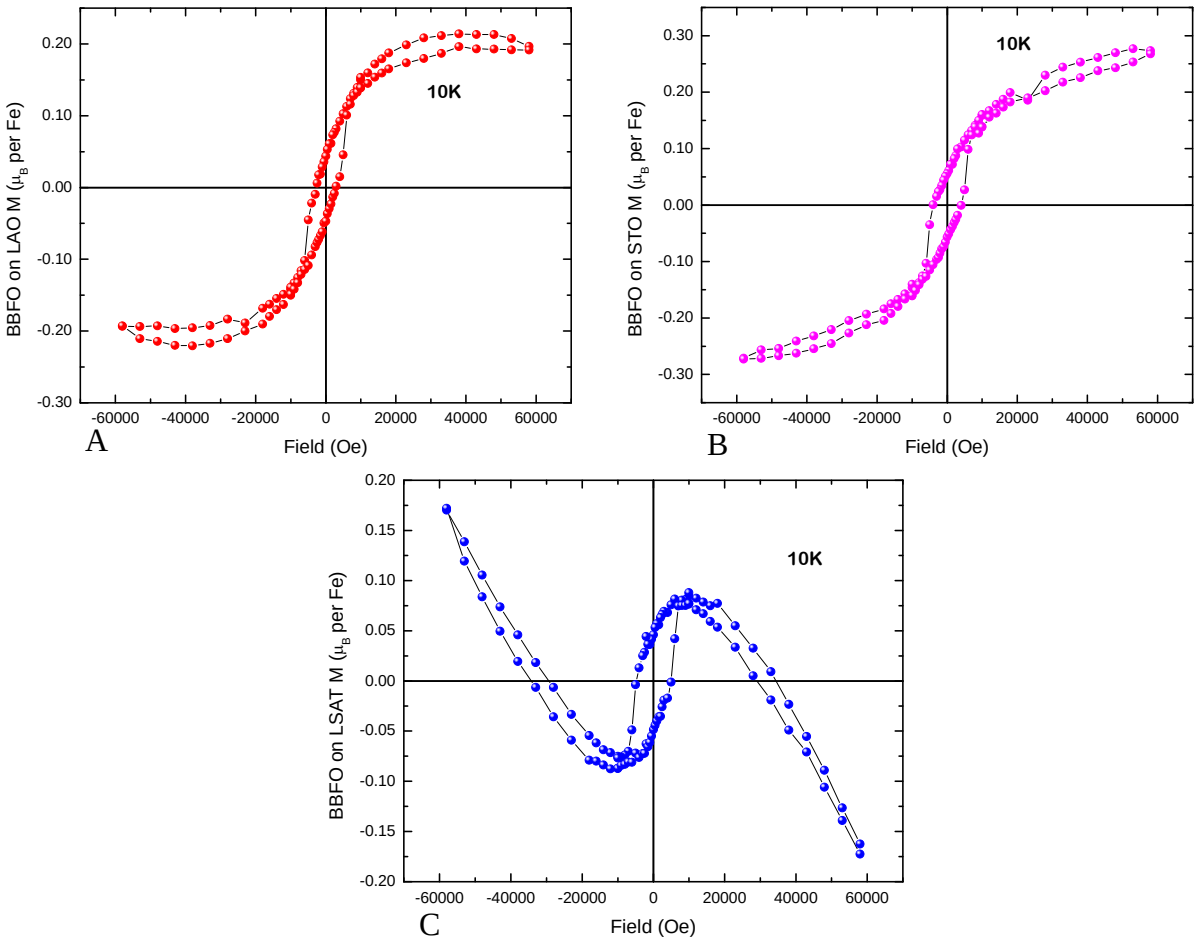

Figure 6-16. Magnetization vs Field data of $Bi_{0.9}Ba_{0.1}FeO_{3-x}$ epitaxial films grown on three out of four different substrates. A) Red loop is film on $LaAlO_3$, B) Magenta loop is film on $SrTiO_3$, and C) Blue loop is film on LSAT.

7.0 **Reflection high energy electron diffraction study of $K(Ta,Nb)O_3$ film growth**

One of the critical aspects of in fabricating superlattices is understanding and controlling the growth of the constituent components. In order to address the growth of $K(Ta,NbO)_3$ (KTN), the study examined KTN epitaxy using reflection high energy electron diffraction (RHEED). The growth was achieved using pulsed laser deposition using a segmented target consisting of 50% KTN, 50% KNO_3. The growth study was performed at 690ºC in 10 mTorr oxygen. The laser repetition rate was 1 Hz. Figure 7-1 shows the RHEED intensity plot as a function of time for KTN deposited on a $SrTiO_3$ (001) substrate. In this plot, the growth starts at t=80 s, indicated by a drop in RHEED intensity. Note that the apparent intensity overshoot spikes are simply the optical emission from the ablation plume. The lower intensity envelop represents the RHEED reflection intensity. First note that the growth yields an initial drop in intensity, followed by apparent oscillations. However, unlike conventional RHEED plots, these oscillations do not correspond to unit cell iterations in growth. Instead, these oscillations reflect a change in growth kinetics in rastering from the KTN target and the KNO_3 (KN) potassium source. In order to better understand this behavior, the rotation of the segmented KTN/KN was frozen on the KN target segment at t=225 s. At this point, the RHEED intensity continuously increases before saturating. At t=295 s, the target is rotated to the KTN segment only. With KTN only, the RHEED intensity drops to near the background noise in the RHEED image, indicating a loss in crystallinity. Reintroducing the KN target ablation plume at t = 325 s yields an increase in the RHEED intensity. These results reflect the fact that stochiometric KTN growth does not occur with ablation from a stoichiometric KTN target. The additional source of potassium is necessary. Second, it appears that the extended exposure of the growth surface to KN flux reaches a steady state with the apparent formation of impurity phases. One may be able to

calibrate the KTN RHEED intensity drop with KTN target ablation such that the (Nb,Ta) flux necessary for a unit cell can be easily controlled. Figure 7-2 shows an experiment where the stability of the K-deficient surface was examined. At t = 100s, the laser was blocked on the down-slope of the target-induced oscillation, terminating with KTN target ablation. The RHEED intensity is stable between without flux, indicating that the KTN film surface is stable and does not decompose or lose K if held at high temperature without additional KN flux.

In order to observe RHEED oscillations due to KTN layer by layer growth, the growth rate was decreased such that multiple iterations between the KTN and KN targets occurs between unit cell growths. Figure 7-3 shows RHEED oscillations due to layer-by-layer growth of KTN for 10 completed cells.

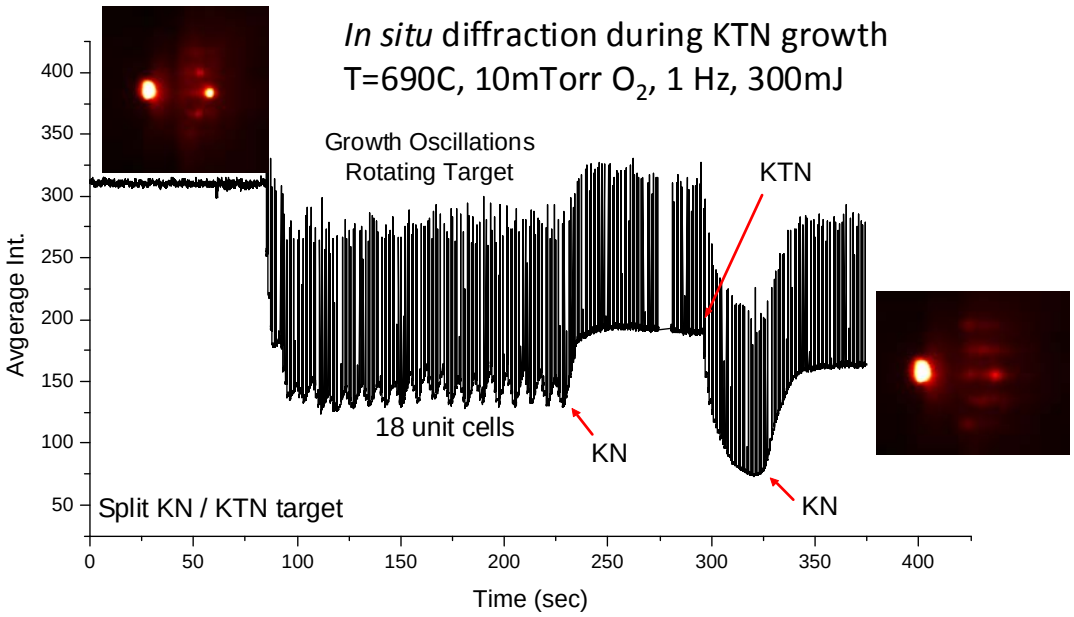

Figure 7-1 shows the RHEED intensity plot as a function of time for KTN deposited on a $SrTiO_3$ (001) substrate

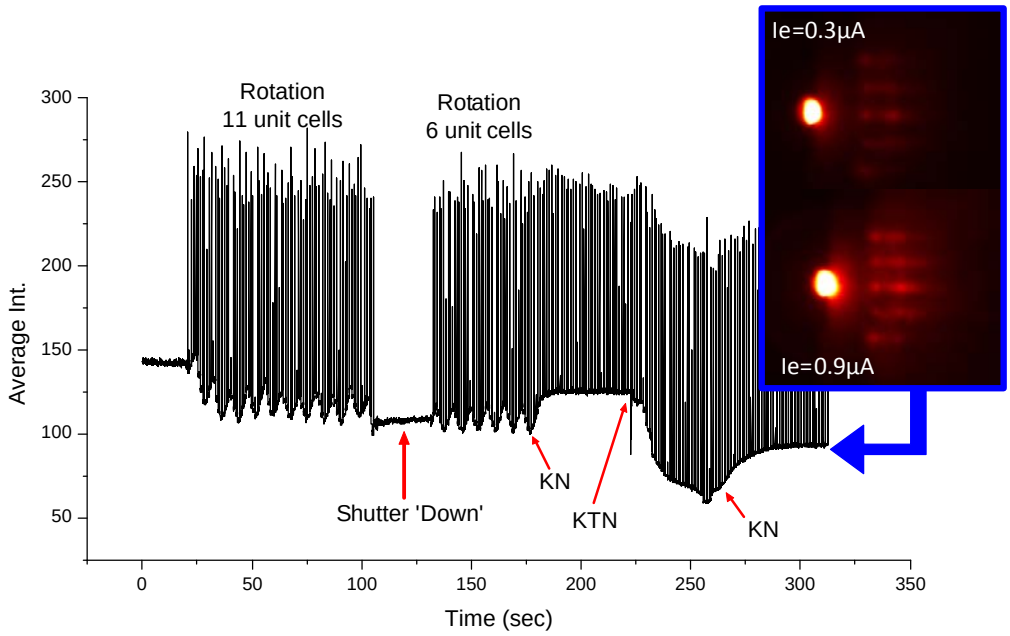

Figure 7-2 Target-induced RHEED oscillations where the stability of the K-deficient surface was examined

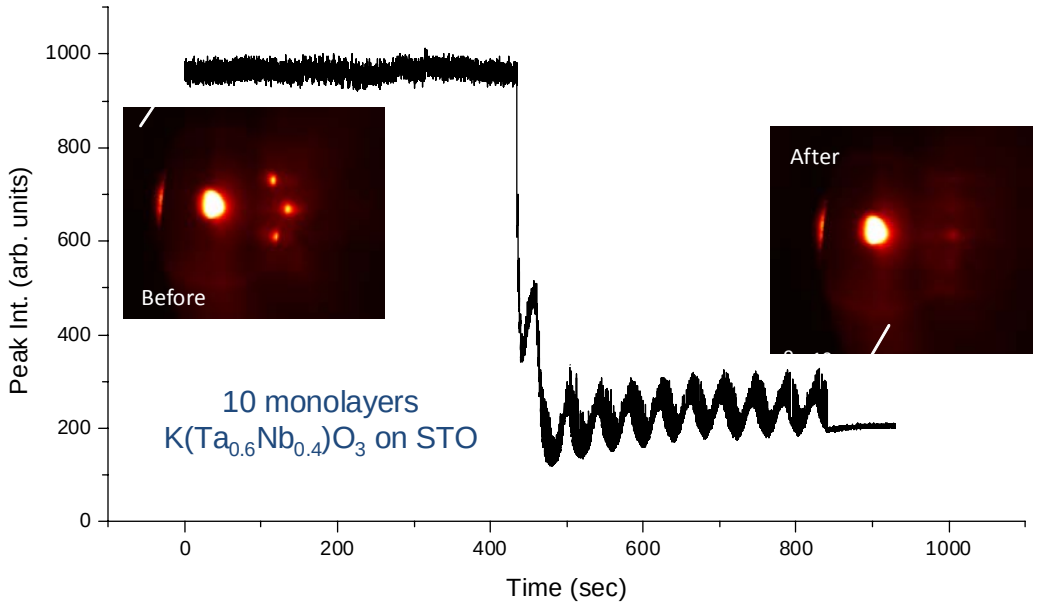

Figure 7-3 RHEED oscillations due to layer-by-layer growth of KTN

8. Structural, magnetic, and electronic properties of $ZnCo_2O_4$ thin films grown via pulsed laser deposition

$ZnCo_2O_4$ is another interesting candidate material for thin film electronics and spin-based electronic device concepts. It exhibits the spinel crystal structure, with generalized chemical formula $A^{+2}(B^{+3})_2O_4$, and has been reported to be both n-type and p-type. It is transparent and has been shown to exhibit ferromagnetism under specific growth conditions. This makes $ZnCo_2O_4$ a candidate ferromagnetic semiconductor to be considered for spintronic applications. Despite these interesting characteristics, there is little known about the thin-film processing, transport, and magnetic properties. In this reports, the synthesis and properties of $ZnCo_2O_4$ thin films will be discussed.

The $ZnCo_2O_4$ films were grown using Pulsed Laser Deposition (PLD). Stoichiometric $ZnCo_2O_4$ ablation targets were made by mixing ZnO and Co_3O_4 powders, then pressing and sintering at 1000ºC. Substrates used in this study sapphire, silicon, spinel, and MgO. A KrF eximer laser with a wavelength of 248 nm was used for ablation. The laser energy was approximately 180 mJ and the PLD chamber was evacuated to a base pressure less than 1×10^{-5} torr each growth run. The growth temperature was varied from 25°C to 800°C. The oxygen growth pressure was varied from 10 to 200 mTorr.

After growth, the structure of the films was characterized by X-Ray Diffraction (XRD), using a Philips APD 3720. Atomic Force Microscopy was used to image the surface and measure roughness. A Digital Instruments Dimension 3100 was used for these measurements. The electronic properties of the films were measured with a Lakeshore 7507 Hall Effect-Electronic measurement system. This system was used to measure the electronic properties at applied magnetic fields ranging from -10 to 10 kG. The magnetic properties of $ZnCo_2O_4$ thin films were also measured using a Quantum Design SQUID magnetometer. Optical transmittance

was measured with a Perkin Elmer Spectrometer. Chemical information was also obtained from X-Ray Photoelectron Spectroscopy (XPS) using a Perkin-Elmer UHV XPS/ESCA PHI 5100.

Figure 8-1 shows the x-ray diffraction results for films grown on c-plane sapphire in an oxygen pressure of 10 mTorr at various growth temperatures. The results show that the majority (111) oriented films are obtained at 400°C. Higher growth temperature result in either mixed orientation or the onset of impurity phases, namely ZnO and CoO. At 750°C, the resulting film appears to be only CoO. This is indicative of the high deficiency of zinc, due to the high vapor pressure at this growth temperature. Figure 8-2 shows the X-ray diffraction results for $ZnCo_2O_4$ films grown at 400°C in various oxygen pressures. In this case, the films are most highly oriented at 400°C, with preferred growth in the (111) direction. High Resolution XRD was also conducted for films grown on sapphire at 400°C and pressures of 50 and 150 mTorr. Omega rocking curves examined orientation of the (333) peaks, yielding a full width at half maximum of 0.34-0.39°, indicating good crystallinity.

Figure 8-3 shows the XPS results of the high resolution scan of the Co peak $2p_{3/2}$ and $2p_{1/2}$ locations. Due to the close proximity of the $ZnCo_2O_4$, Co_3O_4, and CoO peak locations, it is very difficult to resolve the state of the cobalt cation. However, the large height of the shoulders of the $2p_{3/2}$ and $2p_{1/2}$ satellite peaks is indicative of Co^{+2} in the films The high resolution scan of the Zn $2p_{3/2}$ and $2p_{1/2}$ locations, indicated that Zn is in the +2 valence state. Electron Dispersive Spectroscopy was used as a final confirmation to check that the Zn:Co ratio was correct. Figure 8-4 shows that there was no observable correlation between Zn:Co ratio and growth pressure in the films grown at 400°C. However, some films were found to be Zn-deficient, consistent with the presence of Co_3O_4 in the films.

Using AFM, the RMS roughness value of a $ZnCo_2O_4$ film grown at 400°C and 150 mTorr was found to be 4.674 nm over a $1\mu m^2$ area, as shown by Figure 8-5. Hall measurements on the thin films grown at 400°C were found to be n-type for oxygen growth pressures of 10 to 100 mTorr and p-type for pressures of 150 to 200 mTorr. In these films, resistivity was found to increase with Oxygen growth pressure, while carrier density was found to decrease with increasing Oxygen growth pressure. The carrier density and resistivity are shown in Figure 8-6. For each sample, resistivity and carrier density were calculated by the average of the measured value at all applied fields. Resistivity was also measured as a function of temperature on a Quantum Design Physical Property Measurement System. The results show that the conductivity has an exponentially decaying $T^{-1/4}$ dependence, as seen in Figure 8-7. This is indicative of a variable-range hopping mechanism regulating the conduction in the films. This is consistent with the past research on $ZnCo_2O_4$ and Co_3O_4.

The optical transmittance was measured for two films grown at 400ºC on sapphire. The results give an estimated bandgap of 2.2-2.4 eV, as shown by graphing the Tauc relation of $(\alpha h\nu)^2$ vs. energy in Figure 8-8, and obtaining the x-intercept of the tangent line. This compares with the previous research on $ZnCo_2O_4$, which gives a bandap of 2.63 eV. A possible second band gap can be deduced from another linear region of the curve at 1.4 eV, which would confirm the presence of Co_3O_4 in the films. The bandgap of CoO has been measured at 2.5 eV.

The n-type film grown at 10 mTorr was found to be strongly ferromagnetic, as a distinct hysteresis loop was present, as shown in Figure 8-9. At higher growth pressures, the films were observed to have a superparamagnetic-like response. The Curie temperature was estimated to be above room temperature due to the lack of pinch off and observable maximum in the zero field-cooled and field-cooled measurements of the magnetization as a function of temperature.

To investigate the source of these magnetic properties, the XPS results were investigated further. The XPS results indicate a lack of Cobalt metal in the films, eliminating it from contributing to the magnetic properties. Co^{+2} is indicated in the XPS data; however, no CoO peaks are observed in the XRD results. This leaves Co_3O_4 as the source of the Co^{+2} cation state. However, as Co_3O_4 is anti-ferromagnetic, we must conclude that the $ZnCo_2O_4$ is the source of the ferromagnetism.

Describing the source of the superparamagnetic-like response is more difficult. It could be possible that an exchange interaction between the $ZnCo_2O_4$ ferromagnetic exchange and the Co_3O_4 antiferromagnetic exchange results in a superparamagnetic-like behavior. It also has been shown that Co_3O_4 nanoparticles can exhibit superparamagnetism. A third possibility is the possible solid solution of $ZnCo_2O_4$-Co_3O_4, which prevents the ferromagnetic direct exchange between the Co atoms in the $ZnCo_2O_4$.

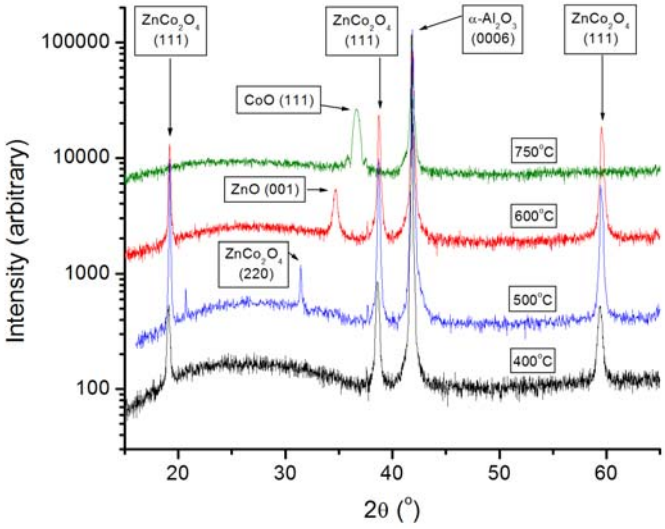

Figure 8-1 X-ray diffraction results of $ZnCo_2O_4$ films grown at multiple temperatures and 100 mTorr

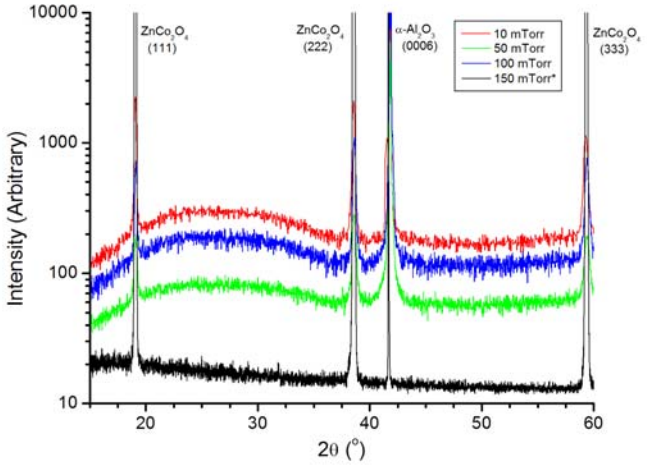

Figure 8-2 X-ray diffraction results of $ZnCo_2O_4$ films grown at 400ºC and various pressures

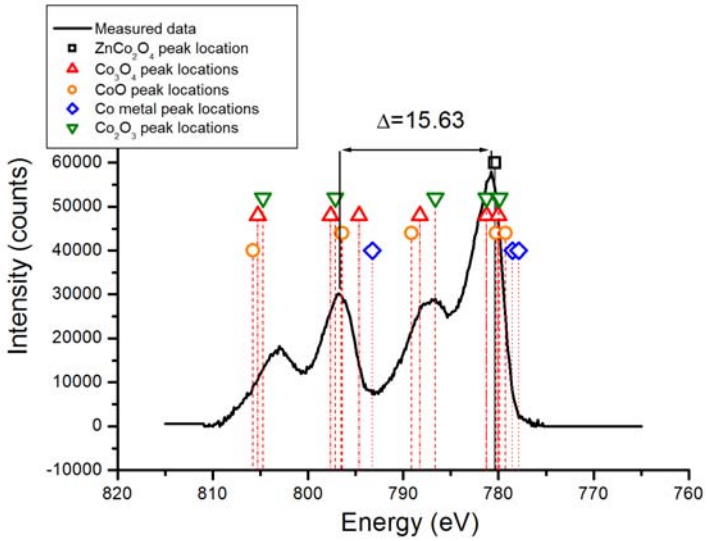

Figure 8-3 X-Ray Photoelectron Spectroscopy results of $ZnCo_2O_4$ film with Co peak locations

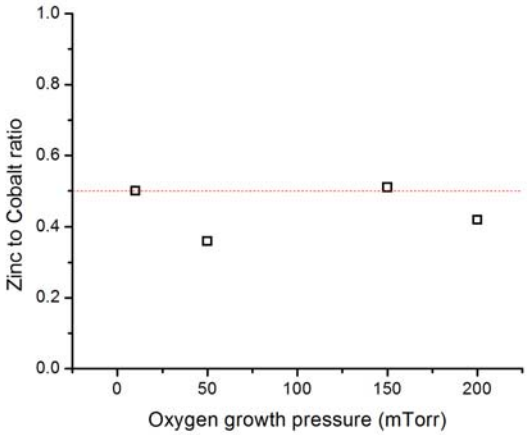

Figure 8-4 Energy Dispersive Spectroscopy results of $ZnCo_2O_4$ films growth at 400ºC and various pressures

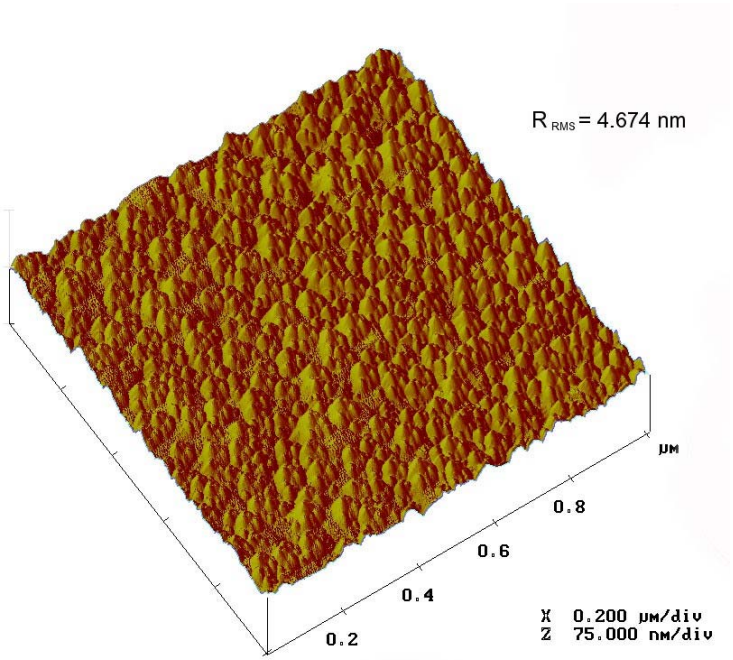

Figure 8-5 Atomic force microscopy image of $ZnCo_2O_4$ film grown at 400ºC, 150 mTorr

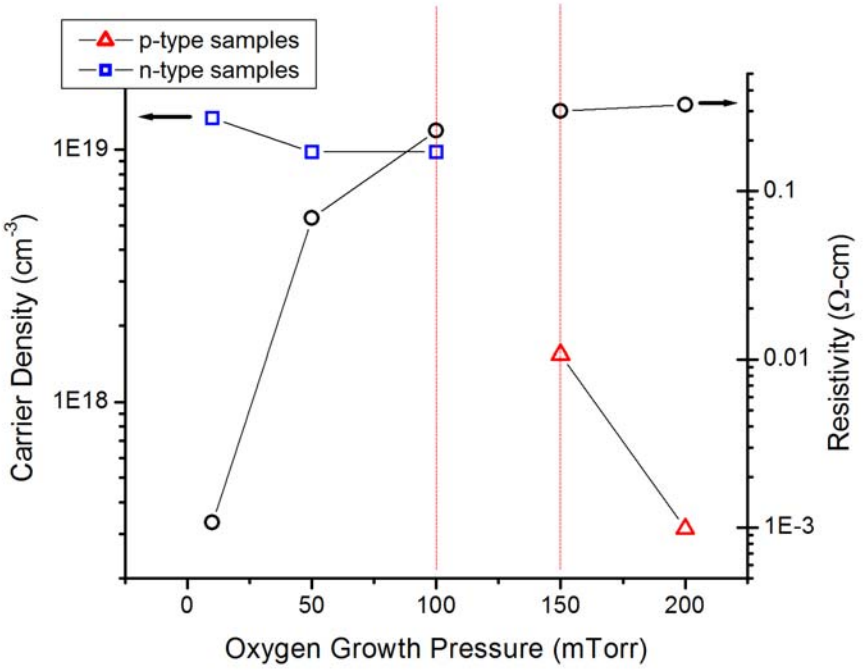

Figure 8-6 Carrier density and resistivity vs. Oxygen growth pressure

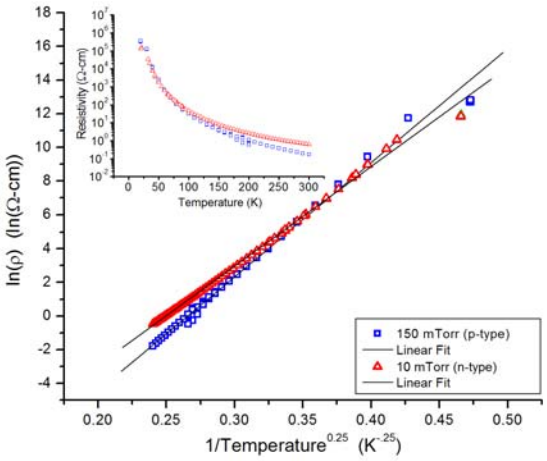

Figure 8-7 Resistivity as a function of temperature

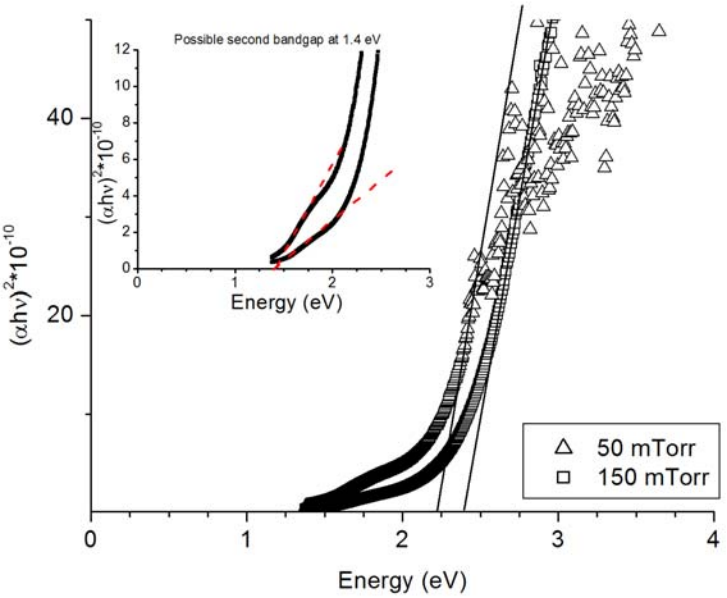

Figure 8-8 Transmittance vs. energy, with inset of $(\alpha h\nu)^2$ vs. E

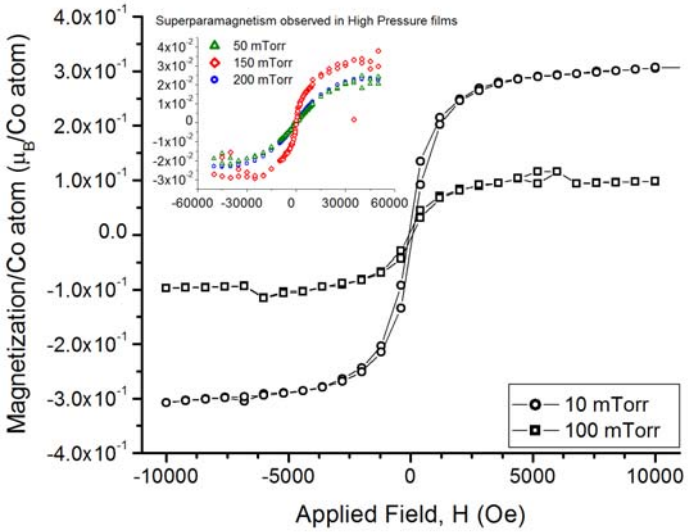

Figure 8-9 Hysteresis curve exhibiting ferromagnetism of $ZnCo_2O_4$ film grown at 400ºC, 10 mTorr

Summary of the most important results

$BaFeO_{3-x}$ thin films were grown on single crystal perovskite substrates. It is found that as-deposited films were pseudo-cubic perovskite, nonconductive and weakly ferromagnetic, which differ from that of the bulk $BaFeO_3$. Two phases of $BaFeO_3$ were identified, an oxygen-deficient phase and an oxygen-rich phase, where formation of either/both is dependent on growth temperature and pressure. With increase in temperature, both phases are fully visible. After annealing in oxygen, the films change from translucent to reflective and exhibit a rather large change in lattice parameter. The films also show ferromagnetism and are in some cases are conductive. .

Further investigation of $BaFeO_{3-x}$ epitaxial films demonstrated a more complex structure dependence on processing seen in reciprocal space maps. After *ex situ* anneal in oxygen, these complex structures transform into a single pseudocubic structure that is magnetic. $BaFeO_3$ grown under low laser fluence is not easily convertible via anneal to a magnetic material. Its it tends to decompose into BaO and Fe_2O_3. With increasing thickness, the crystalline quality of as-grown $BaFeO_{3-x}$ decreases, but this decrease makes it a more compatible to annealing conversion to the magnetic phase. Artificial superlattices of $BaFeO_3/SrTiO_3$ were synthesized in an attempt to decrease cracking of annealed $BaFeO_3$ which occurs due to a large change in lattice constant when converted to the magnetic phase. Periodicities down to 4nm continued to result in partial cracking of the multilayers. The magnetization of *ex situ* annealed $BaFeO_{3-x}$ epitaxial films were examined as a function of direction. There was no dependence in magnetization on direction of field with respect to crystalline plane, despite other research claims.

Alloys of a solid-solution between $BiFeO_3$ and $BaFeO_{3-x}$ were successfully created. The alloy films via two-target rotation method have been realized over nearly the entire range of

solubility. The alloy films via solid-solution targets have been successfully fabricated at near both end-member-points and at 50/50 composition, showing that the solubility is possible over the entire range of the solid-solution. Investigation of the magnetic properties for strained and highly crystalline $Bi_{0.9}Ba_{0.1}FeO_3$ epitaxial films reveal that the samples are weakly ferromagnetic with a magnetization of $0.2\mu_B$ per Fe, more than an order of magnitude greater than that of pure $BiFeO_3$.

The synthesis and properties of $ZnCo_2O_4$ thin films was examined. $ZnCo_2O_4$ is a semiconducting oxide that exhibits the spinel crystal structure. Thin films were deposited using pulsed laser deposition. Growth temperatures were varied from 300°C to 800°C, with growth oxygen pressures from 10 to 200 mTorr. Under selected conditions, x-ray diffraction indicate that the films on sapphire are highly (111) oriented. Hall measurements indicate that the carrier type varies from n-type to p-type as the growth pressure increased. Resistivity was strongly dependent on the oxygen growth pressure, with resistivity varying between 0.001 to 0.326 Ω-cm. SQUID measurements indicated ferromagnetism in both n-type and p-type samples. Optical absorption spectra yielded a bandgap of 2.2-2.4 eV.

LIST OF REFERENCES

1 C. Ederer and N. A. Spaldin, Nat Mater **3**, 849 (2004).

2 W. Eerenstein, N. D. Mathur, and J. F. Scott, Nature **442**, 759 (2006).

3 N. A. Hill, The Journal of Physical Chemistry B **104**, 6694 (2000).

4 Y. Tokura, Science **312**, 1481 (2006).

5 J. F. Scott, Nat Mater **6**, 256 (2007).

6 N. A. Spaldin, *Magnetic materials : fundamentals and device applications* (Cambridge University Press, Cambridge, Uk; New York, 2003).

7 R. E. Hummel, *Electronic properties of materials* (Springer, New York, 2001).

8 S. O. Kasap, *Principles of electronic materials and devices* (McGraw-Hill, Boston, 2003).

9 A. Nussbaum, *Electronic and magnetic behavior of materials* (Prentice-Hall, Englewood Cliffs, N.J., 1967).

10 M. A. Gilleo, Physical Review **109**, 777 (1958).

11 A. J. Moulson, J. M. Herbert, and I. NetLibrary, (Wiley, Chichester; Hoboken, NJ.

12 M. W. Barsoum and I. NetLibrary, (Institute of Physics Pub., Bristol, UK; Philadelphia, PA.

13 K. M. Rabe, M. Dawber, C. Lichtensteiger, C. H. Ahn, and J. M. Triscone, Topics in applied physics. **105**, 1 (2007).

14 M. Erchak, I. Fankuchen, and R. Ward, Journal of the American Chemical Society **68**, 2085 (1946).

15 M. Erchak and R. Ward, Journal of the American Chemical Society **68**, 2093 (1946).

16 E. Lucchini, S. Meriani, and D. Minichelli, Acta Crystallographica, Section B (Structural Crystallography and Crystal Chemistry) **B29**, 1217 (1973).

17 H. J. V. Hook, The Journal of Physical Chemistry **68**, 3786 (1964).

18 S. Mori, Journal of the Physical Society of Japan **28**, 44 (1970).

19 F. Iga, Y. Nishihara, T. Katayama, K. Murata, and Y. Takeda, Journal of Magnetism and Magnetic Materials **104-07**, 1973 (1992).

20 E. Taketani, T. Matsui, N. Fujimura, and K. Morii, IEEE Transactions on Magnetics **40**, 2736 (2004).

21 T. Matsui, H. Tanaka, E. Taketani, N. Fujimura, T. Ito, and K. Morii, Journal of the Korean Physical Society **42**, 1378 (2003).

22 T. Matsui, E. Taketani, N. Fujimura, T. Ito, and K. Morii, Journal of Applied Physics **93**, 6993 (2003).

23 C. Michel, J.-M. Moreau, G. D. Achenbach, R. Gerson, and W. J. James, Solid State Communications **7**, 701 (1969).

24 J. R. Teague, R. Gerson, and W. J. James, Solid State Communications **8**, 1073 (1970).

25 V. M. Yudin, Soviet Physics-Solid State **8** (1966).

26 G. A. Smolenski, Yudin, V. M., Soviet Physics-Solid State **6**, 2936 (1965).

27 J. B. Neaton, C. Ederer, U. V. Waghmare, N. A. Spaldin, and K. M. Rabe, Physical Review B (Condensed Matter and Materials Physics) **71**, 14113 (2005).

28 F. Kubel and H. Schmid, Acta Crystallographica, Section B: Structural Science **46**, 698 (1990).

29 D. Lebeugle, D. Colson, A. Forget, and M. Viret, Applied Physics Letters **91**, 22907 (2007).

[30] R. Seshadri and N. A. Hill, Chemistry of Materials **13**, 2892 (2001).
[31] J. M. Moreau, C. Michel, R. Gerson, and W. J. James, Journal of the Physics and Chemistry of Solids **32**, 1315 (1971).
[32] R. T. Smith, G. D. Achenbach, R. Gerson, and W. J. James, Journal of Applied Physics **39**, 70 (1968).
[33] I. Sosnowska, T. P. Neumaier, and E. Steichele, Journal of Physics C: Solid State Physics **15**, 4835 (1982).
[34] T. Moriya, Physical Review **120**, 91 (1960).
[35] H. Bea, M. Bibes, S. Fusil, K. Bouzehouane, E. Jacquet, K. Rode, P. Bencok, and A. Barthelemy, Physical Review B (Condensed Matter and Materials Physics) **74**, 020101 (2006).
[36] D. H. Kim, H. N. Lee, M. D. Biegalski, and H. M. Christen, Applied Physics Letters **92**, 012911 (2008).
[37] H. Bea, Fusil, S, Bouzehouane, K, Bibes, M, Sirena, M, Herranz, G, Jacquet, E, Contour, J.-P., Japanese Journal of Applied Physics **45**, L187 (2006).
[38] H. Bea, M. Gajek, M. Bibes, and A. Barthelemy, Journal of Physics: Condensed Matter, 434221 (2008).
[39] S.-W. Cheong and M. Mostovoy, Nat Mater **6**, 13 (2007).
[40] N. A. Spaldin and M. Fiebig, Science **309**, 391 (2005).
[41] D. I. Khomskii, Journal of Magnetism and Magnetic Materials **306**, 1 (2006).
[42] M. Fiebig, Journal of Physics D: Applied Physics **38**, R123 (2005).
[43] H. Zheng, et al., Science **303**, 661 (2004).
[44] H. Tabata, K. Ueda, and T. Kawai, Materials Science and Engineering B **56**, 140 (1998).
[45] M. P. Singh, W. Prellier, L. Mechin, C. Simon, and B. Raveau, Journal of Applied Physics **99**, 024105 (2006).
[46] M. P. Singh, W. Prellier, L. Mechin, and B. Raveau, Applied Physics Letters **88**, 012903 (2006).
[47] P. Murugavel, P. Padhan, and W. Prellier, Applied Physics Letters **85**, 4992 (2004).
[48] P. Murugavel, D. Saurel, W. Prellier, C. Simon, and B. Raveau, Applied Physics Letters **85**, 4424 (2004).
[49] P. Murugavel, M. P. Singh, W. Prellier, B. Mercey, C. Simon, and B. Raveau, Journal of Applied Physics **97**, 103914 (2005).
[50] M. P. Singh, W. Prellier, C. Simon, and B. Raveau, Applied Physics Letters **87**, 022505 (2005).
[51] N. Hur, S. W. Cheong, S. N. Kale, S. B. Ogale, R. Choudhary, S. R. Shinde, and T. Venkatesan, Applied Physics Letters **86**, 112507 (2005).
[52] K. Fukae, T. Takahashi, T. Yoshimura, and N. Fujimura, Ultrasonics, Ferroelectrics and Frequency Control, IEEE Transactions on **55**, 1056 (2008).
[53] J. S. Kim, C. I. Cheon, C. H. Lee, and P. W. Jang, Journal of Applied Physics **96**, 468 (2004).
[54] V. A. Khomchenko, D. A. Kiselev, I. K. Bdikin, V. V. Shvartsman, P. Borisov, W. Kleemann, J. M. Vieira, and A. L. Kholkin, Applied Physics Letters **93**, 262905 (2008).
[55] S.-T. Zhang, L.-H. Pang, Y. Zhang, M.-H. Lu, and Y.-F. Chen, Journal of Applied Physics **100**, 114108 (2006).
[56] S. R. Das, R. N. P. Choudhary, P. Bhattacharya, R. S. Katiyar, P. Dutta, A. Manivannan, and M. S. Seehra, Journal of Applied Physics **101**, 034104 (2007).

[57] S.-T. Zhang, Y. Zhang, M.-H. Lu, C.-L. Du, Y.-F. Chen, Z.-G. Liu, Y.-Y. Zhu, N.-B. Ming, and X. Q. Pan, Applied Physics Letters **88**, 162901 (2006).
[58] G. L. Yuan, S. W. Or, J. M. Liu, and Z. G. Liu, Applied Physics Letters **89**, 052905 (2006).
[59] C. Fanggao, S. Guilin, F. Kun, Q. Ping, and Z. Qijun, Journal of Rare Earths **24**, 273 (2006).
[60] Z. Quan, W. Liu, H. Hu, S. Xu, B. Sebo, G. Fang, M. Li, and X. Zhao, Journal of Applied Physics **104**, 084106 (2008).
[61] A. Z. Simoes, A. H. Aguiar, A. H. M. Gonzalez, J. Andres, E. Longo, and J. A. Varela, Journal of Applied Physics **104** (2008).
[62] V. A. Khomchenko, et al., Journal of Physics: Condensed Matter, 155207 (2008).
[63] V. R. Palkar, D. C. Kundaliya, S. K. Malik, and S. Bhattacharya, Physical Review B **69**, 212102 (2004).
[64] J. Dhahri, M. Boudard, S. Zemni, H. Roussel, and M. Oumezzine, Journal of Solid State Chemistry **181**, 802 (2008).
[65] V. A. Khomchenko, D. A. Kiselev, E. K. Selezneva, J. M. Vieira, A. M. L. Lopes, Y. G. Pogorelov, J. P. Araujo, and A. L. Kholkin, Materials Letters **62**, 1927 (2008).
[66] V. A. Khomchenko, M. Kopcewicz, A. M. L. Lopes, Y. G. Pogorelov, J. P. Araujo, J. M. Vieira, and A. L. Kholkin, Journal of Physics D: Applied Physics, 102003 (2008).
[67] B. Kundys, A. Maignan, C. Martin, N. Nguyen, and C. Simon, Applied Physics Letters **92**, 112905 (2008).
[68] V. A. Khomchenko, D. A. Kiselev, J. M. Vieira, L. Jian, A. L. Kholkin, A. M. L. Lopes, Y. G. Pogorelov, J. P. Araujo, and M. Maglione, Journal of Applied Physics **103**, 024105 (2008).
[69] D. H. Wang, W. C. Goh, M. Ning, and C. K. Ong, Applied Physics Letters **88**, 212907 (2006).
[70] W. Eerenstein, F. D. Morrison, F. Sher, J. L. Prieto, J. P. Attfield, J. F. Scott, and N. D. Mathur, Philosophical Magazine Letters **87**, 249 (2007).
[71] C. Wang, M. Takahashi, H. Fujino, X. Zhao, E. Kume, T. Horiuchi, and S. Sakai, Journal of Applied Physics **99**, 054104 (2006).
[72] J. Wang, et al., Science **299**, 1719 (2003).
[73] V. L. Mathe, K. K. Patankar, R. N. Patil, and C. D. Lokhande, Journal of Magnetism and Magnetic Materials **270**, 380 (2004).
[74] H. Bea, M. Bibes, S. Petit, J. Kreisel, and A. BarthÃ©lÃ©my, Philosophical Magazine Letters **87**, 165 (2007).
[75] S. Yasui, Uchida, H, Nakaki, H, Funakubo, H, Koda, Seiichiro, Japanese Journal of Applied Physics **45**, 7321 (2006).
[76] X. Qi, J. Dho, R. Tomov, M. G. Blamire, and J. L. MacManus-Driscoll, Applied Physics Letters **86**, 062903 (2005).
[77] D. B. Chrisey and G. K. Hubler, *Pulsed laser deposition of thin films* (J. Wiley, New York, 1994).
[78] D. P. Norton, Materials Science and Engineering: R: Reports **43**, 139 (2004).
[79] D. H. Lowndes, D. B. Geohegan, A. A. Puretzky, D. P. Norton, and C. M. Rouleau, Science **273**, 898 (1996).
[80] J. Schubert, T. Heeg, and M. Wagner, Topics in applied physics. **106**, 115 (2007).
[81] J. E. Mahan, *Physical vapor deposition of thin films* (Wiley, New York, 2000).

[82] S. B. Ogale and MyiLibrary, *Thin films and heterostructures for oxide electronics* (Springer, New York, 2005).
[83] C. R. Brundle, C. A. Evans, and S. Wilson, *Encyclopedia of materials characterization : surfaces, interfaces, thin films* (Butterworth-Heinemann ; Manning, Boston; Greenwich, CT, 1992).
[84] R. L. Fagaly, Review of Scientific Instruments **77**, 101101 (2006).
[85] B. D. Cullity and S. R. Stock, *Elements of x-ray diffraction* (Prentice Hall, Upper Saddle River, NJ, 2001).
[86] J. Goldstein, *Scanning electron microscopy and x-ray microanalysis : a text for biologists, materials scientists, and geologists* (Plenum Press, New York, 1992).
[87] D. J. Craik, *Magnetic oxides* (Wiley, London; New York, 1975).
[88] R. Ramesh and N. A. Spaldin, Nature Materials **6**, 21 (2007).
[89] M. Sepliarsky, S. R. Phillpot, M. G. Stachiotti, and R. L. Migoni, Journal of Applied Physics **91**, 3165 (2002).
[90] J. Hombo, Y. Matsumoto, and T. Kawano, Journal of Solid State Chemistry **84**, 138 (1990).
[91] W. W. Malinofsky and H. Kedesdy, Journal of the American Chemical Society **76**, 3090 (1954).
[92] T. Matsui, H. Tanaka, N. Fujimura, T. Ito, H. Mabuchi, and K. Morii, Applied Physics Letters **81**, 2764 (2002).
[93] D. P. Norton, B. C. Chakoumakos, J. D. Budai, and D. H. Lowndes, Applied Physics Letters **62**, 1679 (1993).
[94] D. P. Norton, J. D. Budai, D. H. Lowndes, and B. C. Chakoumakos, Applied Physics Letters **65**, 2869 (1994).
[95] H. M. Christen, E. D. Specht, D. P. Norton, M. F. Chisholm, and L. A. Boatner, Applied Physics Letters **72**, 2535 (1998).
[96] H. M. Christen, L. A. Boatner, J. D. Budai, M. F. Chisholm, L. A. Gea, P. J. Marrero, and D. P. Norton, Applied Physics Letters **68**, 1488 (1996).
[97] K. H. Kim, D. P. Norton, J. D. Budai, M. F. Chisholm, B. C. Sales, D. K. Christen, and C. Cantoni, physica status solidi (a) **200**, 346 (2003).
[98] R. W. Eason, *Pulsed laser deposition of thin films : applications-led growth of functional materials* (Wiley, Hoboken, NJ, 2007).
[99] N. Takano, T. Okita, N. Nakayama, Y. Bando, Y. Takeda, O. Yamamoto, and J. B. Goodenough, in *J. Solid State Chem. ; Vol/Issue: 73:1*, United States, 1988), p. Pages: 140.
[100] C. Callender, D. P. Norton, R. Das, A. F. Hebard, and J. D. Budai, Applied Physics Letters **92**, 012514 (2008).
[101] M. Coey, Nature **430**, 155 (2004).
[102] M. Rajeswari, et al., Applied Physics Letters **73**, 2672 (1998).
[103] N. A. Hill and K. M. Rabe, (Materials Research Society, Warrendale, PA, USA, San Francisco, CA, USA, 1999), p. 157.
[104] D. Higashiyama, S. Miyasaka, N. Kida, T. Arima, and Y. Tokura, Physical Review B **70**, 174405 (2004).
[105] O. I. Lebedev, G. Van Tendeloo, N. Hayashi, T. Terashima, and M. Takano, Philosophical Magazine **84**, 3825 (2004).

[106] R. J. McQueeney, J. Ma, S. Chang, J.-Q. Yan, M. Hehlen, and F. Trouw, Physical Review Letters **98**, 126402 (2007).
[107] P. M. Woodward, D. E. Cox, E. Moshopoulou, A. W. Sleight, and S. Morimoto, Physical Review B **62**, 844 (2000).
[108] T. Takeda, Y. Yamaguchi, and H. Watanabe, Journal of the Physical Society of Japan **33**, 967 (1972).
[109] M. Azuma, H. Kanda, A. A. Belik, Y. Shimakawa, and M. Takano, Journal of Magnetism and Magnetic Materials **310**, 1177 (2007).